Velocity sensorless control switched reluctance motors

Erik Chumacero Polanco

UNIVERSITÉ PARIS SUD

Comprendre le monde, construire l'avenir®

L2S

Université Paris-Sud

Ecole Doctorale STITS

Laboratoire des Signaux et Systèmes

Discipline : Physique

Thèse de doctorat

Soutenue le 10 Avril 2014 par

Erik CHUMACERO-POLANCO

Velocity sensorless control of switched reluctance motors

Directeur de thèse :	M. Antonio LORIA	Directeur de recherche CNRS (LSS)
Composition du jury :		
Président du jury :	GLUMINEAU, Alain	Professeur (IRCCyN)
Rapporteurs :	GHANES, Malek	Maître de conferences HDR (ENSEA)
	HILAIRET, Mikaël	Professeur (FEMTO-ST)
Examinateurs :	GLUMINEAU, Alain	Professeur (IRCCyN)
	DAMM, Gilney	Maître de conferences HDR (Université d'Evry)

Declaration of Authorship

I, Erik Alfredo CHUMACERO POLANCO, declare that this thesis titled, '*Velocity sensorless control of switched reluctance motors*' and the work presented in it are my own. I confirm that:

- This work was done wholly or mainly while in candidature for a research degree at this University.
- Where any part of this thesis has previously been submitted for a degree or any other qualification at this University or any other institution, this has been clearly stated.
- Where I have consulted the published work of others, this is always clearly attributed.
- Where I have quoted from the work of others, the source is always given. With the exception of such quotations, this thesis is entirely my own work.
- I have acknowledged all main sources of help.
- Where the thesis is based on work done by myself jointly with others, I have made clear exactly what was done by others and what I have contributed myself.

Signed: _____

Date: _____

“When you make the finding yourself - even if you’re the last person on earth to see the light - you’ll never forget it. "

Carl Sagan

Abstract

"*Velocity sensorless control of switched reluctance motors*'4

by: Erik Alfredo CHUMACERO POLANCO

In this thesis dissertation we present the design, stability analysis, numerical simulations and physical experiments of different controllers designed to drive the mechanical velocity of the switched reluctance motor (SRM). In the First and Second Chapters a brief description of the physics and construction of the SRM is presented, as well as the problem of control to be aboard, that is the velocity sensorless control of motors and the state of the art of this problem. The proposed solution is introduced and a summary of the published papers as well as the contribution are also presented. In the Chapter number three is presented the velocity sensorless and adaptive control of the SRM. It is assumed, in a first stage, that only mechanical velocity is unknown, uniform exponential stability of the errors is achieved in this scenario. In a second stage, conditions are stressed and in addition to the velocity, physical parameters are also assumed unknown, uniform asymptotical stability is achieved in this case and parameters estimation is guaranteed under a persistence of excitation condition. This controller consists of two loops, an internal loop based on a PI^2D–type controller which is of particular interest given it is free-model; this loop drives the mechanical variables –that is position and velocity- towards a desired reference. An external control loop takes the electrical current towards a ''virtual" current reference which is generated based on a torque share approach. The controller is tested on numerical simulations, which are also presented. In the fourth chapter, a new approach on the modeling of the SRM is utilized to design the controller, in this scenario is assumed that the whole state and all the physical parameters are available, however this approach is thought to be suitable to observer based controller, whose ongoing research is being performed. The controller is composed by two loops, similarly to the one mentioned previously. This controller is selected because it is suitable for certainty equivalence control, that is, to substitute the "measurements" by the "observations" coming from a virtual sensor. Numerical implementation is performed on Simulink of Matlab.

Finally, in the Chapter five, the experimental results carried out to evaluate the performance of the proposed controllers are presented, these are the PI^2D and the adaptive PI^2D controllers for the simplified model and the PID controller for the novel modeling approach. In the first part, a brief description of the construction of the utilized bench is presented as well as the some technical characteristics. Three different velocity profiles were imposed to each of the overmentioned controllers –these are the so called smooth step, the saturated ramp and the sinusoidal reference- and good results, considering that the controlled variable is the velocity, were obtained. The last chapter corresponds to the conclusions of the performed research as well as to the future work.

Acknowledgements

First of all, I want to thank to Dr. Antonio LORIA, whose invaluable assistance and guidance, in addition to his almost infinite patience toward my unbounded mistakes, have asymptotically taken me to good culmination of studies. He induced me a new taste toward the fascinating world of stability theory, I know there is a long way to follow but he helped me to give the very first steps. Thanks also to my lovely friend, partner, companient, counselor... to my complement, my loved wife Yaret... for being beside me in the good, the bad and the worst.

For pushing me forward when I was forceless, for back me up when I was down, for keep my foot on earth when it was necessary, for being my lonely left-side pole.

To my mother Martha for teaching me to fight, to persevere, to love. To Alejandro for adopting me into his heart with love and care. To the lovely memory of my father Alfredo for his love and care during the very first years of my life. Thanks to my family, to my uncle Rogelio and my aunts Patricia and Mary, who have always treated me as a soon, loved and admired all of them. Finally, thanks to the Mexican people who, through the Mexican National Counsil for Science and Technology CONACYT, has financed and make possible this work.

Contents

List of Figures

List of Tables

Chapitre 1

Moteur à réluctance variable

Le moteur à réluctance variable est un moteur électrique dont le couple est produit par la tendance de son rotor à se déplacer jusqu'à une position où l'inductance du stator est maximisée. L'origine du moteur à réluctance peut être retracée à 1842. Sa ≪réinvention≫ a été probablement due à l'avènement des dispositifs de commutation peu chers et de haute puissance. Le moteur à réluctance est un type de machine synchrone. Le stator, pareil au stator d'un moteur à courant continu, est bobiné ; néanmoins, le rotor n'est ni bobiné ni magnétisé. Celui-ci est plutôt fait de feuilles de fer. Tant le stator que le rotor ont des pôles saillants, d'où le qualificatif de machine doublement saillante attribué au moteur à réluctance variable [1].

Le MRV a plusieurs caractéristiques qui le positionnent comme une option importante parmi d'autres machines couramment utilisées telles que les moteurs à courant continu, les moteurs asynchrones ou les moteurs synchrones . Ses principaux avantages sont sa construction simple et peu coûteuse, sans oublier sa capacité à se dispenser de courants bidirectionnels. De plus, les pertes thermiques n'apparaissent que dans le stator, facilitant son refroidissement. Un autre avantage majeur est la caractéristique vitesse-couple de rotation réglable qui permet l'obtention d'un couple élevé à basse vitesse et qui évite l'utilisation de boîtes de vitesses. Il est également possible de faire usage de ces moteurs à des températures plus élevées en comparaison à d'autres moteurs, tels que des moteurs à aimants permanents.

Cependant , le moteur à réluctance variable présente aussi des inconvénients. La construction à double saillance et la nature discrète de la production de couple par les phases indépendantes conduisent à plus d'ondulations de couple par rapport à d'autres machines. Ainsi, une ondulation de couple plus élevée, en même temps que la nécessité de récupérer de l'énergie à partir du flux magnétique, provoque une trop grande ondulation du courant, ce qui, en conséquence, réclame une grande capacité de filtrage. Également, la structure doublement saillante du moteur à réluctance variable provoque un bruit acoustique plus élevé par rapport à d'autres modèles. En fait, la principale source de bruit acoustique vient de la force magnétique radiale induite.

Ainsi, une plus grande ondulation de couple et le bruit acoustique sont les désavantages du MRV les plus critiqués. Toutefois, il faut souligner que les avantages du MRV sont nettement plus

importants que ses défauts, ce qui lui permet de disposer d'un large champ d'application dans les industries pour des usages réguliers comme dans les compresseurs, les ventilateurs, les pompes, les centrifugeuses, les robots culinaires, les machines à laver, les aspirateurs, et bien d'autres. Il est d'ailleurs encore bien présent dans l'industrie émergente des véhicules électriques. Une étude approfondie de la physique du MRV va au-delà de la portée de cette thèse, (Les lecteurs intéressés sont invités à trouver plus d'informations dans [2] et dans [3]). Cependant, dans les prochaines pages sera présentée une brève description du principe de fonctionnement de cette machine populaire.

1.1 *Construction et fonctionnement*

Le MRV est parmi les moteurs les plus simples concernant sa construction. Sa structure de base est composée d'un stator bobiné et d'un rotor en fer qui n'est ni bobiné ni magnétisé. Le rotor se compose essentiellement d'un morceau de fer laminé pour former des pôles saillants. Les pôles du stator sont également saillants et sont enroulés sur des pôles opposés radialement. Chaque phase du stator est constituée de bobines de stator concentrées sur les pôles. Parmi de nombreuses alternatives, les configurations les plus courantes sont les pôles 8*-rotor/*9*-stator 4-phases moteur et le* 6*-rotor/*4*-stator* 3*-phases moteur, dont un schéma est présenté dans la Figure 1.1.*

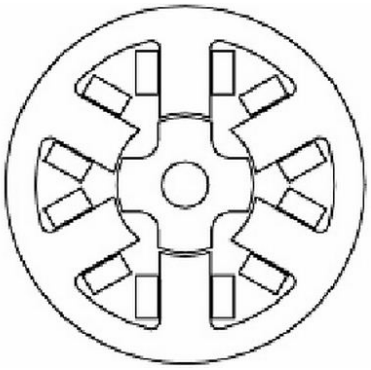

FIGURE 1.1: *Schématique d'un 6/4 3 phases moteur à réluctance variable.*

En supposant que les pôles r_2 et r'_2 du stator sont parfaitement alignés aux pôles c_2 et c'_2 du rotor, tel que montré sur la Figure 1.2-(1)*, si un courant électrique est appliqué à travers la phase $a-a'$, un flux magnétique est induit par les pôles du stator $a-a'$ de sorte que les pôles du rotor r_1 et r'_1 tournent vers les pôles du stator a et a' tel qu'il est montré sur la Figure 1.2-*(2)*. Une fois que les pôles sont alignés, le courant du stator de la phase a s'éteint. Ensuite, la bobine du stator $b-b'$ est excité, tirant r_2 et r'_2 vers b et b' dans le sens inverse des aiguilles d'une montre, comme illustré à la Figure 1.2-*(3)*.*

Par conséquent, il faut séquencer trois excitations dans l'ordre $a-b-c$ afin de déplacer le rotor de 60 *degrés. Suivant ce raisonnement, un tour de rotor est réalisé en effectuant la séquence $a-b-c$ autant de fois qu'il y a de nombre de pôles du stator. La commutation de courants dans la séquence $a-c-b$ produit donc une inversion de rotation du rotor.*

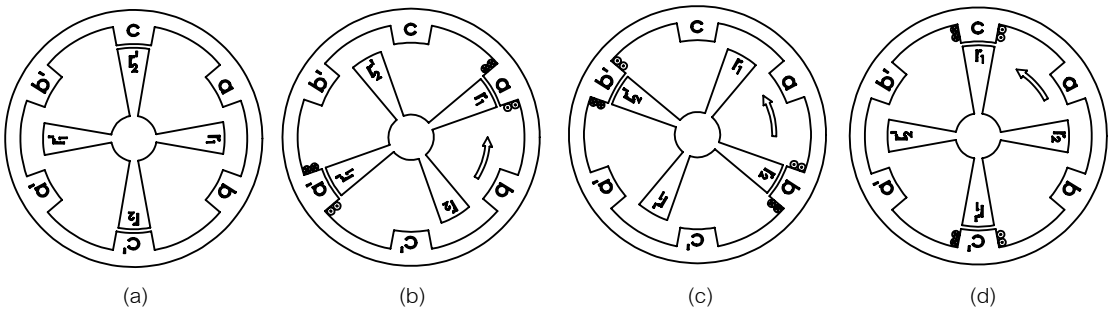

FIGURE 1.2: *Operation du MRV (1)-Phase c alignée (2)-Phase a alignée (3)-Phase b alignée (4)-Phase c alignée.*

L'inductance du MRV dépend de la position mécanique. En supposant que la phase a dans la Figure 1.3 est alimentée lorsque le stator et le rotor sont complètement désalignés (rotor entre q_1 et q_4), l'inductance réalisée est alors à son minimum. De même, lorsque le rotor et le stator sont alignés (rotor positionné au milieu de q_2 et q_3) l'inductance atteint son maximum. Ce comportement est illustré dans la figure suivante.

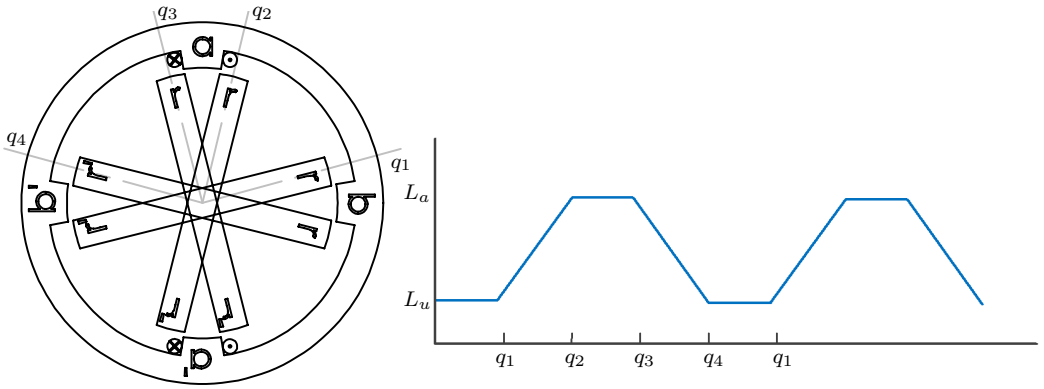

FIGURE 1.3: *L'inductance en tant que fonction de la position mécanique.*

1. $0 - q_1$: *Les pôles du stator et du rotor ne se chevauchent pas dans cette région et le flux est déterminé principalement par la voie d'air, ce qui rend le minimum d'inductance et à peu près constante. Par conséquent, cette région ne contribue pas à la production de couple. L'inductance dans cette région est connue comme inductance non aligné L_u.*

2. $q_1 - q_2$: *Les pôles se chevauchent, conséquemment le flux s'établit principalement entre les tôles du stator et du rotor. Cela augmente l'inductance de la position du rotor, ce qui lui donne une pente positive. Un courant imposé dans l'enroulement de cette région produit un couple positif. Cette région prend fin lorsque le chevauchement des pôles est terminé..*

3. $q_2 - q_3$: *Au cours de cette période, le mouvement du pôle de rotor ne modifie pas le chevauchement complet du pôle de stator et ne modifie pas le chemin de flux dominant. Ceci a pour effet de maintenir l'inductance maximale et constante, cette inductance est connue comme inductance alignée L_a. Comme il n'y a pas de changement dans l'inductance au*

cours de cette région, la génération de couple est zéro même lorsqu'un courant est présent dans cet intervalle. En dépit de ce fait, cette période joue un rôle utile en fournissant des temps pour le courant du stator pour revenir à zéro, ce qui empêche la génération de couple négatif pour une partie du temps lorsque le courant a été en décomposition dans la région de l'inductance à la pente négative.

4. $q_3 - q_4$: *Dans cette région, le rotor s'éloigne du pôle du stator (le chevauchement se termine). Ceci est très similaire à la région* $q_1 - q_2$ *excepté que l'inductance diminue pendant que la position du rotor augmente, contribuant ainsi à une pente négative de la région d'inductance. Le fonctionnement de la machine dans cette région se traduit par un couple négatif, à savoir, la génération d'énergie électrique à partir de l'entrée mécanique de la machine à réluctance variable.*

À cause de la saturation magnétique dans le MRV, il n'est pas possible d'atteindre les profils d'inductance idéales représentées sur la Figure 1.3. Même qui provoque, au-delà d'un point, une diminution sur le couple et la puissance de sortie.

1.2 *Production du couple mécanique*

La dépendance de la production du couple sur la saturation magnétique, en addition aux effets des champs frangeants et de l'excitation d'onde quarrée donne au MRV une caractéristique de commande non linéaire.

Le couple mécanique d'origine électrique (couple électromagnétique) est produit grâce à la tendance des pôles du rotor à s'aligner avec la phase du stator excité. Les déplacements du rotor à une position où la réluctance est à son minimum et où l'inductance est à son maximum même que la relation entre l'inductance et de la production de couple selon la position du rotor sont représentés sur la Figure 1.4. Pour un courant positif et constant, le couple positif est produit lorsque l'inductance augmente, tandis qu'aucun couple n'est produit lorsque l'inductance reste constante. Finalement, un couple négatif est produit lorsque l'inductance diminue. Sur la base de ce comportement, il est possible de calculer le temps de commutation nécessaire pour produire le couple désiré en fonction de la vitesse désirée.

La caractéristique couple-vitesse d'un MRV est donnée dans la Figure 1.5. Basée sur les plages de vitesses différentes, la génération du couple du moteur a été divisée en trois régions différentes : couple constant, puissance constante et région de chute de puissance.

La vitesse de base ω_B *est la vitesse maximale à laquelle le couple et le courant maximale peut être atteinte à la tension nominale. Dessous de* ω_B*, le couple peut être maintenue constante. À faible vitesse, le courant de phase augmente presque immédiatement après que les interrupteurs de phase se mettent en marche, depuis la force contre-électromagnétique est faible à ce moment. Ainsi, le courant peut être fixé à n'importe quel niveau désiré au moyen de régulateurs (hystérésis*

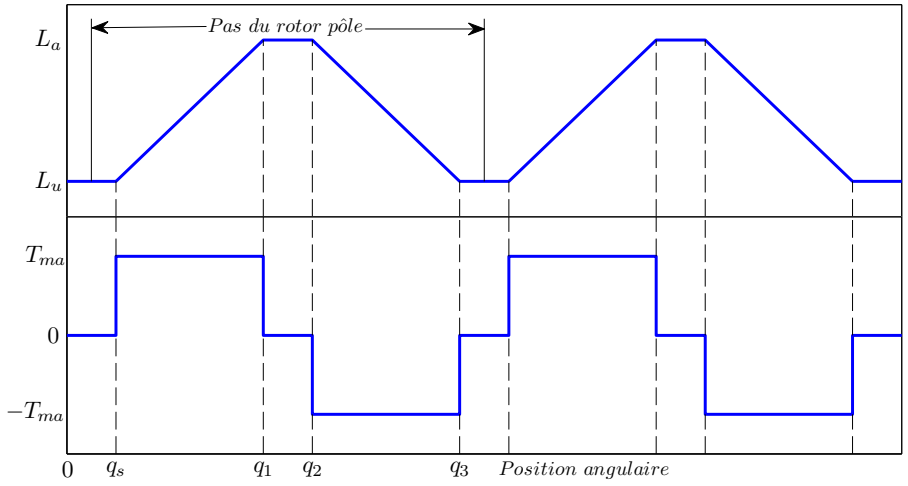

FIGURE 1.4: *Le couple et l'inductance en tant que fonctions de la position mécanique.*

ou contrôleur de modulation de largeur d'impulsion). Par conséquent, l'ajustement du cours de l'angle de tir peut réduire le bruit et d'améliorer l'efficacité d'ondulation ou du couple.

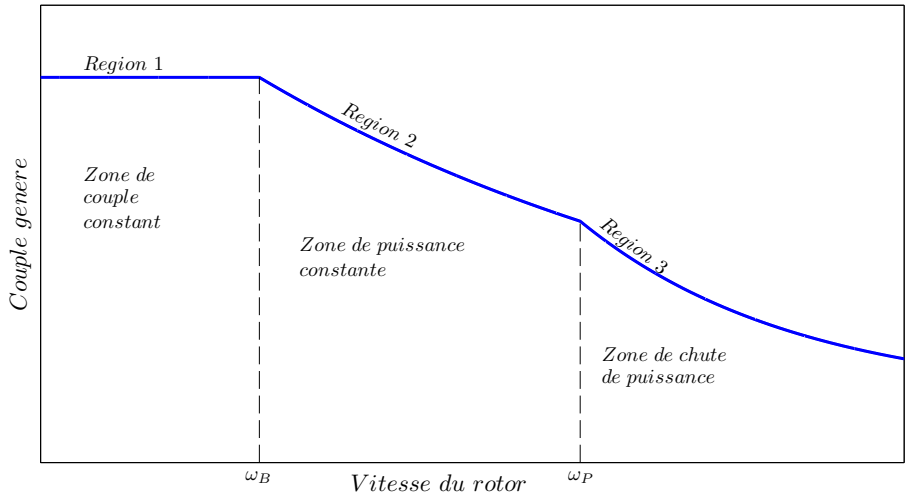

FIGURE 1.5: *La relation couple-vitesse.*

Lorsque la vitesse augmente, la force contre-électromotrice augmente également. Alors, un avancement de l'angle de conduction est nécessaire pour atteindre le courant désiré avant que le rotor et le stator ne commencent à se chevaucher. Le courant désiré est une fonction de la vitesse et de l'état de charge. Étant donné qu'aucun courant arraché n'apparaît au cours de l'angle d'arrêt, seule la commande de l'angle peut être utilisée à ce stade, de sorte que le couple ne peut pas être maintenue constant, causant sa diminution linéaire pendant que la vitesse augmente. Dans la région de puissance en baisse, lorsque la vitesse augmente, l'angle de conduction ne peut pas être avancé plus loin. En raison de la chute rapide de couple, la puissance ne peut être maintenue et le courant de queue de la bobine de phase s'étend à la région de couple négatif. Le courant de queue ne peut même pas tomber à zéro. Dans le fonctionnement à grande vitesse, la conduction du courant continu dans la bobine de phase peut augmenter le courant de phase et la densité de puissance peut être augmentée.

1.3 *Le problème de la commande sans capteur*

Comme mentionné précédemment , les machines à réluctance variable sont attrayantes car elles sont fiables, relativement pas cher et elles produisent un couple élevé à bas vitesse. Ces caractéristiques les rendent aptes à des fins différentes, notamment pour les applications à utilisation direct et pour l'actionnement des robots, où la position et la vitesse de joints doivent être contrôlées. Toutefois, ce type de machine n'est pas facile à contrôler, même sous des hypothèses expérimentalement validées conduisant à des simplifications. Tout d'abord, le modèle dynamique est fortement non linéaire par exemple, le couple électromagnétique est généré par une fonction complexe des courants électriques et de la positions du rotor. Deuxièmement , les méthodes indirects de détection pour les variables mécaniques qui soient fiables et précises sont fondamentales dans le développement des moteurs à réluctance de coût basset de haute-performance. D'une part, l'utilisation de capteurs mécaniques augmente le coût de la mise en place et d'autre part, des capteurs de vitesse sont souvent contaminées par du bruit. Par conséquent, éviter l'utilisation de capteurs de vitesse et de position angulaire, qui est bien connu comme ***contrôle sans capteur****, est au-delà de l'intérêt purement théorique.*

1.4 *L'état de l'art et les objectives de la recherche*

Il existe une riche littérature sur le contrôle adaptatif sans capteur sur les autres catégories de machines électriques. Par exemple, dans [4] un observateur adaptatif de flux, vitesse, couple de charge et la résistance électrique d'un moteur à induction est présenté et la stabilité pratique basée sur la théorie de Lyapunov est garantie, la validation expérimentale est même présentée. Dans [5] est présenté un observateur adaptatif à grand gain qui n'est fourni que par les mesures de courants et tensions pour le moteur synchrone à aimants permanents, cet observateur estime la vitesse du rotor, la position, la résistance du stator et le couple de charge. Dans [6], un contrôleur de vitesse sans capteur pour des moteurs synchrones à aimants permanents est conçu par la combinaison d'un contrôleur de retour robuste avec des actions intégrées et un observateur d'adaptation interconnecté, des conditions suffisantes sont données afin de prouver la stabilité pratique de la boucle fermée. Un contrôleur et un observateur à mode glissant avec retour de sortie sont conçus pour entraîner le moteur à induction sans l'aide de capteurs ni de flux ni de vitesse, des propriétés de stabilité sont garanties sur la base de la théorie de Lyapunov et des preuves expérimentales sont ainsi présentés. Une intéressante comparaison entre l'observateur de cascade et l'observateur à grand gain pour le contrôle sans capteur du moteur à induction est présente dans [7] et dans [8]. En ce qui concerne le moteur à réluctance variable, il existe un grand nombre d'approches de contrôle et d'identification qui sont basées sur l'euristique et validés expérimentalement . Ces dernières avec des objectifs différents de contrôle : contrôle de couple et de flux -[9], contrôle de vitesse -[10], estimation d'état -[11], identification de paramètres -[12]. Une comparaison de deux stratégies de contrôle qui permettent à la machine à réluctance variable de fonctionner en large plage de vitesse, est présenté dans [13]. En outre, l'auteur dans

[14] décrit une architecture optimisée basée sur un partitionnement matériel/logiciel, la stratégie proposée atteint ondulations inférieures de courant et de couple dans une large gamme de vitesse. Les auteurs de [15] présentent un contrôle sans capteur pour les moteurs à réluctance variable basés sur le contrôle direct de couple. Diverses design et réalisations expérimentales des observateurs de Luenberger pour position mécanique sont présentés dans [16] et dans [17], où les mesures de tensions et courants sont les seules entrées disponibles à l'observateur. Une approche intéressante apparaît dans [18] ; où, sans l'aide de capteurs optiques ou magnétiques, les informations stockées de la caractéristique magnétique est utilisée afin d'élucider la position mécanique, la même approche est présentée dans [19]. Une transformation de coordonnées du système de courants de phase est utilisé dans [20] pour concevoir un observateur de position, des résultats expérimentaux sont également présentés. Certains travaux sur le contrôle non basé sur modèle a été ainsi déclarée, dans [21] et dans [22] algorithmes de contrôle sans capteur basés sur la logique floue sont décrits et les résultats expérimentaux sont présentés. Dans [23] des réseaux neuronaux ont été utilisés pour prédire la position en utilisant l'inductance et des données de courant de phase sont utilisés par un deuxième réseau de neurones qui fournissent un courant de référence et minimise les ondulations de couple. De même, dans [24], un réseau neuronal de propagation avec pré-traitement d'entrée est utilisé pour estimer la position du rotor du MRV. Pour le contrôle entièrement sans capteur, dans [25] un contrôleur est présenté où la position et la vitesse sont obtenues à partir d'informations sur liaison de flux et courants de phase (pas d'analyse de la stabilité). Dans cette avenue, observateurs à mode glissant sont communs, par exemple, le papier [26] règle le problème d'estimation de vitesse et de position, d'autres travaux sur observateurs à mode glissants sont [26–28] où des résultats expérimentaux sont même inclus. Enfin, une revue intéressante sur commande sans capteur pour MRV est donnée dans [29] et, particulièrement sur le contrôle de position sans capteur, dans [30]. Une variété d'approches pour la commande sans capteur dans la littérature est donnée dans [31]. Cependant, pour le meilleur de la connaissance des auteurs, des articles sur le contrôle des moteurs à réluctance variable en incluant une analyse rigoureuse de la stabilité, en particulier dans un contexte sans capteur (et encore moins dans l'incertitude paramétrique) sont rares, même que pour ad hoc *solutions basées sur des méthodes telles que le contrôle de modèle prédictif - [32]. Le résultat principal dans [33] garantit la stabilité asymptotique globale pour un contrôleur basé sur passivité dans le cas de charge mécanique inconnue, mais il fait usage de deux variables mécaniques, vitesse et position. Un contrôleur du type PID est proposé dans [34] mais il relaie sur la connaissance de la charge de couple. Dans [35] les auteurs considèrent seulement la dynamique de rotor qui est, il est supposé que les courants sont entrés de commande physique valides. Dans [36] un contrôleur non linéaire utilisant un schéma similaire est présenté cependant, les auteurs supposent que la charge de couple mécanique est connue et le modèle inclut frottement visqueux ; Ce qui facilite considérablement l'analyse de stabilité. En dépit d'un certain nombre d'articles sur le contrôle des machines à réluctance variable via retour complet d'état - [33, 37–39] et retour partielle d'état - [10, 40] , il est intéressant de remarquer que l'absence d'analyse dans un contexte sans capteur n'est certainement pas le cas pour d'autres machines électriques tels que les moteurs à induction - voir [41, 42], ou machines synchrones à aimants permanents - [43, 44].*

Les travaux expérimentaux sur le contrôle de MRV est présent dans la littérature consultée, par exemple dans [45] la tension de chaque phase d'exécution et le signal de courant de référence sont utilisés en tant qu'entrées dans un système neuro-flou d'apprentissage pour obtenir la vitesse du rotor, alors, la position du rotor est déterminée par intégration de la valeur estimée de la vitesse. Les résultats expérimentaux montrent que la position du capteur de vitesse et le rotor virtuel proposé peut fonctionner dans un système de contrôle sans capteur pour le moteur à réluctance variable. Dans [46] sont réalisés des essais expérimentaux sur la base d'une approche de modélisation par éléments finis. Dans [47] un dispositif de commande en fonction d'un compensateur de type neuro-flou est proposé en plus d'un contrôleur proportionnel-intégral. Dans [48] un système de contrôle de vitesse du MRV en utilisant un contrôleur de logique floue est présenté et la performance est étudiée expérimentalement à différentes conditions de fonctionnement. Une technique de recherche en table est proposée dans [49] pour contrôler la tension de sortie d'un générateur à réluctance variable. Néanmoins, en dépit de l'importante quantité de littérature trouvée, aucun d'entre eux comprenait une démonstration rigoureuse de la stabilité, ce qui est une contribution importante de ce travail.

'objectif principal de ce travail est de proposer des alternatives à la commande sans capteur du MRV même que d'établir des conditions précises pour garantir différents types de stabilité. Afin d'atteindre cet objectif, nous avons divisé le travail en plusieurs objectifs spécifiques :

1. *concevoir un dispositif de commande pour le MRV en supposant que seulement le couple de charge et la vitesse mécanique ne sont pas connus ;*
2. *concevoir un dispositif de commande pour le MRV sous l'hypothèse que, en plus de la charge de couple et de la vitesse, tous les paramètres physiques sont également inconnus ;*
3. *concevoir un contrôleur basé sur une nouvelle approche de modélisation du moteur à réluctance variable qui est appropriée pour le design de contrôleurs basés en observateur.*

1.5 *La solution proposée et les contributions*

D'une manière générale, notre méthode de conception de contrôle est dépendant de la possibilité de séparer le modèle de la machine en ses composants électriques et mécaniques. La génération du couple est obtenue en suivant l'approche de couple couple présenté dans [34] avec le but de réduire l'ondulation qui apparaît dans les variables mécaniques à cause de la commutation électrique. Une première boucle de commande est conçue pour orienter les courants de stator à une "référence" souhaitée qui peut être considérée comme une entrée virtuelle de commande pour la dynamique mécanique. Puis, une boucle "externe" de contrôle comprenant un contrôleur de type PID est conçue, sans doute, la plus fréquemment utilisée dans la pratique. Nous avons utilisé deux différents modèles mathématiques, le premier introduit dans [34] surnommé dans ce travail q-modèle et le second surnommé ρ-modèle qui est introduit dans [50] et est inspirée

par les idées exprimées dans [51]. Pour le q-modèle nous avons proposé un premier contrôleur qui font usage de la position mécanique, du courant électrique et des paramètres physiques et un second contrôleur qui uniquement prend en compte la position et les courants ; la vitesse, les paramètres et le couple de charge sont assumés inconnus. Le ρ-modèle est plus intéressant, car il est propice à la commande basée sur observateur. Pour ce dernier modèle, nous avons proposé un contrôleur basé sur l'hypothèse que la position, la vitesse et le courant électrique sont disponibles et les paramètres physiques sont connus.

Il est important de souligner que même si la technique d'ajouter un filtre de la dérivée de la position pour connaître la vitesse n'est pas nouvelle, autant que nous savons, une analyse rigoureuse de la stabilité n'est pas encore présente dans la littérature. Ici, seront présentées les analyses de stabilité pour les trois contrôleurs conçus en textbf supposant que les paramètres physiques et que les mesures de vitesse et de couple de charge, en tant qu'inconnus, sont une nouveauté pour la théorie de contrôle de ce type de moteurs. D'autre part, il a été noté que le ρ-modèle n'a pas été largement utilisé. C'est pour quoi, dans ce travail, sont exploités les avantages qu'il offre pour la conception de commande. Une autre contribution importante de ce travail est la mise en œuvre d'expériences physiques sur les contrôleurs conçus. Cela a été réalisé dans le Département d'Ingénierie de l'Université Nationale Autonome du Mexique

Ce travail présente donc la conception, l'analyse, les simulations numériques et les résultats expérimentaux obtenus pour les preuves de différents contrôleurs du moteur à réluctance variable. Tout d'abord, les paramètres physiques sont supposés comme connus. La vitesse, quant à elle inconnue, est obtenue à travers un filtre dérivatif de la position. La stabilité exponentielle globale uniforme de l'origine est alors atteinte dans ce cas. Ensuite, il a été supposé qu'en plus de la vitesse les paramètres physiques soient aussi inconnus. Ainsi, un contrôleur d'équivalence positive a été utilisé afin de réussir le suivi de vitesse et l'estimation des paramètres. La stabilité asymptotique globale uniforme est établie sur la base d'une loi d'adaptation de type gradient et sur une condition de persistance d'excitation. Enfin, une nouvelle approche de modélisation est utilisée pour exprimer la dynamique mécanique du MRV, ie cette dynamique est décrite dans un nouveau système de coordonnées. Dans ce dernier cas, la stabilité exponentielle globale uniforme est réussie en supposant que les paramètres sont connus et que tout l'état est mesuré. Il est important de préciser que ce dernier contrôleur est une première étape vers un travail en cours sur la commande basée à observateur. Dans chaque cas, les conditions suffisantes ont été crées pour garantir que la stabilité soit exponentielle, asymptotique, globale, ou uniforme selon les hypothèses imposées. En outre, les résultats des expériences physiques effectuées permettent d'évaluer le comportement des contrôleurs conçus.

1.5.1 *Des papiers publis*

Les travaux de recherche de cette thèse ont conduit aux publications suivantes.

Magazine scientifique avec comité de lecture

- Loria, A. ; Espinosa-Perez, G. ; Chumacero, E. ***Exponential Stabilization of Switched-Reluctance Motors Via Speed-Sensorless Feedback*** ; Control Systems Technology, IEEE Transactions DOI : 10.1109 TCST.2013.2271446 Publication Year : 2013. In press.

- E. Chumacero, A. Loria, G. Espinosa, ***Velocity-sensorless tracking control and identification of switched reluctance motors*** in Automatica 2013. Provisionally accepted.

- A. Loria, G. Espinosa, E. Chumacero ***Robust passivity-based control of switched-reluctance motors*** in International Journal of Robust and Nonlinear Control 2013. Provisionally accepted.

Conferences international

- Loria, A. ; Espinosa-Perez, G. ; Chumacero, E. ; Aguado-Rojas, M.**Speed-sensorless control of switched-reluctance motors with uncertain payload** American Control Conference (ACC), 2013 Publication Year : 2013 , Page(s) : 3437 - 3442

- Chumacero, E. ; Loria, A. ; Espinosa-Perez, G. **Robust adaptive control of switched-reluctance motors without velocity measurements** Control Conference (ECC), 2013 European Publication Year : 2013 , Page(s) : 4586 - 4591

- Loria, A. ; Espinosa-Perez, G. ; Chumacero, E. **A novel PID-based control approach for switched-reluctance motors** Decision and Control (CDC), 2012 IEEE 51st Annual Conference on. DOI : 10.1109/CDC.2012.6426179 Publication Year : 2012 , Page(s) : 7626 - 7631

Chapter 2

The Switched Reluctance Motor

The switched reluctance motor is an electric motor in which torque is produced by the tendency of its rotor to move towards a position where the inductance of the excited winding is maximized. The origin of the reluctance motor can be traced back to 1842, but the "reinvention" has been possibly due to the advent of inexpensive, high-power switching devices. The reluctance motor is a type of synchronous machine. It has wound field coils of a DC motor for its stator windings and has no coils or magnets on its rotor. Both the stator and rotor have salient poles; hence, the switched-reluctance motor is a doubly salient machine [1].

It has several advantages that make it an important competitor among other widely used machines, such as direct-current motors, induction motors or even synchronous motors. We can point out its simple and low cost construction and the advantage that bidirectional currents are not necessary. Moreover, thermal losses appear only in the stator, which in fact is easier to cool down. Another important advantage is the speed-torque characteristic which is adjustable, making it possible to obtain high torque at low speed, thereby avoiding the use of gear boxes. It is also possible to make use of these motors at high temperatures and speed in comparison to other motors such as permanent magnet motors.

However, arg1 the switched-reluctance motor also presents some disadvantages. The double saliency construction and the discrete nature of torque production by the independent phases lead to higher torque-ripple compared to other machines. The higher torque ripple, and the need to recover energy from the magnetic flux, also cause the ripple current in the DC supply to be quite large, necessitating a large filter capacitor. The doubly salient structure of the switched-reluctance motor also causes higher acoustic noise compared to other machines. The main source of acoustic noise is the radial magnetic force induced. Thus, higher torque ripple and acoustic noise are the most critical disadvantages of the SRM. After all, the SRM advantages are heavier and the SRM has a wide field of application in general purpose industrial drives, compressors, fans, pumps, centrifuges, food processors, washing machines, vacuum cleaners. It is even present in the emerging electric vehicle industry and aircraft applications.

A deep study of the physics of the switched-reluctance motor is beyond of the scope of this thesis, (we invite interested readers to find further information in [3] and [2], among others). However, we present, next, a brief description of the operation principle of this popular machine.

2.1 Construction and operation

The switched-reluctance motor is among the simplest motors regarding its construction, the basic structure consists in a wound stator and an iron rotor that is neither wound nor magnetized. The rotor basically consists in a piece of laminated iron shaped to form salient poles. The stator poles are also salient and, furthermore, they are wound on radially opposite poles. Each stator phase is made up of concentrated coils placed on stator poles. Among many more options, the most common configurations are the 8-rotor/9-stator poles 4-phases motor and the 6-rotor/4-stator poles 3-phases motor, which is shown in Figure 2.1.

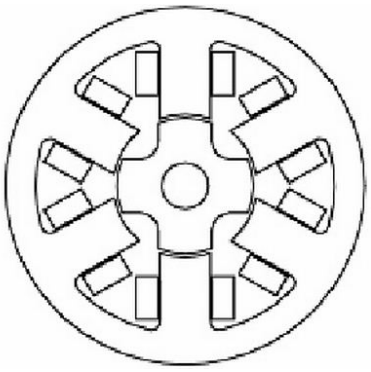

FIGURE 2.1: Schematic of a 6/4 3 phases switched-reluctance motor.

Assume that the rotor poles $r2$ and $r2'$ and stator poles c and c' are aligned, as it is shown in Figure 2.2-(1). If an electrical current is applied through the phase $a - a'$, a magnetic flux is induced through the stator poles $a - a'$ so the rotor poles $r1$ and $r1'$ tend to move toward the stator poles a and a' as it is shown in Figure 2.2-(2). Once they are aligned, the stator current of phase a is turned off. Then, the stator winding $b - b'$ is excited, pulling $r2$ and $r2'$ toward b and b', in a counter clockwise direction, as illustrated in Figure 2.2-(3). Likewise, energization of phase $c - c'$ results in the alignment of $r1$ and $r1'$ with c and c' (note the feeding sequence *a-b-c*). Hence, it takes three phase energization in sequence to move the rotor by 60 degrees and one revolution of rotor is effected by performing the *a-b-c* sequence as many times as there are number of stator poles. The switching of currents in the sequence *a-c-b* results in the reversal of rotor rotation.

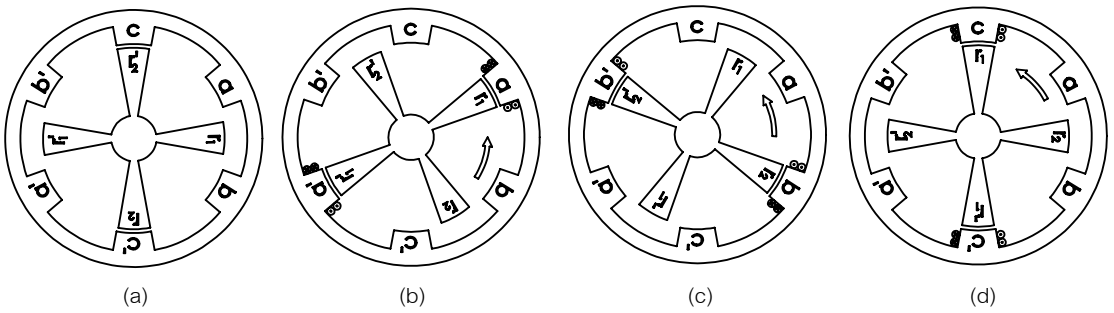

FIGURE 2.2: Operation of a switched-reluctance motor (1)-Phase c aligned (2)-Phase a aligned (3)-Phase b aligned (4)-Phase c aligned.

On the other hand, the inductance in the SRM depends on the mechanical position. For instance, assume that phase a in Figure 2.3 is fed, when stator and rotor are completely misaligned (rotor between q_1 and q_4) a minimum in the inductance is achieved; likewise, when rotor and stator are aligned (rotor between q_2 and q_3) we have a maximum, such behavior is depicted in the following figure

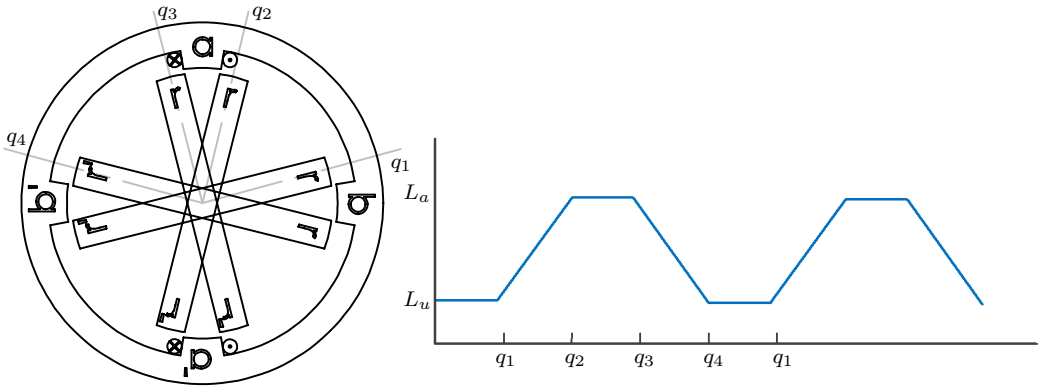

FIGURE 2.3: Inductance as function of mechanical position.

1. $0-q_1$: The stator and rotor poles do not overlap in this region and the flux is predominantly determined by the air path, making the inductance minimum and almost constant. Hence, this region does not contribute to torque production. The inductance in this region is known as unaligned inductance L_u.

2. q_1-q_2: The poles overlap, so the flux path is mainly through stator and rotor laminations. This increases the inductance with the rotor position, giving it a positive slope. A current impressed in the winding of this region produces a positive (*i.e.*, motoring) torque. This region comes to an end when the overlap of poles is complete.

3. q_2-q_3: During this period, movement of rotor pole does not alter the complete overlap of the stator pole and does not change the dominant flux path. This has the effect of keeping the inductance maximum and constant, and this inductance is known as aligned inductance L_a. As there is no change in the inductance in this region, *torque generation is*

zero even when a current is present in this interval. In spite of this fact, it serves a useful purpose by providing time for the stator current to come to zero or lower levels when it is commutated, thus preventing negative torque generation for part of the time if the current has been decaying in the negative slope region of the inductance.

4. $q_3 - q_4$: In this region the rotor pole moves away from overlapping the stator pole. This is very much similar to the $q_1 - q_2$ region, but it has decreasing inductance and increasing rotor position contributing to a negative slope of the inductance region. The operation of the machine in this region results in negative torque (i.e., generation of electrical energy from mechanical input to the switched reluctance machine).

As aconsequence of saturation , it is not possible to achieve the ideal inductance profiles shown in Figure 2.3 in an actual motor. Saturation causes the inductance profile to curve near the top and thus reduces the torque constant. Hence, saturating the machine beyond a point produces a diminishing return on torque and power output.

2.2 Induction of mechanical torque

The dependence of torque production on magnetic saturation , coupled with the effects of fringing fields and the classical fundamental square wave excitation result in nonlinear control characteristics for the reluctance motor.

The mechanical torque of electrical origin (electromagnetic torque) is produced due to the tendency of rotor poles to align with the excited stator phase. The rotor shifts to a position where reluctance is minimized and inductance is maximized, the relationship between inductance and torque production according to rotor position is shown in Figure 2.4. For a constant positive current, positive torque is produced when inductance increases, no torque is produced when inductance remains constant and, finally, negative torque is produced when the inductance decreases, based on this behavior, it is possible to select the switch on and off regime to produce torque and movement.

The torque-speed characteristic of a switched-reluctance motor is shown in (2.5), based on different speed ranges, the motor torque generation has been divided into three different regions: *constant torque*, *constant power* and *falling power region*.

The base speed ω_B is the maximum speed at which maximum current and rated torque can be achieved at rated voltage. Below ω_B, the torque can be maintained constant or control the fat-top phase current. At lower speed, the phase current rises almost instantly after the phase switches turn-on since the back-electromagnetic force is small at this time. So it can be set at any desired level by means of regulators (hysteresis or pulse-width modulation controller). Therefore, the adjustment of firing angle current can reduce noise and improve torque ripple or efficiency.

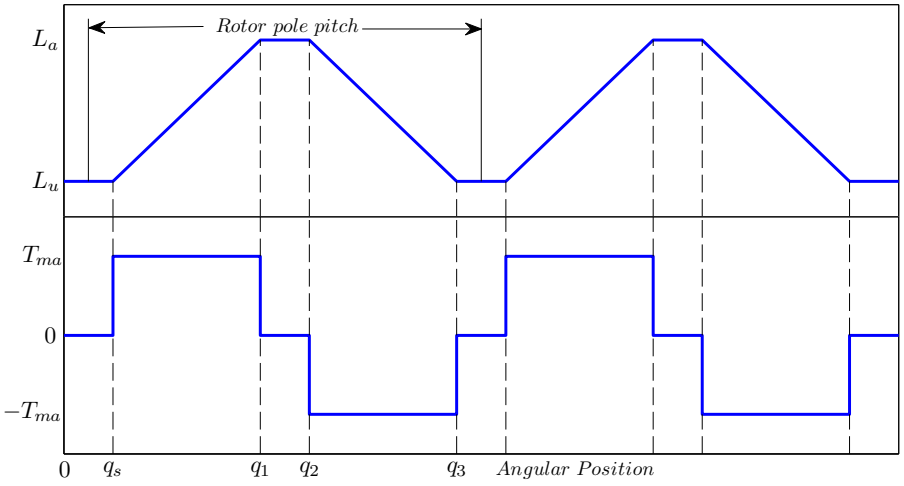

FIGURE 2.4: Torque and inductance as function of mechanical position.

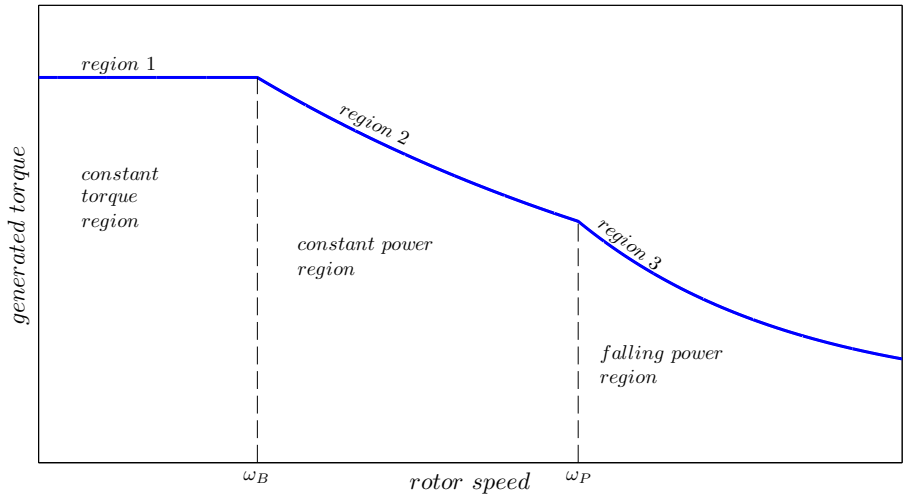

FIGURE 2.5: The torque-speed relationship.

As speed increases, the back-EMF also increases, then an advanced turn-on angle is necessary to reach the desired current before rotor and stator start to overlap. The desired current is a function of the speed and load condition, since no current chopping appears during the dwell angle, only the angle control can be used at this stage so the torque cannot be kept constant and is falling linearly as speed is increasing. In the falling power region, as speed increases, the turn-on angle cannot be advanced further. Due to the faster fall of torque, the power cannot be maintained and the tail current of the phase winding extends to the negative torque region. The tail current may not even drop to zero. In the high speed operation, the continued conduction of current in the phase winding can increase magnitude of phase current and the power density can be increased.

2.3 The sensorless control problem

As previously mentioned, switched-reluctance machines are attractive since they are reliable, relatively cheap and they produce high torque at low speed. These characteristics make them suitable for different purposes, among others for direct-drive and actioning robots applications, where position and velocity of joints must be controlled. However, this kind of machine is not easy to control; even under experimentally-validated assumptions leading to some simplifications. Firstly, the dynamic model is highly nonlinear *e.g.*, the generated electromagnetic torque is a complicated function of the electric currents and rotor positions. Secondly, reliable and accurate indirect sensing methods for the mechanical variables are fundamental in the development of low-cost, high-performance switched-reluctance motors. On one hand, the use of mechanical sensors increase the cost of the set-up and on the other, velocity sensors are often contaminated with noise. Therefore, avoiding the use of angular velocity and position sensors which is well known as ***sensorless*** control, is beyond pure theoretical interest.

2.4 State of the art and objectives of research

Literature on sensorless adaptive control on other class of electrical machines is rich. For instance, in [4] an adaptive observer of flux, velocity, load torque and resistance of an induction motor is presented and practical stability based on Lyapunov theory is guaranteed, experimental validation is presented as well. In [5] is presented an adaptive high gain interconnected observer which is only supplied by the measurements of electrical currents and voltages of the permanent magnet synchronous motor, this observer estimates the rotor speed, the position, the stator resistance and the load torque.

In [6], a sensorless speed control for interior permanent magnet synchronous motors is designed by combining a robust back-stepping controller with integral actions and an adaptive interconnected observer, sufficient conditions are given to prove practical stability of the closed-loop. A sensorless output feedback sliding-mode controller and observer are designed in order to drive the induction motor without using neither flux nor speed sensors, stability properties are guaranteed based in Lyapunov theory and experimental runs are presented as well. An interesting cascade and High-Gain Observers Comparison for Sensorless control of induction motor is presented in [7] and in [8].

Concerning the switched-reluctance motor, there exists a large number of efficient heuristically-based and experimentally-validated identification and control approaches with different control objectives: torque and flux control –[9], velocity control –[10], state estimation –[11], parameters identification –[12]. A comparison of two control strategies, that allow the switched-reluctance machine to operate in wide-speed-range, is presented in [13]. Moreover, in [14] is described an optimized architecture based on a hardware/software partitioning, the proposed strategy achieves lower current and torque ripples in a large speed range. *etc.*

The authors of [15] presented a sensorless control for switched-reluctance motors based on direct torque control. Designs and experimental implementations of Luenberger-type observers for position are presented in [16] and in [17], where measurements of voltages and currents are the only available inputs to the observer. An interesting approach appears in [18], where without using optical or magnetic sensors, stored magnetic characteristic information is utilized in order to elucidate the mechanical position, the same approach is presented in [19].

A coordinate transformation of the current phases system is utilized in [20] to design a position observer; experimental result are also presented. Some work on non model-based control has been as well reported, in [21] and in [22] fuzzy logic-based sensorless control algorithms are described and experimental results are presented as well. In [23] neural networks have been applied to predict position from inductance and phase current data and a second neural network provides a current reference that minimizes torque ripple. Likewise, in [24] an improved back propagate neural network with inductance input pretreatment for the rotor position estimator of switched-reluctance motor is proposed as well as a sensorless control algorithm.

For fully sensorless control, in [25] is given a controller where position and velocity are obtained from information about flux linkage and phase currents (no stability analysis). In this avenue, sliding mode observers are common, for example, paper [26] deal with the velocity and position estimation problem, other works on sliding mode observers are [26–28] where experimental results are also included.

Finally, interesting review on sensorless control for switched-reluctance motor is given in [29] and, particularly on position-sensorless control, in [30]. A variety of approaches for the sensorless commutation as reported in the literature is given in [31].

However, to the best of the authors knowledge, articles on control of switched-reluctance drives that include a rigorous stability analysis, especially in a sensorless context (let alone under parametric uncertainty), are rare. Certainly the same holds for *ad hoc* solutions based on methods such as model-predictive control —[32].

The main result in [33] establishes global asymptotic stability for a passivity-based controller in the case of unknown load but it makes use of both mechanical variables, angular velocity and position measurements. A proportional-derivative-based controller is proposed in [34] but it relays on the knowledge of the torque load. In [35] the authors consider only the rotor dynamics that is, it is assumed that the currents are valid physical control inputs. In [36] a nonlinear controller using a similar scheme is presented however, the authors suppose that the mechanical load-torque is known and the model includes viscous friction; This which eases considerably the stability analysis.

In spite of a number of articles on control of switched-reluctance machines via full state feedback –[33, 37–39] and partial state-feedback –[10, 40], it is worth remarking that the lack of analysis in a sensorless context is certainly not the case for other electrical machines such as induction motors – see [41, 42], or permanent-magnet synchronous machines –[43, 44].

Experimental work on control of switched-reluctance motor is present in the consulted literature, for instance in [45] the voltage from each conducting phase and the reference current signal are used as inputs to a neurofuzzy learning system to obtain the rotor speed, then, the rotor position is determined by integrating the estimated value of speed. The experimental results show that the suggested "virtual" speed sensor and corresponding rotor position can operate well in a sensorless switched-reluctance speed control system. In [46] experimental tests are performed based on a finite-element modeling approach. In [47] is proposed a controller based on a neuro-fuzzy compensator in addition to a *proportional-integral* controller. In [48] a speed control scheme of the switched-reluctance motor using a fuzzy logic controller is presented and the performance is investigated experimentally at different operating conditions. A "Lookup Table" technique is proposed in [49] to control the output voltage of a switched reluctance generator. Nevertheless, in spite of the large literature found, none of them included a rigorous proof of stability, which is an important contribution of the present work.

The main objective of this work is to offer some alternatives to the sensorless control of the switched-reluctance motor and to establish precise conditions to guarantee different kinds of stability. In order to accomplish this objective, we have split the work in several particular objectives:

1. to design a controller for the switched-reluctance motor under the assumption that only load torque and velocity are unknown;
2. to design a controller for the switched-reluctance motor under the assumption that, in addition to load torque and velocity, all the physical parameters are also unknown;
3. to design a controller based on a new modeling approach of the switched-reluctance motor which is suitable for observer based control.

2.5 The proposed solution and contributions

Generally speaking, our control-design method relies on the ability to separate the machine model into its electrical and mechanical components. Torque generation is achieved by following the *torque-sharing* approach of [34] with the aim of reducing the ripple in the mechanical variables that appears due to the electric commutation. A first control loop is designed to steer the stator currents to a desired "reference" that may be regarded as a virtual control input for the mechanical dynamics. Then, an "outer" control-loop is designed including a controller of proportional-integral-derivative type, probably the most often used in control practice.

We have used two different mathematical models, the first one introduced in [34] called the $q-model$ and the second one called $\rho-model$ is introduced in [50] which is inspired by ideas expressed in [51].

For the $q-model$ we proposed a first controller which make uses of position, current, parameters and a second controller which only considers position and current knowledge, that is velocity, parameters and load torque are unknown. The $\rho-$model is more interesting, this because it is suitable for observer-based control. For this model, we proposed a controller based on the assumption that position, velocity and electrical current are available and physical parameters are known.

It is important to point out that even when the technique of adding a derivative filter to the position in order to "know" the velocity is not new, to the best of our knowledge, a rigorous analysis of stability is not present in the literature on switched-reluctance motor; **we present here stability analyses for the three designed controllers**. Furthermore, **assuming both physical parameters and velocity measurements as unknown** in addition to load torque is new in the context of control theory of this kind of motors. On the other hand, the so called $\rho-model$ has not been widely utilized and in this work we exploit the advantages that it offers for control design.

Another important contribution of this work is **the physical implementation of the designed controllers**, this was carried out in the department of Engineering at the National Autonomous University of Mexico.

We present the design, analysis, numerical simulations and physical experiments under several scenarios of different sensorless controllers for the switched-reluctance motor. Firstly, we assume that the physical parameters are known and that unknown velocity is obtained trough a derivative filter of the position,uniform global exponential stability of the origin is achieved in this case. Secondly we assume, in addition, that the physical parameters are unknown. We use a certainty-equivalence controller to achieve velocity tracking and parameters estimation. Uniform global asymptotic stability is established, based on a gradient-type adaptive law and on a persistency of excitation condition. Finally, a new approach of modeling is used to express the mechanical dynamic of the switched-reluctance motor , *i.e.* this dynamic is described in a new set of coordinates, in this last stage uniform global exponential stability is achieved assuming that the parameters are known and the whole state is measured. We must clarify that this last control is a first step towards an ongoing work on observer based control. In each case, we give sufficient conditions to guarantee either uniform global exponential stability or uniform global asymptotical stability depending on the imposed assumptions. Moreover, we present the results of several physical experiments performed in order to evaluate the behavior of the designed controllers.

2.5.1 Published papers

The research work of this thesis led to the following publications.

Peer-reviewed journal

- Loria, A. ; Espinosa-Perez, G. ; Chumacero, E. ***Exponential Stabilization of Switched-Reluctance Motors Via Speed-Sensorless Feedback***; Control Systems Technology, IEEE Transactions DOI: 10.1109 TCST.2013.2271446 Publication Year: 2013. In press.

- E. Chumacero, A. Loria, G. Espinosa, ***Velocity-sensorless tracking control and identification of switched reluctance motors*** in Automatica 2013. Provisionally accepted.

- A. Loria, G. Espinosa, E. Chumacero ***Robust passivity-based control of switched-reluctance motors*** in International Journal of Robust and Nonlinear Control 2013. Provisionally accepted.

International conference

- Loria, A. ; Espinosa-Perez, G. ; Chumacero, E. ; Aguado-Rojas, M.**Speed-sensorless control of switched-reluctance motors with uncertain payload** American Control Conference (ACC), 2013 Publication Year: 2013 , Page(s): 3437 - 3442

- Chumacero, E. ; Loria, A. ; Espinosa-Perez, G. **Robust adaptive control of switched-reluctance motors without velocity measurements** Control Conference (ECC), 2013 European Publication Year: 2013 , Page(s): 4586 - 4591

- Loria, A. ; Espinosa-Perez, G. ; Chumacero, E. **A novel PID-based control approach for switched-reluctance motors** Decision and Control (CDC), 2012 IEEE 51st Annual Conference on. DOI: 10.1109/CDC.2012.6426179 Publication Year: 2012 , Page(s): 7626 - 7631

Chapter 3

Velocity Sensorless control via a PI^2D type controller

Velocity control of electrical machines is important in a variety of applications. In this chapter we present the design and analysis of a robust adaptive velocity-sensorless controller for the switched-reluctance motor. For clarity of exposition, we present a first result on *robust* stabilization where only the rotor inertia and load torque are considered as unknown. Then, in a second stage, we assume that the rest of physical parameters are unknown (stator inductances and resistance). Finally we incorporate an adaptation law for the electrical parameters.

3.1 A general model

Under the experimentally justified and widely accepted assumption that *the stator phases are magnetically decoupled*, (the mutual inductance between stator phases can be neglected) a general mathematical model for the m-phases switched-reluctance motor is given by:

$$\dot{\Psi}_j(q,x) + Rx_j = u_j \tag{3.1a}$$

$$J\dot{\omega} = T_e(q,x) - T_L(q,\dot{q}) \tag{3.1b}$$

$$\dot{q} = \omega \tag{3.1c}$$

where $j = \{1, 2 \ldots, m\}$ with m the number of phases, u_j is the voltage applied to the stator terminals, x_j is the stator electrical current, ψ_j is the linkage flux, q and ω are respectively the angular rotor position and velocity, T_L is the load torque, R is the stator winding resistance and J is the total rotor and load inertia. $T_e(q,x)$ is the mechanical torque of electrical origin (electromagnetic torque); note that it depends on both the angular position q and the electrical currents x.

The structure of model (3.1) is quite general and applies to several versions for complete and simplified models found in literature. What makes a difference among them, is the considered structure of the linkage flux $\Psi_j(q,x)$. Also note that Equation (3.1a) describes the behavior of the electrical variables while Equations (3.1b)-(3.1c) describe the behavior of the mechanical variables and correspond to a linear differential equation in q, $\dot{q}$ with inputs $T_e(q,x)$ and $T_L(q,\dot{q})$.

3.2 A saturated-flux model

In this section we present a mathematical model that takes into account the magnetic flux saturation phenomena, that is, the flux does not exceeds a threshold regardless electric current increases indefinitely –see Figure 3.1. This behavior can be described in different ways, we use the saturated model presented in [52] and [53], where the saturation phenomenon is described by an exponential -type function.

$$\psi_j(q,x_j) = \psi_s\left(1 - e^{-f_j(q)x_j}\right); \tag{3.2}$$

for the electrical current $x_j \geq 0$ with j as defined in previous section. The constant ψ_s denotes the saturated flux linkage and $f_j(q)$, known as the winding inductance, is a strictly positive periodic function commonly represented by a Fourier series as

$$f_j(q) = a + \sum_{m=1}^{\infty}\left\{b_m \sin\left(mN_r q - (j-1)\frac{2\pi}{3}\right) + c_m \cos\left(mN_r q - (j-1)\frac{2\pi}{3}\right)\right\}.$$

N_r denotes the number of pole pairs. The parameters a, b_m and c_m are constant positive reals, it is important to mention that the function f_j reflects the behavior of the inductance described in Section 2.1-Figure 2.3. A scheme of the linkage flux $\psi(q,x)$ expressed in (3.2), considering a positive fixed winding inductance $f(j(q)) \in [L_u, L_a]$, is depicted in the following figure:

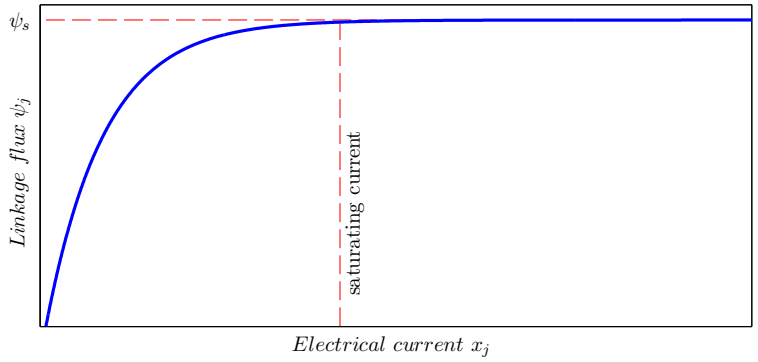

FIGURE 3.1: The current-linkage flux relationship.

On the other hand, as a result of the decoupled behavior, the torque of electrical origin, $T_e(q,x)$, results from the contribution of each stator electric current that is,

$$T_e(q,x) = \sum_{j=1}^{m} T_j(q,x)$$

where

$$T_j(q,x_j) = \frac{\partial}{\partial q} W'_j(q,x_j) \tag{3.3}$$

and

$$W'_j(q,x_j) = \int_0^{\bar{x}} \psi_j(q,x_j)dx_j. \tag{3.4}$$

is the *magnetic co-energy* at each winding. Hence, taking into account (3.2), (3.3) and (3.4) the electromagnetic torque at each phase results in

$$T_j(q,x_j) = \frac{\psi_s}{f_j^2(q)} \frac{\partial f_j(q)}{\partial q} \left\{ 1 - [1 + x_j f_j(q)] \exp^{-x_j f_j(q)} \right\}. \tag{3.5}$$

which clearly illustrate the complexity and nonlinear nature of the model.

Expression (3.2) enjoys two attractive features, namely, it accounts for magnetic saturation and, from a mathematical perspective, it is a continuous function. Its main disadvantage lies in the fact that the resulting electromagnetic torque T_e defines a not invertible map $x_j \mapsto T_j$, -see Equation (3.5).

Remark 3.1. *From (3.2), notice that if the current winding x_j is positive and bounded then the flux linkage is also positive and bounded. In fact, the maximum value that the flux can reach is the saturation value ψ_s.*

From (3.5), the assumed positivity of stator currents and the positivity of the nonlinear inductance $f_j(q)$, the torque sign is only determined by the term $(\partial f_j(q)/\partial q)$, *i.e.*, the variation of $f_j(q)$ with respect to rotor position q. This property agrees with the physical behavior of the motor and will be fundamental in the definition of the sharing functions -see *torque sharing technique* in page 28.

3.3 A simplified model in conventional coordinates

The mathematical model presented in Section 3.2 accounts for magnetic saturation but it leads to the definition of a non-invertible $x_j \mapsto T_j$ map (3.5). Therefore, the inductance of each phase f_j is now expressed as a strictly positive Fourier series truncated at the first harmonic, $L_j(q)$ –see [33, 54]; this implies that

$$\Psi(q,x) = L(q)x. \tag{3.6}$$

Where the winding inductance matrix $L(q) = \text{diag}\{L_j(q)\}$ is positive definite and each entry is defined as

$$L_j(q) \;=\; \ell_0 - \ell_1 \cos\Big(N_r q - (j-1)\frac{2\pi}{3}\Big),$$

and

$$K_j(q) = \frac{\partial L_j}{\partial q} = N_r \ell_1 \sin\Big(N_r q - (j-1)\frac{2\pi}{3}\Big)$$

corresponds to the phase-inductance variation relative to the rotor angular position. Constants $\ell_0 > \ell_1 > 0$ and N_r is the number of rotor poles. It is clear that

$$0 < l_m \leq |L_j(q)| \leq l_M, \quad |K_j(q)| \leq k_M. \tag{3.7}$$

for some positive constants l_m, l_M and k_M

Under such definitions, after (3.1a) and (3.6), a simplified mathematical model for the switched-reluctance motor is given by

$$L(q)\dot{x} + K(q)\omega x + Rx \;=\; u \tag{3.8a}$$

$$J\dot{\omega} \;=\; \mathbf{T}_e(q,x) - T_L(q,\dot{q}) \tag{3.8b}$$

$$\dot{q} \;=\; \omega \tag{3.8c}$$

Variable u is a column vector denoting the voltage applied to the stator terminals, x denotes the stator currents column vector, q and ω are respectively the rotor position and velocity, R denotes the stator winding resistance, J is the total rotor inertia. The load torque T_L and the mechanical torque of electrical origin $\mathbf{T}_e$.

Considering the decoupled behavior of stator windings, the mechanical torque $\mathbf{T}_e$ corresponds to the sum of torques T_j produced by m phases, that is

$$\mathbf{T}_e = \sum_{j=1}^{m} \frac{1}{2} K_j(q) x_j^2. \tag{3.9}$$

This model is adopted in both the electrical-machines and the control research communities –*cf.* [54].

3.4 The control problem and its solution

The control problem for the *simplified model* of the switched-reluctance motor is to design a dynamic controller whose output $u = [u_1\ u_2\ u_3]^\top$, depending only on measurements of the stator currents x and rotor angular positions q, stabilizes exponentially the origin $e_\omega = 0$, that is to achieve $\omega(t)$ tracks a desired reference trajectory $\omega^*(t)$, this problem was open until [55]. The control approach consists in applying two control loops, as illustrated in Figure 3.2. The

first one is an outer loop to robustly stabilize the rotor dynamics via the virtual control input T_e. The second and inner loop is used to stabilize the stator dynamics using currents measurements to guarantee the tracking control goal $\mathbf{T}_e \to T_e^*$, this is performed through the voltage input, which is the *real* control input.

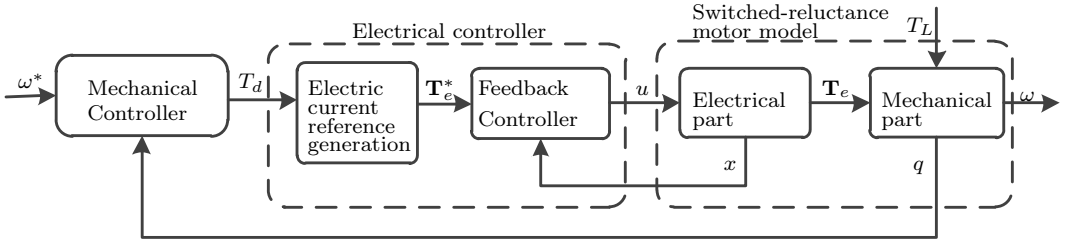

FIGURE 3.2: Control approach for the SRM in $q-$*model*.

For switched-reluctance motors modeled by (3.8) with torque of electrical origin defined by (3.9), we solve the velocity sensorless control problem via dynamic feedback control $u = [u_1\ u_2\ u_3]^\top$ which depends on the stator currents and rotor angular positions. The variable to be controlled is the rotor velocity ω. To that end, we make the following standing hypothesis.

Assumption 3.4.1.

- *the velocity reference trajectory, denoted* ω^**, is bounded, differentiable almost everywhere* $\dot{\omega}^*$ *is piecewise constant;*
- *the inertia* J *is unknown and belongs to an interval of known limits* J_m*,* J_M *i.e.,* $J \in [J_m, J_M]$*;*
- *the load torque* T_L *is piece-wise-constant and unknown.*

Note that Assumption 3.4.1 is fairly realistic; it comprises the case of piecewise continuous reference trajectories ω^* composed of steps and ramps –see the Simulations section. Also, in contrast to other theoretically-validated results in the literature, we assume that the inertia and the load-torque are unknown.

3.5 The control approach

We present in detail the two control loops mentioned above. The first one is applied to drive the rotor speed ω, toward its imposed reference ω^*, through a "virtual input" T_d. The second loop is designed in order to control the electrical current x and, therefore, the torque of electrical origin $\mathbf{T}_e$. Moreover, we present a model reference adaptive control in case the physical parameters ℓ_0, ℓ_1 and R are not known.

3.5.1 Robust control of rotor velocity

Considering $\mathbf{T}_e$ as an input, the rotor Equation (3.8b) is linear in the state ω with a (piecewise) constant perturbation T_L/J hence, we chose to use proportional-integral-derivative (PID) control, however, since the velocity ω is neither measured nor computed we use the PI²D controller, introduced in [56] for robot manipulators. Its name comes from the fact that it corresponds to a modified PID controller; it consists in a correction term proportional to the tracking errors e_q, a "derivative" term proportional to filtered velocities ϑ and a double integral action (where the notation I^2 comes from), both on e_q and ϑ. The PI²D controller is easy to implement, it conserves the passivity properties of Lagrangian systems and it ensures asymptotic stability provided a property of detectability holds –see [57]. Moreover, it is model-free which is fundamental in the present context in which we assume that the physical parameters are unknown. The PI²D *tracking* controller for the rotor dynamics is defined by

$$
\begin{aligned}
T_d &= \overbrace{-k_p e_q}^{P}\overbrace{+\nu}^{I^2}\overbrace{-k_d\vartheta}^{D}+\dot{\omega}^* && \text{(3.10a)}\\
\dot{\nu} &= -k_i(e_q-\vartheta) && \text{(3.10b)}\\
\dot{q}_c &= -a(q_c+be_q) && \text{(3.10c)}\\
\vartheta &= q_c+be_q && \text{(3.10d)}
\end{aligned}
$$

where q_c is a internal integrator and k_p, k_i, k_d, a, b are the positive control gains and $e_q = q - q^*$ the position tracking error with

$$
q^*(t) = \int_0^t \omega^*(s)ds, \quad q^*(0) = q_0^* \in [-\pi, \pi]. \tag{3.11}
$$

Since the variable to be controlled is ω, the initial value $q^*(0)$ is innocuous. Equations (3.10c) and (3.10d) correspond to the widely-used "approximate differentiation" filter

$$
\vartheta = \frac{b}{p+a}e_\omega \quad \Leftrightarrow \quad \dot{\vartheta} = -a\vartheta + be_\omega
$$

where p is the Laplace variable and $e_\omega := \omega - \omega^*$ denotes the velocity tracking error. Variable ϑ is not an estimate of the velocity error e_ω but a filtered version of it; in the limit case, when the pole is at $-\infty$, $\vartheta = e_\omega$ modulo the DC gain b/a.

The following is a preliminary but original result on the stability of the solutions of (3.8b) driven by the PI²D controller 3.10.

Proposition 3.1. *Consider the PI²D controller (3.10), let* $k_p' := k_p - (k_i/\varepsilon)$ *where* $\varepsilon \in (0,1)$, $k_i \leq \varepsilon$ *and let*

$$
\boldsymbol{T}_e^* = \eta T_d, \quad \eta > 0. \tag{3.12}
$$

Then, the solution

$$\left\{\left[q\ \omega\ \nu\right]^\top = \left[q^*\ \omega^*\ \nu^*\right]^\top\right\}, \quad \nu^* := \frac{T_L}{\eta} + \left(\frac{J}{\eta} - 1\right)\dot{\omega}^* \tag{3.13}$$

of the system (3.8b), (3.8c) with $\boldsymbol{T}_e = T_e^*$ *and under Assumption 3.4.1, is uniformly globally exponentially stable, provided that*

$$A(\eta) := \begin{bmatrix} 0 & 1 & 0 & 0 \\ -(\eta/J)k_p' & 0 & -(\eta/J)k_d & (\eta/J) \\ 0 & b & -a & 0 \\ -k_i & -k_i/\varepsilon & k_i & 0 \end{bmatrix} \tag{3.14}$$

is Hurwitz. Consequently, if $\boldsymbol{T}_e \neq T_e^*$ *the system is input-to-state stable with input* $\tilde{T}_e := \boldsymbol{T}_e - T_e^*$.

Remark 3.2. The equilibrium of the closed-loop system for the rotor dynamics depends on the parameter η which, on a case-by-case basis, may be known or unknown. However, the stability of the equilibrium may be established independently of its value. In Appendix A.1 we show that the matrix $A(\eta)$ is Hurwitz for any $\eta \in [\eta_m, \eta_M]$ and $J \in [J_m, J_M]$ if

$$b \geq \left[\frac{\eta_M}{J_m} + 1\right]a + 1, \quad k_p' > k_d.$$

Hence, the eigenvalues of A may be made negative by properly choosing the control gains k_p, k_d and k_i without the knowledge of η and J.

Proof of proposition 3.1. In view of (3.10a) and (3.12), Equation (3.8b) is equivalent to

$$\dot{\omega} = -\frac{\eta}{J}\left[k_p' e_q + \frac{k_i}{\varepsilon} e_q + k_d \vartheta\right] + \frac{\eta}{J}(\nu + \dot{\omega}^*) - \frac{T_L}{J} + \frac{\tilde{T}_e}{J}.$$

Next, let

$$z := \nu - \nu^* - \frac{k_i}{\varepsilon} e_q, \tag{3.15}$$

where ν^* is defined in (3.13) then,

$$\dot{e}_w = -\frac{\eta}{J}\left[k_p' e_q + k_d \vartheta - z\right] + \frac{\tilde{T}_e}{J}.$$

So differentiating on both sides of (3.15), using (3.10b) and rearranging terms we obtain the rotor closed-loop dynamics.

$$\dot{\xi} = A\xi + B\tilde{T}_e, \quad \xi := [e_q\, e_\omega\, \vartheta\, z]^\top \tag{3.16}$$

where $B = [0\ (1/J)\ 0\ 0]^\top$. Now, the Hurwitz property of A is equivalent to the existence of $P = P^\top > 0$ and a constant γ_1 such that $|PB| \leq \gamma_1$ such that $-(A^\top P + PA) = Q$ for a given

positive definite matrix Q, therefore

$$V_1(\xi) = \frac{1}{2}\xi^\top P\xi \tag{3.17}$$

satisfies

$$\dot{V}_1(\xi) \quad \leq \quad -\frac{1}{2}\xi^\top Q\xi + \frac{\gamma_1}{J}\left|\xi\right|\left|\tilde{T}_e\right| \quad \text{a.e.} \tag{3.18}$$

that is, V_1 is an *input to state*-Lyapunov function and $\tilde{T}_e = 0$ implies global exponential stability of $\{\xi = 0\}$. The result follows observing that $\xi = 0$ implies that $\begin{bmatrix} q & \omega & \nu \end{bmatrix}^\top = \begin{bmatrix} q^* & \omega^* & \nu^* \end{bmatrix}^\top$ □

3.5.2 Control of the stator dynamics

Equation (3.16) is valid if and only if (3.12) holds for a given T_d; this is accomplished by solving $T_e^*(q, x^*) = \eta T_d$ for x^* *i.e.*,

$$\frac{1}{2}\sum_{i=1}^{3} x_i^{*2} K_i(q) = \eta T_d \sum_{i=1}^{3} m_i(q).$$

To that end, we employ the so-called *torque sharing technique –cf.* [34]. We consider the commutation smooth functions $q \mapsto m_j$ such that $\sum_{j=1}^{3} m_j(q) = 1$ then, we define

$$x_j^* = \left[\frac{2\eta T_d m_j}{N_r \ell_1 s_j(q)}\right]^{1/2} \qquad \forall\, j \in \{1, 2, 3\}$$

where $s_j(q)$ may be equal to zero and the quotient above may be negative. For x_j^* to be well-posed we exploit the physics of the reluctance machine as in [34, 54] and introduce a current-switching policy as follows. Let the sets

$$\begin{aligned} \Theta_j^+ &= \{q \in [-\pi, \pi] : s_j(q) \geq 0\} \\ \Theta_j^- &= \{q \in [-\pi, \pi] : s_j(q) < 0\} \end{aligned}$$

and let

$$m_j(q) = \begin{cases} m_j^+(q) & \text{if} \quad T_d \geq 0 \\ m_j^-(q) & \text{if} \quad T_d < 0 \end{cases}$$

where

$$\begin{aligned} m_j^+(q) > 0 \quad \forall q \in \Theta^+, \quad m_j^+(q) = 0 \quad \forall q \in \Theta^-, \\ m_j^-(q) > 0 \quad \forall q \in \Theta^-, \quad m_j^-(q) = 0 \quad \forall q \in \Theta^+. \end{aligned}$$

Because the functions s_j are sinusoids out of phase by $2\pi/3$, for each q and T_d there always exists (at least) one $j \in \{1, 2, 3\}$ such that

$$\inf \frac{T_d m_j(q)}{s_j(q)} > 0, \qquad \sup \frac{T_d m_j(q)}{s_j(q)} < \infty$$

Furthermore, to make the phase transitions smooth we introduce hysteresis around the switching condition $s_j = 0$ *i.e.*,

$$x_j^*(q, T_d) := \begin{cases} \left[\frac{2\eta}{N_r \ell_1}\right]^{1/2} \left[\frac{T_d m_j(q)}{s_j(q)}\right]^{1/2} & \text{if } |s_j(q)| > \delta_K \\ 0 & \text{otherwise} \end{cases} \tag{3.19}$$

where δ_K is the hysteresis design parameter. Under these conditions we have $T_e^*(q, x^*) = \eta T_d$ so to ensure that $T_e \to \eta T_d$ we must solve the new tracking control problem $x \to x^*$.

The rationale behind the design of the tracking controller for the stator dynamics builds on the observation that under the action of the tracking control law

$$u = L(q)\dot{x}^* + \omega^* K(q)x + Rx^* - k_{px}e_x, \quad e_x = x - x^*, \tag{3.20}$$

the origin of the closed-loop equation

$$L(q)\dot{e}_x + [R + k_{px}]e_x = -K(q)xe_\omega \tag{3.21}$$

with zero input ($e_\omega \equiv 0$) is globally exponentially stable, provided that $k_{px} > 0$, since L is positive definite. Furthermore, the system may be rendered input to state stable from the input e_ω provided that the gain k_{px} dominates over the input "gain" function $K(q)x$; note that this is feasible since q and x are measured states. Under these conditions one may invoke a small-gain argument to establish global exponential stability of the origin of the closed-loop system (3.16), (3.21).

However, the control law (3.20) is not implementable since $\dot{x}^*$ depends on the unmeasured velocity ω indeed,

$$\dot{x}_j^* = \begin{cases} \alpha_j \Big[\rho_j + \delta_j e_\omega\Big] & \text{if} \quad |s_j(q)| > \delta_K \\ 0 & \text{otherwise} \end{cases}$$

where, if $|s_j(q)| > \delta_K$,

$$\begin{aligned} \alpha_j &= \frac{1}{2}\left[\frac{2\eta}{N_r \ell_1}\right]^{1/2} \left[\frac{m_j T_d}{s_j}\right]^{-1/2} \\ \rho_j &= \frac{m_j}{s_j}\Big[(k_d a + k_i)\vartheta - k_i e_q + \frac{\partial m_j}{\partial q}\frac{T_d \omega^*}{m_j}\Big] - \frac{m_j N_r c_j}{s_j^2} T_d \omega^* \\ \delta_j &= \frac{1}{s_j}\Big[- m_j(k_p + k_d b) + \frac{\partial m_j}{\partial q} T_d\Big] - \frac{m_j N_r c_j}{s_j^2} T_d \end{aligned} \tag{3.22}$$

otherwise, $\alpha_j = \rho_j = \delta_j = 0$.

Therefore, we introduce the following control law which is reminiscent of u as defined in (3.20) except that we drop the term $\alpha_j \delta_j e_\omega$ in the definition of $\dot{x}^* = [\dot{x}_1^*,\ \dot{x}_2^*,\ \dot{x}_3^*]^\top$ *i.e.*, let

$$u = L(q)\alpha\rho + \omega^* K(q)x + Rx^* - k_{px}e_x, \tag{3.23}$$

where $\alpha = \text{diag}\{\alpha_1, \alpha_2, \alpha_3\}$, $\rho = [\rho_1 \;\; \rho_2 \;\; \rho_3]^\top$ and $\delta = [\delta_1 \;\; \delta_2 \;\; \delta_3]^\top$. Therefore, (3.23) is equivalent to

$$u = L(q)\dot{x}^* + \omega^* K(q)x + Rx^* - k_{px}e_x - L(q)\alpha\delta e_\omega. \tag{3.24}$$

The closed-loop Equation (3.8a) with (3.24) yields

$$L(q)\dot{e}_x = -\left[R + k_{px}\right]e_x - \Big[K(q)x + L(q)\alpha\delta\Big]e_\omega \tag{3.25}$$

which is also reminiscent of a perturbed linear system with stable drift; in this case the input gain is given by

$$g(t, x, y) := \Big[K(q(t))x + L(q(t))\alpha(t, y)\delta(t, y)\Big] \tag{3.26}$$

in which we underline the dependence of α and δ on $\omega^*(t)$, $q(t)$ and the measurable output $y := [e_q \, \vartheta \, \nu]^\top$. Moreover, since L, K, m_j, $\dfrac{\partial m_j}{\partial q}$ and ω^* are uniformly bounded, there exists a non-decreasing function $\gamma_2 : \mathbb{R}_+ \times \mathbb{R}_+ \to \mathbb{R}_+$ such that

$$|g(t, x, y)| \leq \gamma_2\left(|y|, |x|\right).$$

Note that γ_2 depends on $\eta_M \geq \eta$ but not on the constant η. Thus, it may be established that (3.25) is input-to-state stable with respect to the input e_ω, for an appropriate choice of the gain k_{px} depending on γ_2, hence on $|y|$ and $|x|$.

3.5.3 Robust control of the switched-reluctance motor

From the previous developments we see that the closed-loop system (3.16), (3.25) consists in the interconnection of two input-to-state stable systems for which the feedback gains may be adjusted to ensure global exponential stability under the following hypothesis.

Assumption 3.5.1. *(i) Let the control gains and $\hat{J}$, which is a constant estimate of J, be such that the matrix $A(\hat{J})$ in (3.14) is Hurwitz for any $J \in [J_m, \; J_M]$ –see Remark 3.2.*
(ii) Assume that the stator parameters ℓ_0, ℓ_1 and R are known.

Proposition 3.2. *Consider the system (3.8) in closed loop with the PI²D controller (3.10) under the conditions of Proposition 3.1 and the control law (3.23) where $x^* = [x_1^* \; x_2^* \; x_3^*]^\top$ is defined via (3.19) with $\eta := \hat{J} \in [J_m, J_M]$. Let Assumption 3.5.1 hold. Then, there exist a real number $k'_{px} > 0$ and a continuous function $\left(\omega^*, |y|, |x|, |x^*|\right) \mapsto k''_{px}$, such that $k''_{px}\left(\omega^*, \cdot, \cdot, \cdot\right)$ is non-decreasing and*

$$k_{px} = k'_{px} + k''_{px}\left(\omega^*, |y|, |x|, |x^*|\right),$$

with $e_x := x - x^*$, the origin $\left\{[\xi, \, e_x] = [0, \, 0]\right\}$ of the closed-loop system (3.16)-(3.25) is uniformly globally exponentially stable.

This result establishes uniform global exponential stability for the closed-loop system, under the assumption that the gain k_{px}, in the stator control loop, is a nonlinear function of the measurable currents and $y := [e_q\, \vartheta\, \nu]^\top$. The proof of the proposition above is presented in Appendix A.2.1, where a precise expression for k_{px} is given.

Now we assume that, in addition to J and T_L, the physical parameters ℓ_0, ℓ_1 and R are also unknown. Let matrix $C(q) := \text{diag}\{c_j(q)\}$, $S(q) := \text{diag}\{s_j(q)\}$, where we recall that $c_j(q) = \cos\left(N_r q - (j-1)\frac{2\pi}{3}\right)$ and $s_j(q) = \sin\left(N_r q - (j-1)\frac{2\pi}{3}\right)$. Then, $L(q) = \ell_0 I - \ell_1 C(q)$ and $K(q) = \ell_1 N_r S(q)$. We introduce the *constant* estimate of ℓ_1, $\hat{\ell}_{1\circ} \in [\ell_m,\ \ell_M]$ to redefine η in (3.19) as

$$\eta := \frac{\hat{J}\ell_1}{\hat{\ell}_{1\circ}} \tag{3.27}$$

so α in (3.22) and x^* in (3.19) depend only on known quantities. With this notation, the control law (3.23) may be written as

$$u = \ell_0 \alpha\rho - \ell_1 C(q)\alpha\rho + \omega^* \ell_1 N_r S(q) x + R x^* - k_{px} e_x$$

which is linear in the physical parameters ℓ_0, ℓ_1 and R therefore,

$$\begin{aligned} u &= \Psi(t, y, e_x)^\top \Theta - k_{px} e_x, \\ \Psi(t, y, e_x)^\top &:= \begin{bmatrix} \alpha\rho & \omega^* N_r S(q) x - C(q)\alpha\rho & x^* \end{bmatrix}, \\ \Theta &:= \begin{bmatrix} \ell_0 & \ell_1 & R \end{bmatrix}^\top. \end{aligned}$$

We stress that Ψ is a function of t, the measured outputs $y = [e_q\, \vartheta\, \nu]^\top$ and the closed-loop states e_x; indeed, one should read $q(t)$ and $x = e_x + x^*$ in place of q and x while α, ρ and x^* are functions of t, y and known constants.

Proposition 3.3. *Consider the system (3.8) in closed loop with the PI²D controller (3.10) under the conditions of Proposition 3.1 and*

$$u = \Psi(t, y, e_x)^\top \hat{\Theta} - k_{px} e_x, \tag{3.28a}$$

$$\dot{\hat{\Theta}} = -k_\theta \Psi(t, y, e_x) e_x, \qquad k_\theta > 0. \tag{3.28b}$$

Let the control gains and $\hat{J} \in [J_m,\ J_M]$ be such that the matrix $A(\eta)$, with η as in (3.27), is Hurwitz for any $J \in [J_m,\ J_M]$. Define $\tilde{\Theta} := \hat{\Theta} - \Theta$. Then, the origin of the closed-loop system, $\{[\xi,\ e_x,\ \tilde{\Theta}] = [0,\ 0,\ 0]\}$ is uniformly globally stable (i.e., the origin is uniformly stable and the solutions are uniformly globally bounded) and the tracking errors ξ and e_x satisfy

$$\lim_{t\to\infty} |\xi(t)| = 0 \qquad \lim_{t\to\infty} |e_x(t)| = 0.$$

The proof of the above proposition is presented in Appendix A.2.2.

Furthermore, under the additional condition of persistence of excitation, we establish the uniform convergence of the parameter estimation errors.

Proposition 3.4. *Consider the system (3.8) in closed loop with the PI^2D controller (3.10) under the conditions of Proposition 3.1 and (3.28) under the conditions of Proposition 3.3. Then, the origin of the closed loop system is uniformly globally asymptotically stable if and only if $\Psi_0(t) := \Psi(t,0,0)$ is persistently exciting that is if there exist $\mu > 0$ and $T > 0$ such that*

$$M(t) := \int_t^{t+T} \Psi_0(s)\Psi_0(s)^\top ds \;\geq\; \mu I \quad \forall\, t \geq 0. \tag{3.29}$$

The proof is based on Matrosov's theorem and it is presented in Appendix A.2.3.

3.6 Simulation Results

With aim at evaluating the controller of Proposition 3.4 we performed some numerical simulations in SIMULINK™ of MATLAB™on a fully-nonlinear model which takes into consideration linkage-flux saturation, that is we have used the flux expression $\psi_j(q,x) = \psi_s \exp(-L_j(\theta)x_j)$, a diagram of this is shown in 3.3.

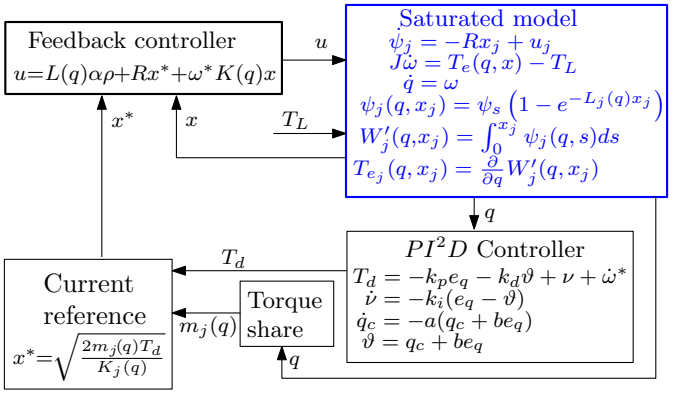

FIGURE 3.3: Diagram of simulation

The parameters are shown in Table 3.1 –some of the motor parameters are taken from [54].

Motor	Controller
$R = 0.3[\Omega]$	$a = 1500$
$\ell_0 = 24[\text{mH}]$	$b = 3200$
$\ell_1 = 19[\text{mH}]$	$k_p = 3500$
$J = 10\text{e}^{-4}[\text{kg}\cdot\text{m}^2]$	$k_i = 5\,\text{e}^{-4}$
$\psi_s = 0.25$	$k_d = 1500$
$N_r = 25$	$\varepsilon = 5\ \text{e}^{-4}$
$\eta = 0.1275$	$k_{px} = 750$

TABLE 3.1: Simulation parameters

It is important to point out that matrix $A(\eta)$ in Equation (3.14) is Hurwitz for the gains exposed in the table above.

On the other hand, the velocity reference signal $\omega^*(t)$ is obtained from the following smooth function

$$\omega^*(t) = \begin{cases} \omega_1^*(t) & \text{if} \quad t < 6.25 \\ \omega_2^*(t) & \text{if} \quad 6.25 \leq t < 12.5 \\ \omega_3^*(t) & \text{if} \quad 12.5 \leq t < 18.75 \\ \omega_4^*(t) & \text{if} \quad 18.75 \leq t \end{cases}$$

where each $\omega_k^*(t)$ is in turn defined by the function

$$\omega_k^*(t) = \omega_{0k}^* + \frac{\omega_{fk}^* - \omega_{0k}^*}{2}\left(1 + \frac{1 - \exp^{-\gamma t}}{1 + \exp^{-\gamma t}}\right)$$

for $k = \{1, 2, 3, 4\}$ and $\omega_{01}^* = 5$, $\omega_{f1}^* = 100$, $\omega_{02}^* = 100$, $\omega_{f2}^* = 150$, $\omega_{03}^* = 150$, $\omega_{f3}^* = -50$, $\omega_{04}^* = -50$ and $\omega_{f4}^* = 5$. Finally, $\gamma = 5$. The gain of the adaptive law is to $k_\theta = \text{diag}[5\text{e}^{-7}, 1\text{e}^{-6}, 2.5\text{e}^{-5}]$.

We recall that the nonlinear part of the gain, k_{px}'', has importance in the *theoretical* statement as it guarantees the global nature of the stability property however, in a typical case-study scenario and for implementation purpose it is both sufficient and convenient to use a constant value for k_{px} to avoid high values in the input voltages.

The commutation functions $m_j : [0, 2\pi) \to \mathbb{R}_+$, which are illustrated along with the currents in Figure 3.7, are defined as follows. Let

$$f(x) = \frac{10x^3}{(\pi/N_r)^3} - \frac{15x^4}{(\pi/N_r)^4} + \frac{6x^5}{(\pi/N_r)^5}$$

and $q_1 := \text{mod}(q, 2\pi/N_r)$, $q_2 := \text{mod}(q - 2\pi/3N_r, 2\pi/N_r)$, $q_3 := \text{mod}(q + 2\pi/3N_r, 2\pi/N_r)$ where the operator mod resets q that is, $q_j = \text{mod}(\beta_1, \beta_2)$ takes the initial value $q_j(0) = \beta_1$ and is reset to the latter when $q_j(t) = \beta_2$. This behavior is reflected on the following figure.

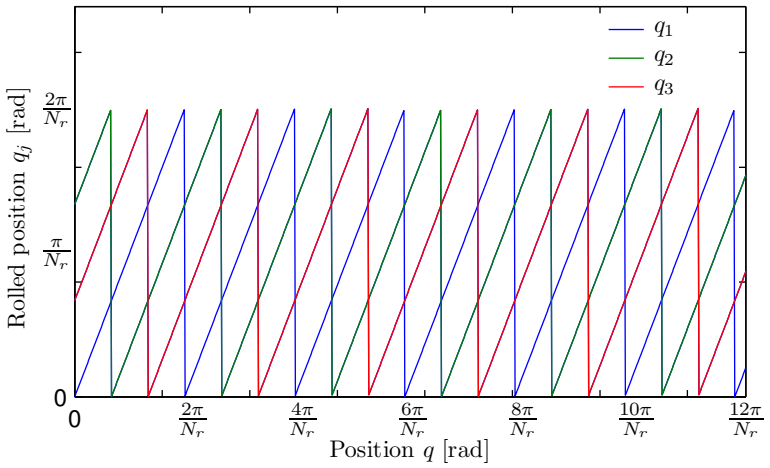

FIGURE 3.4: Rolled positions.

Then, auxiliary functions $m_j^+(q)$ and $m_j^-(q)$ are defined as

$$m_j^+(q) = \begin{cases} f_j(q_j) & 0 < q_j \leq \frac{\pi}{3N_r} \\ 1 & \frac{\pi}{3N_r} < q_j \leq \frac{2\pi}{3N_r} \\ 1 - f_j(q_j) & \frac{2\pi}{3N_r} < q_j \leq \frac{\pi}{N_r} \\ 0 & \text{otherwise} \end{cases} \quad \text{and} \quad m_j^-(q) = \begin{cases} f_j(q_j) & \frac{\pi}{N_r} < q_j \leq \frac{4\pi}{3N_r} \\ 1 & \frac{4\pi}{3N_r} < q_j \leq \frac{5\pi}{3N_r} \\ 1 - f_j(q_j) & \frac{5\pi}{3N_r} < q_j \leq \frac{2\pi}{N_r} \\ 0 & \text{otherwise.} \end{cases}$$

The following figure depicts the function $m_j^+(q)$ and $m_j^-(q)$ in phase with $K_j(q)$, it can be noticed that $m_j^+(q)$ is positive when K_j is positive and zero otherwise. The same occurs with $m_j^-(q)$, which is positive when $K_j(q)$ is negative.

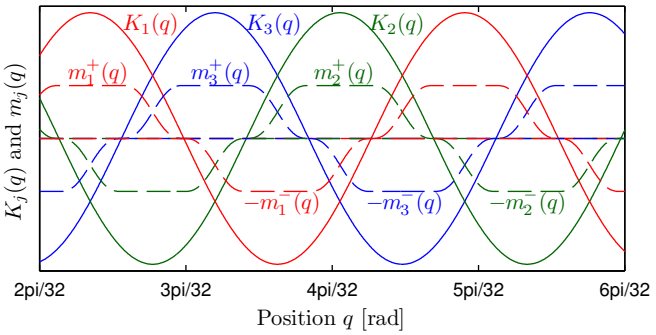

FIGURE 3.5: Switching regime function

The simulation consists in imposing a realistic speed reference namely, the desired motor speed starts off from 5[rad/sec], accelerating gradually up to 100[rad/s]. This value is kept constant until $t \approx 7s$ when the reference velocity increases up to 150[rad/s]. The new velocity reference is kept up to $t \approx 13s$ when the motor is rapidly brought to a regime of inverse rotation at -50[rad/s], afterwards, the reference is taken to 5[rad/sec] where remains until the end of the simulation. During the first 5s, the load torque equals to $1[Nm]$ and it is abruptly increased by 50% at $t = 5$s.

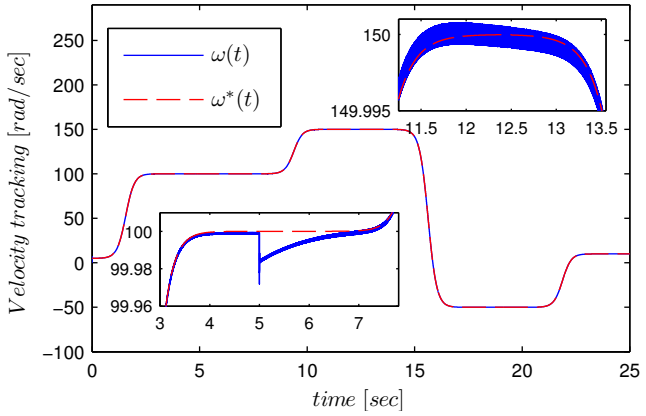

FIGURE 3.6: Velocity Tracking.

In Figures 3.7 and 3.8 we show the results of the electrical current tracking. In Figure (3.7) it is shown on left-hand side plots the transient during the first three seconds note that currents do not overpass $2.5A$. On middle plot it is shown a zoom over the steady state behavior around $t = 5$, when load torque T_L arise by 50%. On right-hand side plot it is shown the current over a small time window, note that for all t, at least two currents are larger than zero.

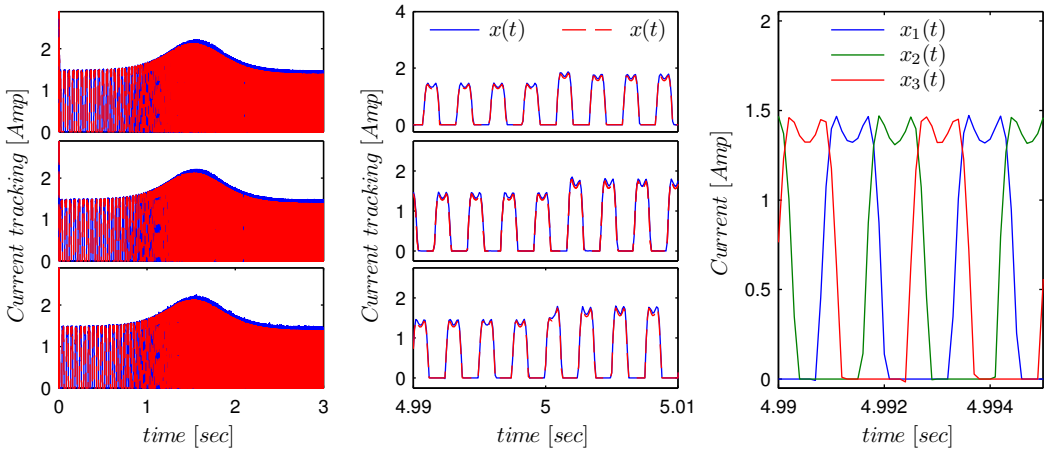

FIGURE 3.7: Electric current during the transient and tracking during the steady state.

On Figure (3.8) we show the overlap of signal concerning the electrical current $x_j(t)$ and the switching regime function $m_j(t)$, note that this last leads the reference $x_j^*(t)$, such as it was stated by the torque share approach.

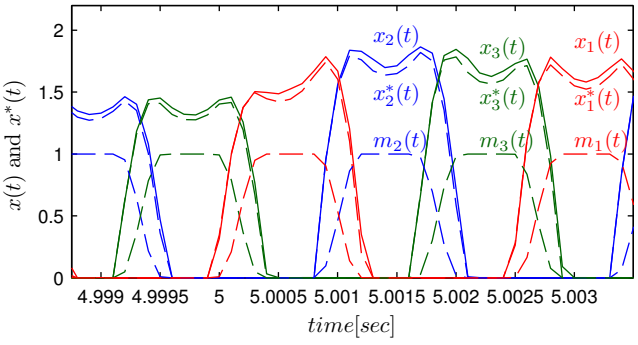

FIGURE 3.8: Electric current around $t = 5s$ when the load torque changes. The dashed lines correspond to the commutation signals m_j.

We show the voltage input, In Figure 3.9 is shown the transient over the first three seconds, notice that magnitudes are suitable for the SRM and seldom overpass $100V$ in magnitude.

On the small zoom is noticed the sequence of phasing, which is characteristic in this machine.

In Figure 3.10 is shown the behaviour of the input control over the time of simulation, once again the magnitude is not too high.

The last two figures illustrate the performance of the adaptation law. In this regard, it is worth recalling that, for model-reference adaptive controlled systems, persistency of excitation is a necessary condition for the estimation errors of the parameters –see [58].

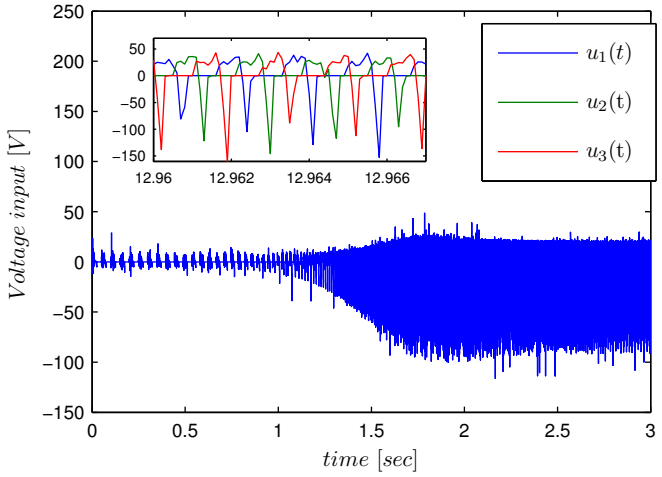

FIGURE 3.9: Voltage control inputs u_j

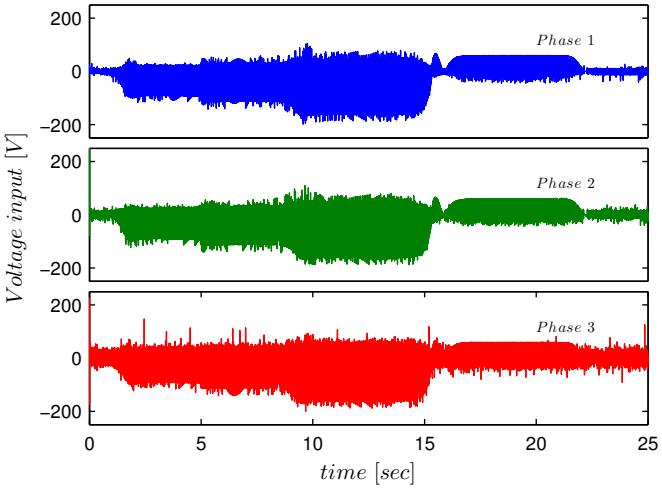

FIGURE 3.10: Voltage control inputs u_j

Common knowledge includes the fact that at least as many frequencies as unknown parameters must be involved in the regressor matrix $\Psi(t, \xi, e_x)$, however, this does not imply that the entries of the latter must be periodic or even continuous. In general, verifying the persistency of excitation condition is a very hard task since it involves solving in closed form complex and involved integrals of functions of time. Alternatively, one may as well accept as verification of (3.29), its numerical computation on a finite simulation window. In that spirit Figure 3.12 clearly shows that the eigenvalues of $M(t)$, which is defined in (3.29), are positive. This illustrates for this case-study, in the absence of rigorous proof, that the condition of persistency of excitation is satisfied.

3.6.1 Verification of the persistence of excitation condition

It is worth recalling that, for model-reference adaptive controlled systems, persistence of excitation is a necessary condition for the estimation errors of the parameters –see [58]. Common knowledge includes the fact that at least as many frequencies as unknown parameters must be

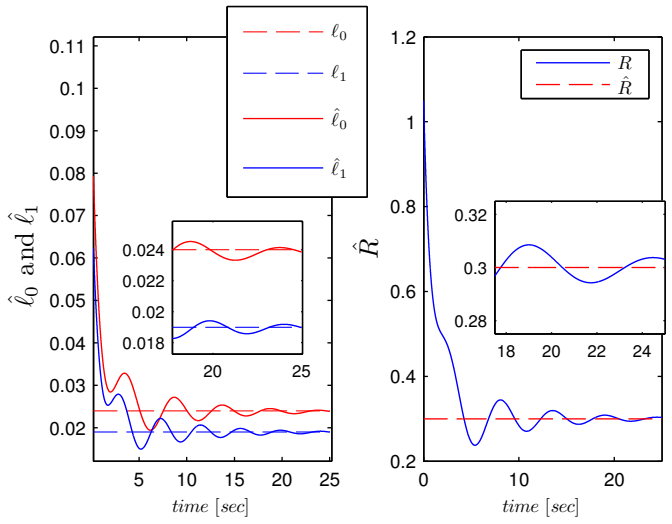

FIGURE 3.11: Estimated parameters converging to the true values

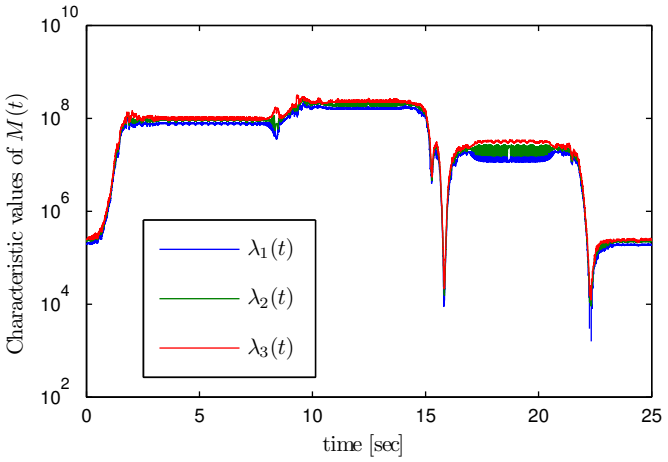

FIGURE 3.12: Verification of the condition of persistency of excitation: eigenvalues of $M(t)$ in (3.29) on the window of simulation.

involved in the regressor matrix, however, this does not imply that the entries of the latter must be periodic or even continuous.

Generally speaking, verify the persistence of excitation condition is very hard since it involves solving complex integrals of functions of time in closed form. Alternatively, one may as well accept as verification of (3.29), its numerical computation on a finite simulation window. In that spirit, Figure 3.15 shows that the eigenvalues of $M(t)$, which is defined in (3.29), are positive for all $t \in [0 \quad 25]$. This illustrates, for this case-study, that the condition of persistence of excitation is satisfied on the simulation window of 25[sec].

We will show that, for a fixed $T > 0$, function M is positive definite for all t in the interval of simulation, that is, all three eigenvalues of $M(t)$ are strictly positive. Note that the time simulation is 25 seconds.

The eigenvalues of $M(t)$ are computed numerically, using MATLAB™. First, we recall that $\Psi_0(t)$ is defined as

$$\Psi_0(t) := \Psi(t,0,0) = \begin{bmatrix} \alpha_0\rho_0 & \omega^* N_r S(q^*)\bar{x}^* - C(q^*)\alpha_0\rho_0 & \bar{x}^* \end{bmatrix} \tag{3.30}$$

where $\alpha_0 = \text{diag}\{\alpha_{01} \;\; \alpha_{02} \;\; \alpha_{03}\}$, $\rho_0 = [\rho_{01} \;\; \rho_{02} \;\; \rho_{03}]^\top$ and $\bar{x}^*$, as defined in 3.19, with $e_x = 0$, $q = q^*$ and $\nu = \nu^*$. That is, $\Psi_0(t)$ corresponds to the 3x3 matrix that results from setting $e_x = 0$ and $\xi = \begin{bmatrix} e_q & e_\omega & z & \vartheta \end{bmatrix}^\top = 0$ in $\Psi(t, e_x, \xi)$ and it is a function of t since so is q^*.

Therefore, for each $j = \{1, 2, 3\}$ we have

$$\alpha_{0j} = \frac{s_j(q^*)\nu^* m_j'(q^*)\omega^* - \nu^* m_j(q^*)N_r c_j(q^*)}{s_j^2(q^*)} \tag{3.31}$$

$$\rho_{0j} = \frac{s_j(q^*)\nu^* m_j'(q^*) - (k_p + bk_d)m_j(q^*)sj(q^*) - \nu^* m_j(q^*)N_r c_j(q^*)}{s_j^2(q^*)} \tag{3.32}$$

for $|s_j(q^*)| > \delta_K$ and $\alpha_{0j} = \rho_{0j} = 0$ otherwise. Furthermore, for the purpose of numerical computation, we define the matrix

$$H(t) = \Psi_0(t)\Psi_0^\top(t) =: \begin{bmatrix} H_{11}(t) & H_{12}(t) & H_{13}(t) \\ H_{21}(t) & H_{22}(t) & H_{23}(t) \\ H_{31}(t) & H_{32}(t) & H_{33}(t) \end{bmatrix}. \tag{3.33}$$

With this notation, $M(t)$ corresponds to

$$M(t) = \begin{bmatrix} \int_t^{t+T} H_{11}(\tau)d\tau & \int_t^{t+T} H_{12}(\tau)d\tau & \int_t^{t+T} H_{13}(\tau)d\tau \\ \int_t^{t+T} H_{21}(\tau)d\tau & \int_t^{t+T} H_{22}(\tau)d\tau & \int_t^{t+T} H_{23}(\tau)d\tau \\ \int_t^{t+T} H_{31}(\tau)d\tau & \int_t^{t+T} H_{32}(\tau)d\tau & \int_t^{t+T} H_{33}(\tau)d\tau \end{bmatrix}.$$

In order to integrate the nine functions $H_{ij}(\tau)$ over $\begin{bmatrix} t & t+T \end{bmatrix}$, as illustrated in the figure below,

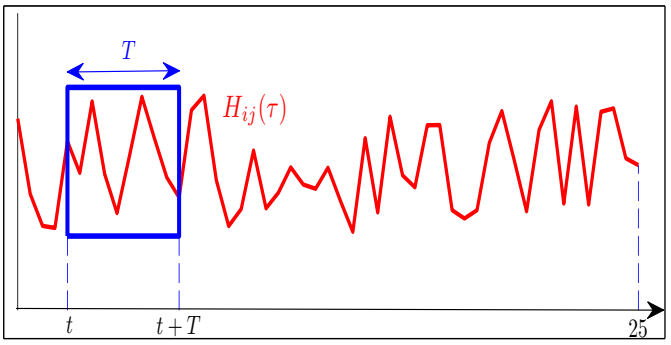

FIGURE 3.13: Window of integration of the function $Hij(\tau)$.

MATLAB™ offers different options to integrate functions expressed in closed forms as well as data vectors. Given the complexity of the function $M(t)$, we use the MATLAB™built-in function

$$\texttt{trapz(X,Y)} := \int_{X(i)}^{X(f)} Y dX.$$

Example 2.1. The defined integral of $y(x) = \sin(x)$ between 0 and π is 2 ,

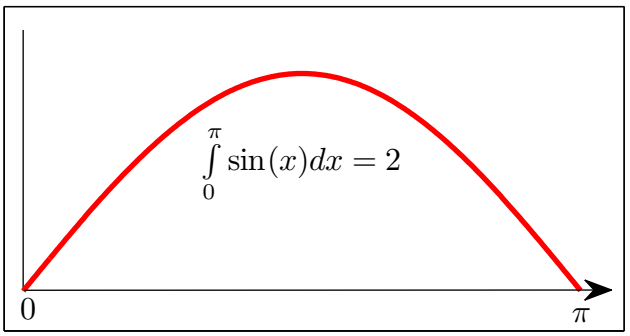

FIGURE 3.14: Defined integral of $\sin(x)$ between 0 and π.

we compute this integral by using MATLAB™function `trapz(X,Y)` and the following MATLAB™code:

```
X=0:pi/100:pi; %build a data vector with entries from 0 to pi with
    increments of pi/100
Y=sin(X); %computes vector Y, where  each entry i corresponds to sin(X(i))
q=trapz(X,Y) % Computes integral of Y with respect to X
```

The code gives as result $q = 1.9998$. In fact, a little lower than the correct value 2, the error comes from the magnitude $\pi/100$ of increments in X, in fact, the smaller the increments, the better the result of q. For instance, building $X = 0 : \pi/200 : \pi$, we obtain as result $q = 2.0$, which is the exact value.

This function allows one to integrate a data vector Y with respect to a data vector X by using the trapezoidal method of integration.

3.6.1.1 Integrating the data results

To integrate the data vector H_{ij} -see Equation (3.33)- with respect to a *time* data vector T_v over a time window of width $T = 500$[ms], see Figure 3.13, we proceed as follows:

1. We build a data vector of time $T_v = \begin{bmatrix} 0 & t_i & 2t_i & \dots & 27 \end{bmatrix}$, where $t_i = 1\text{x}10^{-5}$ is the fixed step of integration. Consequently, T_v is a data vector with $\frac{27}{t_i} + 1 = 27\text{x}10^5 + 1$ elements
2. We run a simulation in SIMULINK™ to obtain nine data vectors H_{kl} as defined in (3.33)
3. For each $t \in [0, 25]$,
   - 3.1. we build a data vector t_T by taking $\frac{T}{t_i} = 5\text{x}10^4$ elements from T_v, starting at the element $\frac{t}{ti} + 1$ down to the element $\frac{t+T}{ti} + 1$.
   - 3.2. we build nine data vectors H_{Tkl} by taking T/t_i elements from H_{kl} for $k = \{1, 2, 3\}$ and $l = \{1, 2, 3\}$, starting at the element $\frac{t}{ti} + 1$ down to the element $\frac{t+T}{ti} + 1$.
   - 3.3. by using MATLAB™command `trapz(X,Y)` we compute

$$iH_{kl} = trapz(t_T, H_{Tkl}) \quad \text{for} \quad k = \{1, 2, 3\} \quad \text{and} \quad l = \{1, 2, 3\}$$

3.4. we build the matrix $M(t)$ as

$$M(t) = \begin{bmatrix} iH_{11} & iH_{12} & iH_{13} \\ iH_{21} & iH_{22} & iH_{23} \\ iH_{31} & iH_{32} & iH_{33} \end{bmatrix}$$

and compute the three eigenvalues $\lambda(t) = eig(M(t))$

The above procedure is programed in MATLAB™and the code is available in Appendix A.4. As result we obtain a data matrix $\Lambda \in \mathbb{R}^{\frac{T}{t_i}\text{x}3}$ where each row contains the three eigenvalues $\lambda(t)$ corresponding to a given time instant t. From the Figure 3.15 it is easily noted that the all of the eigenvalues are positive for all $t \in [0, 25]$, consequently the persistency of excitation condition is satisfied, albeit on the window of integration.

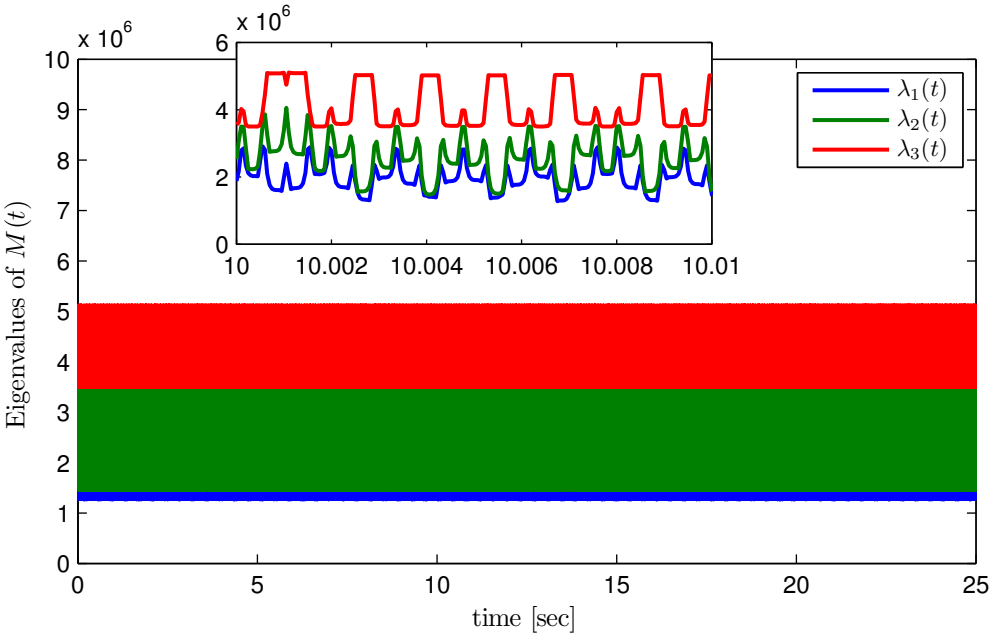

FIGURE 3.15: Eigenvalues of $M(t)$ for all $t \in [0, 25]$.

3.7 Concluding Remarks

We presented a robust adaptive controller for the switched-reluctance motor, considering both the stator and rotor dynamics via fairly simple control laws (PID, approximate differentiation), widely used in control practice. Although our results guarantee robustness with respect to bounded disturbances (possibly unmodelled dynamics) it is of utmost importance in motor control, to design controllers with guaranteed performance. Further ongoing research focuses on avoiding the use of position measurements.

Chapter 4

A novel PID-based control approach for switched-reluctance motors

As previously explained the control approach that we follow in this thesis relies on the ability to split the control problem into one for the electrical part and one for the mechanical part. The control action on the rotor dynamics enters through the mechanical torque; naturally, the current x may be seen as a virtual control input. Accordingly, a control law u must be designed for the stator equations and implemented by applying the corresponding input voltage (via the torque share approach). The control u must be such that the actual current x tracks a desired reference x^* which is viewed as the control law for the rotor electric equations. See Figure 4.1.

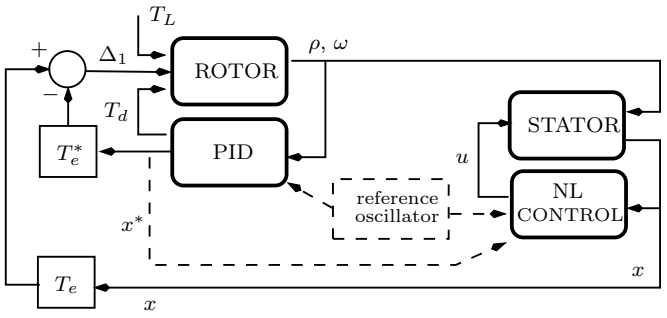

FIGURE 4.1: Illustration of the control approach. A PID controller virtually injected through the variable T_d steers $\omega \to \omega^*$ –See Section 4.3. T_d is also injected in the form of a reference current x^* into the stator control loop and a nonlinear controller ensures current tracking control –see Section 4.4. The systems are feedback interconnected through the nonlinear map T_e. The proper definition of the reference model (dashed lines) ensures that the interconnection remains stable in view of a small-gain argument –see Section 4.5.

However appealing this approach is, it is stymied by two major technical difficulties:

- the rotor equation is non-affine in the 'control input' x,
- the mechanical position appears non-linearly.

The first difficulty is addressed in Section 4.2 via the so-called *torque-sharing* approach. The second, which presents an obstacle to observer-design and output-feedback control, is circumvented

by using an alternative dynamic model in new coordinates. Such model, presented in Section 4.1, is propitious to certainty-equivalence control since it is linear in the unmeasured variables. Indeed, the rotor dynamics model in the new coordinates lends itself naturally to the design of Luenberger-type observers.

For clarity of exposition, we divide the rest of the chapter in three parts that are coherent with the control approach described above. First, in Section 4.3, we discuss the control of the rotor dynamics (design of T_d) then, we present a tracking ($x \to x^*$) control law u for the stator dynamics in Section 4.4. Finally, using a small-gain argument we establish, that the interconnection of the two subsystems, schematically represented in Figure 4.1, is exponentially stable.

4.1 Motor model for control purposes

We use a change of coordinates to state a new system equation equivalent to the simplified model (3.8) in q coordinates. The main advantage of this model consists in the linearity of the map from "position" to inductance.

Following ideas from [59] we introduce the function $\varrho : [-\pi, \pi] \to \mathbb{S}^a$ where $\mathbb{S}^a := \{(\varrho_1, \varrho_2) \in \mathbb{R}^2 : \varrho_1^2 + \varrho_2^2 = a\}$, with $a \in \mathbb{R}_+$. Let $\vartheta \in [-\pi, \pi]$, $A > 0$ and

$$\begin{aligned} \varrho_1 &:= A\cos\big(N_r[q+q_0]\big) \\ \varrho_2 &:= A\sin\big(N_r[q+q_0]\big). \end{aligned}$$

Now, if we set $q_0 = -q(0)$ and for any $\rho_\circ \in \mathbb{R}_+$, we see that the solutions of

$$\dot\rho = \omega\mathbb{J}\rho, \quad \rho = [\rho_1, \rho_2]^\top, \quad \rho(0) = [\rho_\circ, 0]^\top$$

where

$$\mathbb{J} = N_r \begin{bmatrix} 0 & -1 \\ 1 & 0 \end{bmatrix}.$$

satisfy $\rho(t) \in \mathbb{S}^{\rho_\circ}$ for all $t \geq 0$ and are given by $\rho(t) = \varrho(q(t))$ *i.e.*,

$$\begin{aligned} \rho_1(t) &= \rho_\circ\cos\big(N_r[q(t)-q(0)]\big) \\ \rho_2(t) &= \rho_\circ\sin\big(N_r[q(t)-q(0)]\big). \end{aligned}$$

The electromagnetic torque

$$T_e(\rho, x) = \frac{1}{2}x^\top K(\rho)x \tag{4.2}$$

is now expressed as a function of ρ as well as the inductance matrix $K(\rho) = \ell_1 N_r K'(\rho)$ where

$$K'(\rho) = \begin{bmatrix} \rho_2 & 0 & 0 \\ 0 & \frac{1}{2}\left(\rho_2 - \sqrt{3}\rho_1\right) & 0 \\ 0 & 0 & \frac{1}{2}\left(\rho_2 + \sqrt{3}\rho_1\right) \end{bmatrix}$$

and $L(\rho) = \ell_0 I + \ell_1 L'(\rho)$ with

$$L'(\rho) = \begin{bmatrix} -\rho_1 & 0 & 0 \\ 0 & -\frac{1}{2}\left(\rho_1 + \sqrt{3}\rho_2\right) & 0 \\ 0 & 0 & -\frac{1}{2}\left(\rho_1 - \sqrt{3}\rho_2\right) \end{bmatrix}.$$

Note that, although T_e in (4.2) and $\mathbf{T}_e$ in (3.9) are different functions $T_e(\rho(q), x)$ and $\mathbf{T}_e(q, x)$ represent the same quantity. The same applies for $L(\rho)$ and $K(\rho)$ in this chapter when they are compared to $L(q)$ and $K(q)$ in Chapter 3. Consequently, it is clear that there exist positive constants ℓ_m, ℓ_M, k_m and k_M such that

$$\ell_m \leq |L(\rho)| \tag{4.3a}$$

$$\ell_M |\rho_1 - \rho_2| \geq \max\left\{|L(\rho_1 - \rho_2)|, |L(\rho_1) - L(\rho_2)|\right\} \tag{4.3b}$$

$$k_M |\rho_1 - \rho_2| \geq \max\left\{|K(\rho_1 - \rho_2)|, |K(\rho_1) - K(\rho_2)|\right\}. \tag{4.3c}$$

Considering these new definitions, the motor dynamic is described by equations:

$$L(\rho)\dot{x} + K(\rho)\omega x + Rx = u \tag{4.4a}$$

$$\dot{\rho} = \omega \mathbb{J} \rho \tag{4.4b}$$

$$J\dot{\omega} = T_e(\rho, x) - T_L(q, \dot{q}). \tag{4.4c}$$

The advantage of the model (4.4) is that it is linear in the new 'position' variables ρ, hence, it is propitious for certainty-equivalence, observer-based control.

4.2 Torque sharing technique in ρ-coordinates

As illustrated in Figure 4.1, the control approach relies on the ability to control the rotor dynamics via the stator currents x provided, this technique is used to induce a virtual control input into the mechanical Equation (4.4c). Ideally, the virtual control input enters through the mechanical torque $T_e(\rho, x)$. That is, given a control law T_d, one must solve the equation

$$\frac{T_e^*(\rho, x^*)}{J} = T_d \tag{4.5}$$

for the current reference x^*. Using Equation (4.5), mechanical subsystem Equation (4.4c) may be equivalently written as:

$$J\dot{\omega} = \overbrace{JT_d}^{T_e^*(\cdot)} - T_L + \overbrace{[T_e(\rho, x) - T_e^*(\rho, x^*)]}^{\tilde{T}_e}$$

which, for control purposes, may be viewed as a nominal system $\dot{\omega} = T_d - T_L/J$ perturbed by the term $[T_e - T_e^*]$. By design, T_d is such that $\omega \to \omega^*$ provided that $[T_e - T_e^*] \equiv 0$. Note that $[T_e - T_e^*]$ vanishes provided that current reference trajectories x^* are asymptotically tracked.

Clearly, the difficulty to solve (4.5) relies on the fact that T_e^*, after (4.2), is quadratic in x^*. The torque sharing approach as used in [33, 34, 54] and Chapter 3, exploits the fact that the mechanical torque T_e corresponds to the sum of torques due to each phase therefore, we define

$$T_e^* = N_r \ell_1 \frac{1}{2}\Big[K_1'(\rho){x_1^*}^2 + K_2'(\rho){x_2^*}^2 + K_3'(\rho){x_3^*}^2\Big]. \tag{4.6}$$

with $K_j(\rho)$ the entries in the diagonal of matrix $K'(\rho)$. Now we solve (4.5) for x_j^* after (4.6) to obtain

$$x_j^* = \begin{cases} \left[\dfrac{2J}{N_r \ell_1}\right]^{1/2} \left[\dfrac{m_j(\rho) T_d}{K_j'(\rho)}\right]^{1/2} & \text{if } K_j'(\rho) \neq 0 \\ 0 & \text{otherwise} \end{cases} \tag{4.7}$$

where the functions m_j ensure that x_j exists for any ρ^* and any T_d. That is, depending on the current phase of the reference model, the function m_j ensures that the respective signs of the numerator and of the denominator in the previous expression are equal for *at least one* $j \in \{1, 2, 3\}$. To that end, we define the sets

$$\Theta_j^+ = \big\{\rho \in \mathbb{S}^\rho : K_j'(\rho) \geq 0\big\}$$
$$\Theta_j^- = \big\{\rho \in \mathbb{S}^\rho : K_j'(\rho) < 0\big\}$$

where the superscripts $^+$ and $^-$ stand for required positive and negative torque respectively. Accordingly, given T_d, we define

$$m_j(\rho) = \begin{cases} m_j^+(\rho) & \text{if} \quad T_d \geq 0, \\ m_j^-(\rho) & \text{if} \quad T_d < 0. \end{cases}$$

where

$$m_j^+(\rho) > 0 \quad \forall \rho \in \Theta^+, \qquad m_j^+(\rho) = 0 \quad \forall \rho \in \Theta^-,$$
$$m_j^-(\rho) > 0 \quad \forall \rho \in \Theta^-, \qquad m_j^-(\rho) = 0 \quad \forall \rho \in \Theta^+.$$

Moreover, we impose that

$$\sum_{j=1}^{3} m_j^+(\rho) = 1, \qquad \sum_{j=1}^{3} m_j^-(\rho) = 1.$$

so we have

$$T_d = T_d \sum_{j=1}^{3} m_j(\rho)$$

and (4.5) holds.

4.3 Rotor robust state-feedback control

In this section we present two results on robust state-feedback control of the rotor dynamics. In the first case, we establish a result of practical stability with respect to the uncompensated constant disturbance induced by the load-torque; in the second case, we add an integrator to establish global exponential stability. In both scenarios we recover a property of input-to-state stability with respect to external inputs. This is significant to analyze the stability of the system interconnected with the stator dynamics.

For the purpose of tracking control we introduce a reference oscillator dynamics for (4.4b). Given a desired constant reference ω^*, we introduce q^* as the angular position reference for q that is, $\dot{q}^* = \omega^*$ and the reference oscillator dynamics

$$\dot{\rho}^* = \omega^* \mathbb{J} \rho^*, \quad \rho^*(0) = [\rho_\circ^*, 0]^\top \tag{4.8}$$

where the initial condition $\rho_\circ^* \in \mathbb{R}_+$ is a free design parameter. The solutions to (4.8) which define the angular reference trajectories, are

$$\rho^*(t) = \rho_\circ^* \begin{bmatrix} \cos\left(N_r[q^*(t) - q^*(0)]\right) \\ \sin\left(N_r[q^*(t) - q^*(0)]\right) \end{bmatrix} \tag{4.9}$$

where $q^*(t) = \omega^* t + q^*(0)$ and the initial reference angular position $q^*(0) \in [-\pi, \pi]$; without loss of generality we fix $q^*(0) = 0$. Note that $\rho^*(t) \in \mathbb{S}^{\rho_\circ^*}$ for all $t \geq 0$.

4.3.1 Control without load compensation

Let $\nu^* = \frac{T_L}{J}$ then, the rotor model is given by

$$\dot{\omega} = \frac{T_e}{J} - \nu^* \tag{4.10a}$$

$$\dot{\rho} = \omega \mathbb{J} \rho. \tag{4.10b}$$

Define the position error $e_\rho := \rho - \rho^*$ and the velocity error $e_\omega := \omega - \omega^*$ then, according to the policy described in Section 4.2, we pose the state-feedback control law

$$T_d = -k_d e_\omega - k_p \rho^{*\top} \mathbb{J}^\top e_\rho + \nu + \dot{\omega}^*. \tag{4.11}$$

Define further $\tilde{\nu} := \nu - \nu^*$ and add $T_d - T_e^*/J$ to the right-hand side of Equation (4.10a). Then, the latter may be rewritten as

$$\dot{e}_\omega = -k_d e_\omega - k_p {\rho^*}^\top \mathbb{J}^\top e_\rho + \tilde{\nu} + \Delta_1(t, y, e_x) \tag{4.12a}$$

$$\Delta_1(t, y, e_x) = \frac{1}{2J}(e_x + 2x^*)^\top K(\rho) e_x \tag{4.12b}$$

where $y = \begin{bmatrix} e_\rho & e_\omega & \tilde{\nu} \end{bmatrix}^\top$, x^* is a function of t and y, and $\rho = e_\rho + \rho^*(t)$. Subtracting (4.8) from (4.10b) and defining $v = \Delta_1 + \tilde{\nu}$, the mechanical error dynamics becomes

$$\dot{e}_\omega = -k_d e_\omega - k_p \rho^*(t)^\top \mathbb{J}^\top e_\rho + v \tag{4.13a}$$

$$\dot{e}_\rho = e_\omega \mathbb{J}\rho^*(t) + \omega \mathbb{J} e_\rho \tag{4.13b}$$

which may be viewed as a non-autonomous periodic system perturbed by the input v. The interest of this observation relies on the following statement.

Proposition 4.1 (Global exponential stability by state-feedback, no load)**.** *Provided that k_p, k_d are positive, the system (4.13) is input-to-state-stable with respect to the input v and the map $v \to e_\omega$ is output-strictly passive. In addition, in the case that $v \equiv 0$ the origin $(e_\rho, e_\omega) = (0, 0)$ of (4.13) is globally exponentially stable.*

Proof. Consider the positive definite radially unbounded function V_{c1},

$$V_{c1}(e_\omega, e_\rho) = \frac{1}{2}\left(e_\omega^2 + k_p \left|e_\rho\right|^2\right)$$

whose time derivative along the trajectories of (4.13) yields

$$\dot{V}_{c1}(e_\omega, e_\rho) = -k_d e_\omega^2 + e_\omega v\,. \tag{4.14}$$

Output strict passivity of the map $v \mapsto e_\omega$ follows by integrating on both sides of (4.14) since $V_{c1} \geq 0$. The proof of global asymptotic stability under the condition $v \equiv 0$, follows invoking Lasalle's theorem for periodic systems –see *e.g.* [60, Theorem 5.3.79]: note that $e_w = 0$ implies that $\dot{V}_{c1} = 0$ and the only solution of $k_p \rho^*(t)^\top \mathbb{J}^\top e_\rho = 0$ for any t, is $e_\rho = 0$ that is, the origin is the largest invariant set contained in $\{\dot{V}_{c1} = 0\}$. Global exponential stability is established invoking standard results from adaptive control literature, observing that $\mathbb{J}\rho^*(t)$ is persistently exciting that is, there exist T_c and $\mu_c > 0$ such that

$$\int_t^{t+T_c} \mathbb{J}\rho^*(\tau)\rho^*(\tau)^\top \mathbb{J}^\top d\tau = N_r^2 \rho_0^{*2} \int_t^{t+T_c} \Upsilon(\tau) d\tau \geq \mu_c I. \tag{4.15}$$

where $\Upsilon(t)$ is defined in Section B.1 on page 91. As a matter of fact, (4.15) holds with $T_c = \pi/N_r\omega^*$ and $\mu_c = \left|\rho_\circ^*\right|^2 N_r^2 T_c/2$ –see properties of matrix $\Upsilon(t)$ in Appendix B.1. Input-to-state stability follows from the following statement.

Lemma 4.1. *Let $\varepsilon_1 \in (0,1)$ be a small parameter to be defined, let $i \in \{1,\dots 6\}$, $\lambda_i \geq 0$ be such that $\sum_{i=1}^{6} \lambda_i = 1$, $k_{di} := \lambda_i k_d$ and $\bar{k}_{dj} := \sum_{i=j}^{6} k_{di}$; similarly for k_p. Define the functions V_{c2}, V_{c3} by*

$$V_{c2}(t, e_\omega, e_\rho) = \varepsilon_1 e_\omega \rho^*(t)^\top \mathbb{J}^\top e_\rho \tag{4.16a}$$

$$V_{c3}(t, e_\rho) = -e_\rho^\top \int_t^{t+T_c} e^{(t-\tau)} \mathbb{J} \rho^*(\tau) \rho^*(\tau)^\top \mathbb{J}^\top d\tau e_\rho \,. \tag{4.16b}$$

Then, if

$$|\rho_\circ^*| \geq \frac{N_r}{2} e^{\pi / N_r \omega^*} \tag{4.17}$$

we have

$$\begin{aligned} \sum_{i=1}^{3} \dot{V}_{ci} \leq & -\bar{k}_{d3} e_\omega^2 - \frac{N_r \pi}{2\omega^*} |\rho_\circ^*| \left(|\rho_\circ^*| \, e^{-\pi/\omega^*} - \frac{N_r}{2} \right) |e_\rho|^2 \\ & -\varepsilon_1 \bar{k}_{p3} \left[\rho^{*\top} \mathbb{J}^\top e_\rho \right]^2 + \left(\varepsilon_1 \left[\rho^{*\top} \mathbb{J}^\top e_\rho \right] + e_\omega \right) v. \end{aligned} \tag{4.18}$$

The proof of Lemma 4.1 is included in Appendix B. Input-to-state stability with respect to the input v follows remarking that $\sum_{i=1}^{3} V_{ci}$ is an input to state stable-Lyapunov function; indeed, it is enough to choose a constant α sufficiently small such that $|v| \leq \alpha \, |e_\omega, e_\rho|$ implies that $\sum_{i=1}^{3} \dot{V}_c$ is negative definite. □

4.3.2 With compensation of unknown load

In the previous section, Proposition 4.1 establishes global exponential stability for the system without load torque. As a byproduct, the system is robust with respect to additive disturbances such as torque-load uncertainty ($\tilde{\nu} = \text{const.}$). By exploiting the passivity of (4.13) we add a second loop which we close with integral action, to compensate for $\tilde{\nu}$. That is, let the variable ν in (4.11) be defined by

$$\dot{\nu} = -k_i \left(e_\omega + \varepsilon_1 \left[\rho^{*\top} \mathbb{J}^\top e_\rho \right] \right), \quad k_i > 0, \tag{4.19}$$

then, the map $\left(e_\omega + \varepsilon_1 \left[\rho^{*\top} \mathbb{J}^\top e_\rho \right] \right) \mapsto \nu$ is passive, the passivity and robustness properties of (4.13) are conserved.

Proposition 4.2 (Global exponential stability by state-feedback, with load compensation)**.** *The system (4.13) with $v = \tilde{\nu} + \Delta_1$ is input-to-state-stable with respect to Δ_1 and the map $\Delta_1 \mapsto \left(e_\omega + \varepsilon_1 \left[\rho^{*\top} \mathbb{J}^\top e_\rho \right] \right)$ is output-strictly passive. Moreover, if $\Delta_1 \equiv 0$ that is if $v = \tilde{\nu}$, then the origin $(e_\rho, e_\omega, \tilde{\nu}) = (0,0,0)$ of (4.13) is globally exponentially stable for appropriate values of the gains k_p, k_d and k_i.*

Proof. Consider the system (4.13) with $v = \tilde{\nu} + \Delta_1$ and the function

$$V_{c4}(\tilde{\nu}) := \frac{1}{2k_i}\tilde{\nu}^2.$$

The total time derivative of $\sum_{i=1}^{4} V_{ci}$ along the trajectories of (4.13), and

$$\dot{\tilde{\nu}} = -k_i \left(e_\omega + \varepsilon_1 \left[\rho^{*\top} \mathbb{J}^\top e_\rho \right] \right), \quad k_i > 0 \tag{4.20}$$

satisfies (4.18) with $v = \Delta_1$. Integrating the resulting expression of $\sum_{i=1}^{4} \dot{V}_{ci}$ on both sides, we see that the map $\Delta_1 \mapsto \left(e_\omega + \varepsilon_1 \left[\rho^{*\top} \mathbb{J}^\top e_\rho \right] \right)$ is output-strictly passive. Furthermore, if $\Delta_1 \equiv 0$ global asymptotic stability follows invoking Lasalle's principle, as in the proof of Proposition 4.1.

Now we proceed to show that $\sum_{i=1}^{5} V_{ci}$ with

$$V_{c5}(e_\rho, e_\omega, \tilde{\nu}) := -\varepsilon_3 \tilde{\nu} e_\omega - \frac{1}{2}\varepsilon_1 \varepsilon_3 k_i \left| e_\rho \right|^2$$

qualifies as an input-to-state-stable-Lyapunov function. The total time derivative of V_{c5} along the trajectories generated by (4.13), (4.20) yields

$$\begin{aligned} \dot{V}_{c5} \;=\; & \varepsilon_3 k_i \left(e_\omega + \varepsilon_1 \left[\rho^{*\top} \mathbb{J}^\top e_\rho \right] \right) e_\omega \\ & -\varepsilon_3 \tilde{\nu}^2 - \varepsilon_3 \tilde{\nu} \left(-k_d e_\omega - k_p \rho^{*\top} \mathbb{J}^\top e_\rho + \Delta_1 \right) \\ & -\varepsilon_1 \varepsilon_3 k_i e_\rho^\top \left[\omega \mathbb{J} e_\rho + e_\omega \mathbb{J} \rho^* \right]. \end{aligned}$$

Adding $\dot{V}_{c4}$ and the latter to (4.18), we obtain

$$\begin{aligned} \sum_{i=1}^{5} \dot{V}_{ci} \;\leq\; & -[\bar{k}_{d4} - \varepsilon_3 k_i] e_\omega^2 - \frac{N_r \pi}{2\omega^*} \left| \rho_\circ^* \right| \left(\left| \rho_\circ^* \right| e^{-\pi/N_r \omega^*} - \frac{N_r}{2} \right) |e_\rho|^2 - \varepsilon_1 \bar{k}_{p4} \left[\rho^{*\top} \mathbb{J}^\top e_\rho \right]^2 - \frac{\varepsilon_3}{2} \tilde{\nu}^2 \\ & - \delta_2 + \Delta_1 \left(\varepsilon_1 \left[\rho^{*\top} \mathbb{J}^\top e_\rho \right] + e_\omega - \varepsilon_3 \tilde{\nu} \right) \end{aligned} \tag{4.21}$$

where we recall (see Lemma 4.1) that $\bar{k}_{dj} = \sum_{i=j}^{6} k_{di}$, $k_{di} = \lambda_i k_d$ $\lambda_i \in (0,1)$ (similarly for k_p) and we defined

$$\delta_2 := \frac{1}{2} \begin{bmatrix} e_\omega \\ \rho^{*\top} \mathbb{J}^\top e_\rho \\ \tilde{\nu} \end{bmatrix} \begin{bmatrix} 2k_{d3} & 0 & \varepsilon_3 k_d \\ 0 & 2\varepsilon_1 k_{p3} & \varepsilon_3 k_p \\ \varepsilon_3 k_d & \varepsilon_3 k_p & \varepsilon_3 \end{bmatrix} \begin{bmatrix} e_\omega \\ \rho^{*\top} \mathbb{J}^\top e_\rho \\ \tilde{\nu} \end{bmatrix}.$$

Let ε_3 satisfy

$$\min \left\{ \frac{k_{d4}}{k_i}, \; \frac{\lambda_3}{k_d}, \; \frac{\varepsilon_1 \lambda_3}{k_p} \right\} \geq \varepsilon_3 \tag{4.22}$$

then, $\delta_2 \geq 0$ and $\sum_{i=1}^{5} V_{ci}$ is an input-to-state-stable-Lyapunov function for the system (4.13)-(4.21), with $v = \tilde{\nu} + \Delta_1$, with respect to the input Δ_1. Furthermore, if $\Delta_1 \equiv 0$, $\sum_{i=1}^{5} \dot{V}_{ci}$

is bounded by a quadratic negative definite function of the state; global exponential stability follows invoking standard Lyapunov theory. □

4.4 Stator robust state-feedback control

In the previous section we established input-to-state stability for the rotor dynamics with respect to inputs Δ_1 which vanish with $e_x = x - x^*$. In this section we focus on the tracking control of the stator dynamics that is, the control goal is to make $x \to x^*$ where $x^* := [x_1^* \, x_2^* \, x_3^*]^\top$ and the latter is defined by (4.7). The controller that we propose next establishes global exponential stability in the case of perfect velocity tracking ($e_\omega = 0$) and input-to-state stability with respect to external inputs, which vanish as $e_w \to 0$.

For Equation (4.4a) we introduce the control law

$$u^*(t,x) := L(\rho^*)\dot{x}^* + K(\rho^*)\omega^* x + Rx^* - k_{px}e_x$$

where k_{px} is shorthand notation for $k_{px}(t,|e_x|)$ and is defined by a continuous function $k_{px} : \mathbb{R}_+ \times \mathbb{R}_+ \to \mathbb{R}_+$ such that $k_{px}(t,\cdot)$ is non-decreasing. Note that $\dot{x}^*$ is a function of time, $\dot{T}_d$ and T_d which depend only on measured states and computed quantities. Indeed, defining

$$\sigma_j(\rho) := \frac{m_j(\rho)}{K_j'(\rho)}$$

we have, after (4.7),

$$\dot{x}_j^* = \begin{cases} \left[\dfrac{2J}{\ell_1}\right]^{1/2} [\sigma_j(\rho)T_d]^{-1/2} \left[\dot{\sigma}_j T_d + \sigma_j \dot{T}_d\right] & \text{if } K_j'(\rho) \neq 0 \\ 0 & \text{otherwise.} \end{cases} \tag{4.23}$$

Applying $u = u^*$ into (4.4a) we see that

$$L(\rho)\dot{e}_x + [R + k_{px}]\, e_x = \Delta_2(t, e_\rho, e_x, \dot{x}^*) \tag{4.24a}$$

$$\Delta_2(t, e_\rho, e_x, \dot{x}^*) = -\left[L'(e_\rho)\dot{x}^* + K(e_\rho)\omega^* x + K(\rho)e_\omega x\right] \tag{4.24b}$$

and, from (4.3) we have

$$|\Delta_2| \leq \left[\ell_M |\dot{x}^*| + k_M \omega^* |x|\right] |e_\rho| + k_M |\rho_\circ^*|\, |x|\, |e_\omega| \,.$$

That is, the origin $\{e_x = 0\}$ of the the stator closed-loop system is exponentially stable in the case that the rotor controller achieves perfect velocity tracking. Global exponential stability for (4.24) implies local input-to-state stability; the global property is established next.

Proposition 4.3. *Let* $\rho_\circ = \rho_\circ^*$ *and let*[1].

$$u = u^* - \left[\ell_M \left|\dot{x}^*\right| + k_M \omega^* \left|x\right|\right] \left|e_\rho\right| sgn(e_x)\,. \tag{4.25}$$

Assume further that

$$k_{px} := k_{px1} + \frac{1}{2}\left[k_M \left|\rho_\circ^*\right| \left|x\right|\right]^2, \quad k_{px1} > 0 \tag{4.26}$$

then, the closed-loop system (4.4a) with (4.25) is input-to-state stable from the input e_ω*. Moreover, in the case that* $|\Delta_2| \equiv 0$*, the origin* $\{e_x = 0\}$ *is globally exponentially stable with* $u = u^*$ *and* $k_{px} := k_{px1}$*.*

Proof. The total time derivative of

$$V_{c6}(e_x) := \frac{1}{2}\left|e_x\right|^2$$

along the closed-loop trajectories [2] (4.24) yields

$$\dot{V}_{c6} \leq -[R + k_{px}]\left|e_x\right|^2 + \left[k_M \left|\rho_\circ^*\right| \left|x\right|\right] \left|e_\omega\right| \left|e_x\right|$$

which, in view of (4.26), implies that

$$\dot{V}_{c6} \leq -[R + k_{px1}]\left|e_x\right|^2 + \frac{1}{2}\left|e_\omega\right|^2 \tag{4.27}$$

hence, V_{c6} is an ISS-Lyapunov function for the stator closed-loop system. The proof of the second statement follows directly observing that $|\Delta_2| = 0$ implies that $\dot{V}_{c6} \leq -[R + k_{px}]\left|e_x\right|^2$. □

4.5 Robust control of switched-reluctance motor

Now we present our main results, we establish global exponential stability for the controlled switched-reluctance via state feedback. We also establish that the interconnection of the two control loops for the rotor dynamics and the stator dynamics, remains input-to state stable with respect to external inputs.

Proposition 4.4. *Consider the SRM model (4.4) under the assumption of relatively low current in closed loop and the electric controller defined by equations (4.25), (4.23) and (4.7). Moreover, consider the pid control (4.11) with* $\rho_\circ = \rho_\circ^*$*. Let the gain* k_{px} *of the electric controller be given by (4.26) where*

$$k_{px1} \geq \frac{1}{2}\left[k_M \left|\rho_\circ^*\right| \left(\left|x^*\right| + \left|x\right|\right)\right]^2 (\varepsilon_1 + 2\varepsilon_3 + 1) \tag{4.28}$$

where ε_1 *and* ε_3 *are small positive constants and let (4.17) hold. Then, the origin of the closed-loop system is globally exponentially stable.*

[1] By an abuse of notation, the vector $\text{sgn}(e_x) = \text{col}[\text{sign}(e_{xi})]$, where the sign function is defined as $\text{sign}(0) \in [-1, 1]$ and $\text{sign}(x) = \text{abs}(x)/x$ if $x \neq 0$

[2] It is considered that solutions are defined in Filippov's sense.

Proof. The motor model corresponds to the Equations (4.4). Therefore, the closed-loop system corresponds to (4.12), (4.13b), (4.20) and (4.24). The term Δ_1 in (4.12b) satisfies, using $|K(\rho)| \leq k_M \, |\rho_\circ^*|$,

$$|\Delta_1| \leq \frac{k_M}{J} \, |\rho_\circ^*| \, |e_x| \, \Big[\, |x^*| + |x| \, \Big].$$

In view of the latter, (4.21), (4.22) and (4.27), it follows that the total time derivative of $V_c := \sum_{i=1}^{6} V_{ci}$ satisfies

$$\begin{aligned} \dot{V}_c \;\leq\; & -[\bar{k}_{d5} - 0.5]e_\omega^2 - \left[\frac{N_r \pi}{2\omega^*} \, |\rho_\circ^*| \left(|\rho_\circ^*| \, e^{-\pi/N_r\omega^*} - \frac{N_r}{2} \right) \right] |e_\rho|^2 - \varepsilon_1 \bar{k}_{p4} \left[\rho^{*\top} \mathbb{J}^\top e_\rho \right]^2 - \frac{\varepsilon_3}{2} \tilde{\nu}^2 \\ & -[R + k_{px1}] \, |e_x|^2 + \frac{k_M}{J} \, |\rho_\circ^*| \, |e_x| \, \Big[\, |x^*| + |x| \, \Big] \left(\varepsilon_1 \left| \rho^{*\top} \mathbb{J}^\top e_\rho \right| + |e_\omega| + \varepsilon_3 \, |\tilde{\nu}| \right) \end{aligned}$$

which, in virtue of the triangle inequality, (4.28) and provided that k_{p4}, $k_{d5} \geq 1$, implies that

$$\dot{V}_c \;\leq\; -W(e_x, e_\rho, e_\omega, \rho^{*\top} \mathbb{J}^\top e_\rho) \tag{4.29a}$$

$$\begin{aligned} W \;\leq\; & \bar{k}_{d6} e_\omega^2 + \left[R + \frac{1}{2} k_{px1} \right] |e_x|^2 + \varepsilon_1 \bar{k}_{p5} \left[\rho^{*\top} \mathbb{J}^\top e_\rho \right]^2 + \frac{\varepsilon_3}{4} \tilde{\nu}^2 \\ & + \left[\frac{N_r \pi}{2\omega^*} \, |\rho_\circ^*| \left(|\rho_\circ^*| \, e^{-\pi/N_r\omega^*} - \frac{N_r}{2} \right) \right] |e_\rho|^2 \end{aligned} \tag{4.29b}$$

hence, $\dot{V}_c$ is negative definite. Global exponential stability follows invoking standard Lyapunov theory. Now, let v_m and v_s be bounded external inputs and reconsider (4.13a) with $v = \tilde{\nu} + \Delta_1 + v_m$ and let $u = u^* + v_s$. Then, from the previous development we obtain

$$\dot{V}_c \;\leq\; W(e_x, e_\rho, e_\omega, \rho^{*\top} \mathbb{J}^\top e_\rho) + e_x v_s + v_m \left(\varepsilon_1 \left[\rho^{*\top} \mathbb{J}^\top e_\rho \right] + e_\omega - \varepsilon_3 \tilde{\nu} \right)$$

That is, V_c qualifies as an input to state-Lyapunov function for the closed-loop system with inputs v_s, v_m. □

4.6 Simulation results

We have tested our *PID+Feedback* controller on a fully-nonlinear model $\dot{\psi}_j(q, x) + Rx_j = u_j$ where, for implementation purpose we have used the flux expression $\psi_j(q, x_j) = \psi_s \left(1 - e^{-f_j(q) x_j} \right)$ from Equation (3.2). In Figure 4.2 we show the implementation diagram of the simulation.

The numerical simulations were carried out in the software SIMULINK™ of MATLAB™. The physical parameters and the control gains are the shown in Table 4.1.

To reproduce a realistic scenario the reference consists in a smooth function which gradually increases from an initial value to a final constant desired speed,

$$\omega^*(t) = \left(\frac{1 - e^{-\alpha(t-T)}}{1 + e^{-\alpha(t-T)}} + 1 \right) \left(\frac{\omega_f^* - \omega_0^*}{2} \right) + \omega_0^*. \tag{4.30}$$

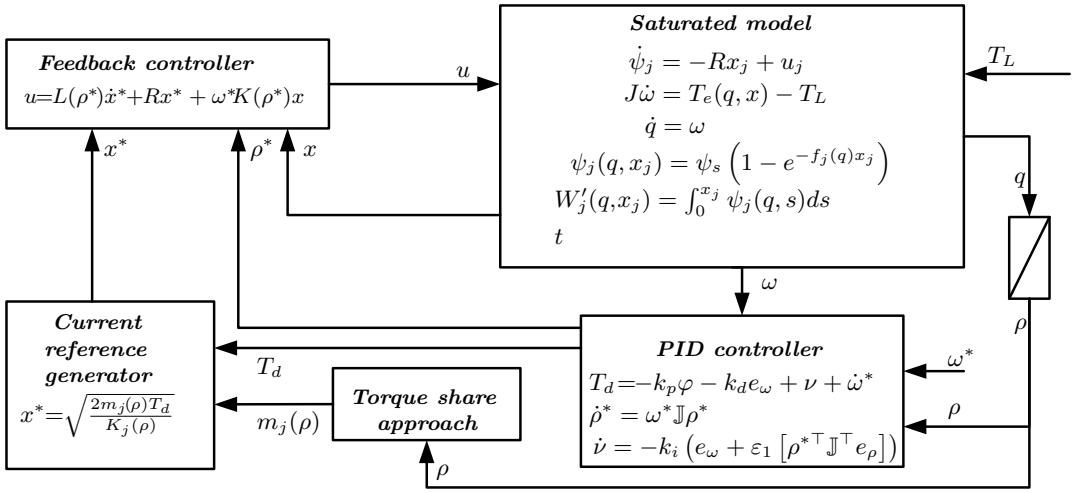

FIGURE 4.2: Diagram of simulation, note that the feedback controller is in ρ coordinates while the motor model is in q coordinates and it does consider linkage flux saturation -Model (3.2). Furthermore there is a coordinate transformation block which takes the position "measurement" q and returns ρ

Motor		**Control**	
$R = 2.5[\Omega]$	$\ell_0 = 52$[mH]	$k_p = 2000$	$k_i = 5e-4$
$\ell_1 = 20$[mH]	$N_r = 8$	$k_d = 25000$	$\varepsilon_1 = 0.1$
$J = 0.01kg - m^2$	$T_L = 0.1$[Nm]	$\rho_0^* = 20$	$K_{px} = 150$
$\beta = 2$	$\psi_s = 0.25$		

TABLE 4.1: Parameters of the motor and gains of the PID+Feedback controller.

We use $\omega_0 = 10$ and a final value of 50[rad/s].

The functions m_j, which are illustrated in Figure 4.3, are constructed as follows. First, we define q as a function of ρ *i.e.*

$$q(\rho) = \begin{cases} \varsigma(\rho) & \text{if } \rho_2 > \rho_1 > 0 \\ \varsigma(\rho) + \frac{\pi}{4} & \text{if } \rho_1 > \rho_2 > 0 \text{ or } \rho_1 > 0 > \rho_2 \\ \varsigma(\rho) + \frac{\pi}{8} & \text{if } \rho_1 < 0 \end{cases} \tag{4.31}$$

where $\varsigma(\rho) = \dfrac{tg^{-1}\left(\rho_2/\rho_1\right) - 2\pi/N_r}{N_r}$. Then, $q \in [0, 2\pi/N_r]$ is used in the construction of the auxiliary functions $\tilde{m}_j^+(\cdot)$ and $\tilde{m}_j^-(\cdot)$,

$$\tilde{m}_j^+(q) = \begin{cases} f(q_j) & \text{if } 0 < q_j \leq \frac{\pi}{3N_r} \\ 1 & \text{if } \frac{\pi}{3N_r} < q_j \leq \frac{2\pi}{3N_r} \\ 1 - f(q_j - 2\pi/N_r) & \text{if } \frac{2\pi}{3N_r} < q_j \leq \frac{\pi}{N_r} \\ 0 & \text{otherwise} \end{cases}$$

and

$$\tilde{m}_j^-(q) = \begin{cases} f(q_j - \frac{\pi}{N_r}) & \text{if } \frac{\pi}{N_r} < q_j \leq \frac{4\pi}{3N_r} \\ 1 & \text{if } \frac{4\pi}{3N_r} < q_j \leq \frac{5\pi}{3N_r} \\ 1 - f(q_j - 5\pi/3N_r) & \text{if } \frac{5\pi}{3N_r} < q_j \\ 0 & \text{otherwise} \end{cases}$$

with $q_1 = q$, $q_2 = q - {}^{2\pi}/_{3N_r}$, $q_3 = q + {}^{2\pi}/_{3N_r}$. Finally, $m_j(\rho)$ is obtained from

$$m_j(\rho) = \begin{cases} \tilde{m}_j^+(q(\rho)) & \text{if } T_d \geq 0 \\ \tilde{m}_j^-(q(\rho)) & \text{if } T_d < 0 \end{cases} \tag{4.32}$$

–notice, from Figure 4.3, that for each $j \in \{1, 2, 3\}$, $m_j^+(\rho) = \tilde{m}_j^+(q(\rho))$ is larger than zero only when $K_j(\rho) > 0$ and it equals zero when $K_j(\rho) < 0$. Similarly $m_j^-(\rho) = \tilde{m}_j^-(q(\rho))$ is larger than zero only when $K_j(\rho) < 0$, the latter guarantees that it is always possible to compute x^* as it is expressed in (4.7).

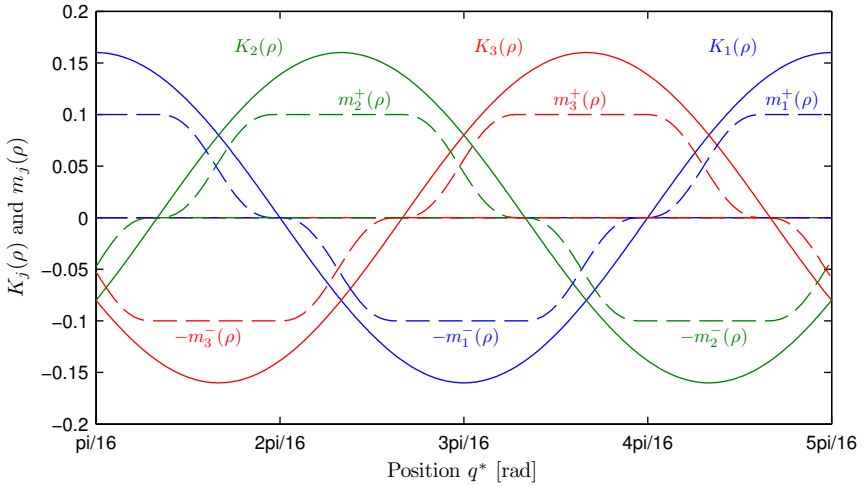

FIGURE 4.3: Construction of functions $m_j(\rho)$ for the simulation test of the *PID+Feedback* controller.

The overall behavior of the electrical currents during all the simulation time is depicted in Figure 4.4, notice that high currents, with magnitudes reaching 25[A], appear during the first half second, this behavior comes as resut of the more stressing condition imposed by the velocity reference profile -see the initial difference between $\omega(t)$ and $\omega^*(t)$ in Figure 4.8.

In Figure 4.5, the electrical currents are compared against the commutation functions m_j along trajectories and the reference currents on a zoomed window of time. Recall function m_j as defined in (4.32) corresponds to the above mentioned *torque sharing technique*.

The small mismatch between the currents and their references in Figure 4.5 may be reduced or eliminated by increasing the control gain k_{px}, note that in the simulation we have used $k_{px} = k_{px1} = 150$ –*cf.* Eq. (4.26).

However, in view of the good velocity tracking performance depicted in Figure 4.8, it is not worth to apply high gain at the stator level by imposing large values to the control gain k_{px}, at the expense of large control inputs.

The control input magnitude for the three phases are showed in Figure 4.6. Once again, notice the high magnitude of the input voltages reaching values of almost 500[V]. These values appears during the first half second, which accords with the electrical current results and have the same explanation.

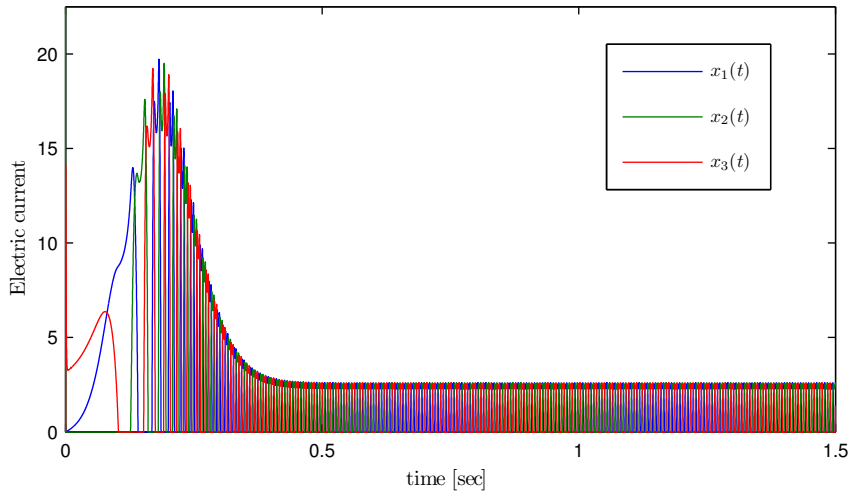

FIGURE 4.4: Three phases currents of the simulation test of the *PID+Feedback* controller..

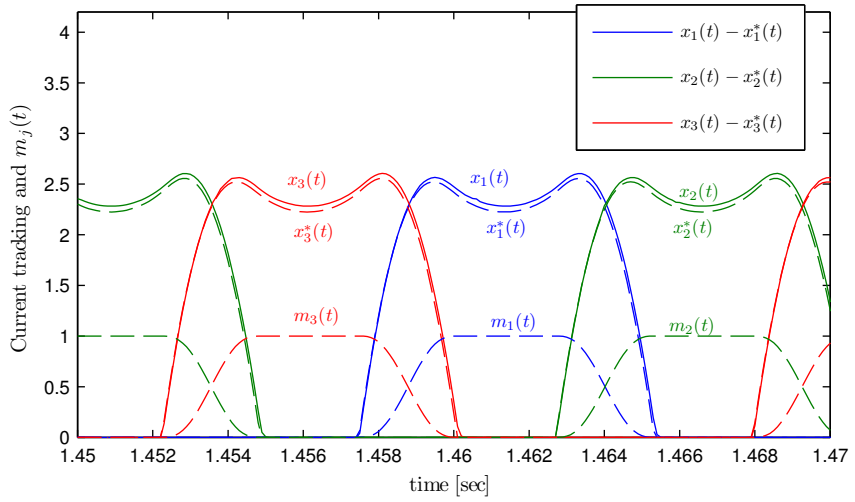

FIGURE 4.5: Zoom on the commutation functions and the three phases currents as well as their references.

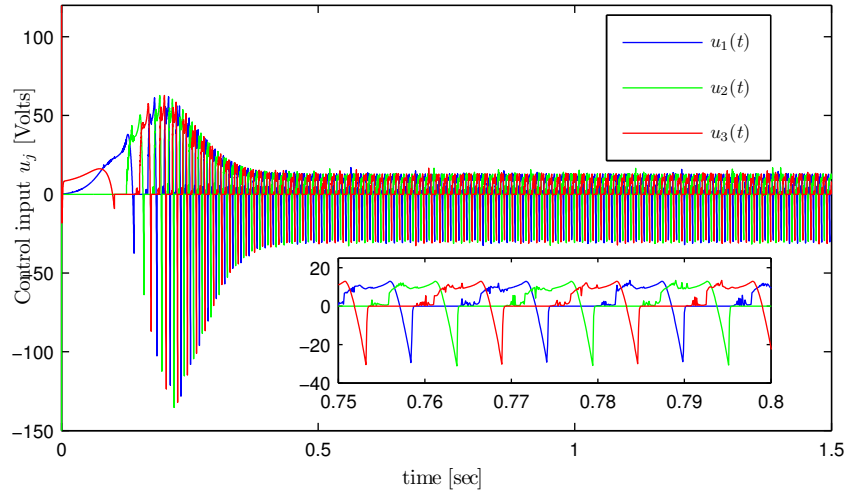

FIGURE 4.6: Voltage control inputs of the simulation test of the *PID+Feedback* controller.

In Figures 4.7 and 4.8 we show, respectively, the good position and velocity tracking performance. Note that in both cases the position $\rho(t)$ and the velocity $\omega(t)$ converge asymptotically toward

their respective references; that is, the rotor (4.4c) synchronizes with the virtual rotor (4.8) generated by the reference oscillator.

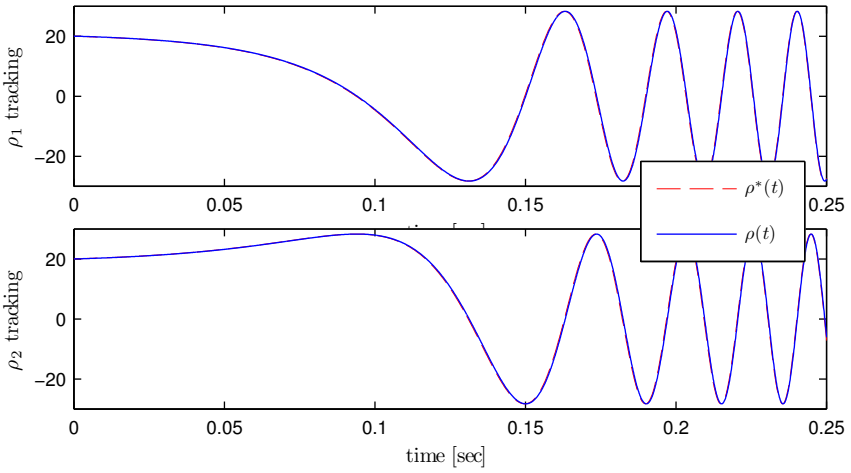

FIGURE 4.7: Tracking of mechanical position of the simulation test of the *PID+Feedback* controller.

Note as well that, while the signal reference $\omega^*(t)$ starts up at $\omega^*(0) = 10$[rad/sec], the switched-reluctance motor is started up from the standstill condition $\omega(0) = 0$. This condition stresses the controller and it is not used during real time applications. We just imposed this condition in simulation in order to show the performance of our controller under non-friendly conditions. As a result of this, we have in Figures 4.4 and 4.6 high values during the first half second.

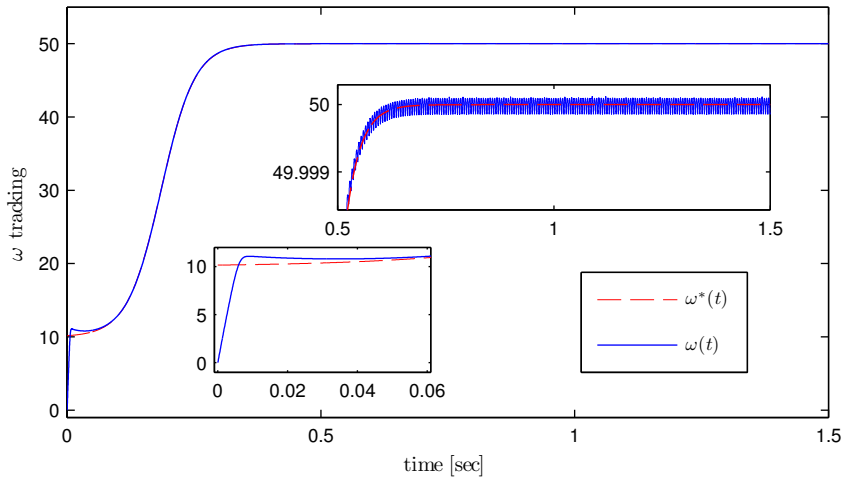

FIGURE 4.8: Tracking of mechanical velocity of the simulation test of the *PID+Feedback* controller.

4.7 Conclusions

In this chapter we have presented a control approach to the robust stabilization of the switched-reluctance motor. The control approach consists in stabilizing separately the stator and the rotor dynamics. We have established global exponential stability and input-to-state stability

with respect to external disturbances. Moreover, our control scheme has the special feature of being tailored to be implemented as a certainty-equivalence controller, with a state estimator. The design of the latter is under current research. Simulation results are encouraging to pursue this avenue towards the solution of full-sensorless control via certainty-equivalence control.

Chapter 5

Experimental Results

In this chapter we present the results of experimental tests that were run with the aim of evaluating the behavior and performance of the controllers described in the previous Chapters.

5.1 Description of the benchmark

A detailed description of the benchmark goes beyond the objective of this document (interested reader is invited to find further details about in [61]). However, a brief description is necessary to familiarize with the performed tests. The following picture present the utilized benchmark

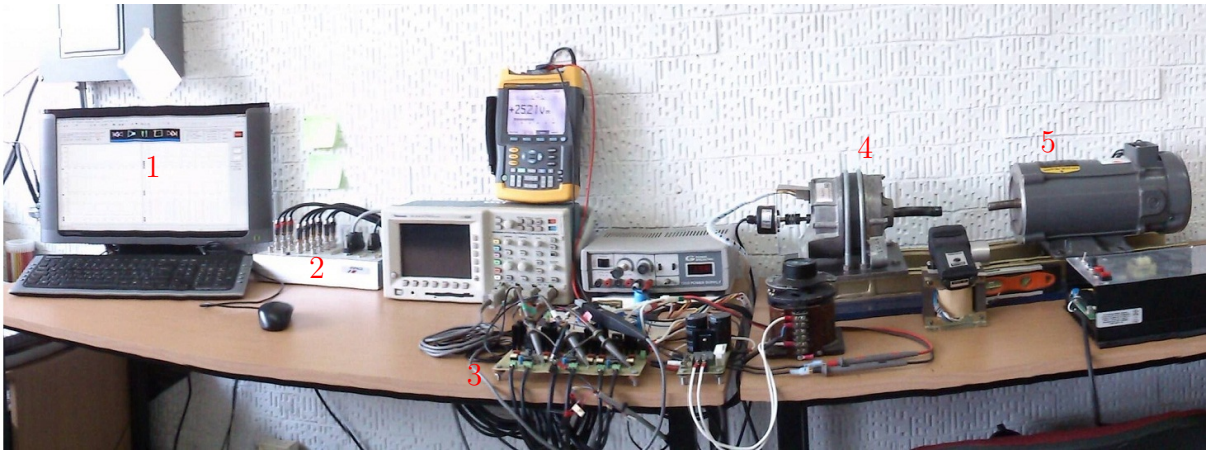

FIGURE 5.1: Benchmark at the Control Laboratory of the Postgraduate Building at UNAM.

As it may appreciated in Figure 5.1 the labeled elements of the benchmark are as follows:

1. A personal computer where the SIMULINK™ and CONTROLDESK™ software are installed. SIMULINK™ is used to directly program the control algorithms, that is the controllers presented in Chapters 3 and 4. CONTROLDESK™ serves to manipulate the control parameters and to process the information obtained during the experiments.

2. A *DSpace* data acquisition and processing card, model DS1104, which is used to implement the controller as well as a communication device model CP1104, also of DSpace, acting as interconnecting device between the data acquisition card and the power electronic device. The sampling time during the tests was set to $t_s = 1\text{x}10^{-4}$.

3. A Half-Bridge Asymmetric Converter (HBAC) which is in charge of translating the control signal, coming from the connecting device, to a train of square pulses in order to feed the switched-reluctance motor. This is performed by using the well known *Pulse Width Modulation* techniques. The HBAC is fed by a direct-current voltage-bus of 120[V].

4. The three phases, twelve stator-poles and eight rotor-poles switched-reluctance motor manufactured by *Emerson Electric Co.* The nominal values are

   Voltage: 120[V] Current: 2.5[A] Power: 250[W]

   and the physical parameters are the aligned inductance $\ell_0 = 30$[mH], the unaligned inductance: $\ell_0 = 24$[mH], the electric resistance: $R = 2.5[\Omega]$ and the rotor inertia J unknown.

5. A direct current motor running in open loop and mechanically coupled to the switched-reluctance motor. This DC motor is fed in such way that it acts as a constant load torque during the experiments.

5.2 Description of the experiments

In previous chapters we presented the design and numerical tests of different controllers for the switched-reluctance motor , these are:

1. PI^2D + *Feedback control* with **known parameters** and **unknown** mechanical velocity (sections 3.5.1 and 3.5.2)

2. PI^2D + *Adaptive feedback control* where in addition to velocity unavailability, **physical parameters are as well assumed unknown** and they are estimated estimated online (sections 3.5.1 and 3.5.3).

3. PID + *Feedback control* for the ρ-model where both **physical parameters and the whole state are assumed known** (sections 4.3 and 4.4).

For each one of controllers listed above, we have imposed three different velocity-reference profiles.

1. *Smooth-steps reference:* Constructed by using an hyperbolic-tangent type function

$$\omega^*(t) := \sum_{i=1}^{4} \omega_{0i} + \frac{1}{2}\left(\omega_{fi} - \omega_{0i}\right) \frac{1 - \exp^{-5(t-T_i)}}{1 + \exp^{-5(t-T_i)}} \tag{5.1}$$

   where

$$\begin{array}{llll} \omega_{01}=0, & \omega_{02}=0, & \omega_{03}=0, & \omega_{04}=0 \\ \omega_{f1}=110, & \omega_{f2}=-220, & \omega_{f3}=220, & \omega_{f4}=-110 \\ T_1=4, & T_2=16, & T_2=28, & T_2=40 \end{array}$$

2. *Saturated-ramp reference:* This reference is constructed by utilizing the following function

$$\omega^*(t) := \begin{cases} \frac{\omega_1}{t_1}t & 0 \le t \le t_1 \\ \omega_1 & t_1 \le t \le t_1 \\ \frac{\omega_2-\omega_1}{t_3-t_2}(t-t_2)+\omega_1 & t_2 \le t \le t_3 \\ \omega_2 & t_3 \le t \le t_4 \\ \frac{\omega_3-\omega_2}{t_5-t_4}(t-t_4)+\omega_2 & t_4 \le t \le t_5 \\ \omega_1 & t_5 \le t \le t_6 \\ \frac{-\omega_3}{t_7-t_6}(t-t_6)+\omega_3 & t_6 \le t \le t_7 \end{cases} \tag{5.2}$$

where

$$\begin{array}{lllllll} \omega_1=100, & \omega_2=-100 & \omega_3=100 & & & & \\ t_1=2.5 & t_2=12.5 & t_3=17.5 & t_4=27.5 & t_5=32.5 & t_6=42.5 & t_7=45 \end{array}$$

3. *Sinusoidal reference:* The easiest reference signal to construct, where we have chosen a suitable amplitude and frequency, *i.e.,*

$$\omega^*(t) = 100\sin(0.45t) \tag{5.3}$$

Consequently, we present the result of nine different experiments (three velocity profiles for each one of the three designed controllers). The load torque imposed by the coupled DC motor remains piece-wise constant and unknown during all the experiments.

5.3 Tests to the PI^2D+*Feedback* controller

In this section we present the result of the experiments performed in order to evaluate the PI^2D+ Feedback controller

$$PI^2D \begin{cases} T_d &= -k_p e_q - k_d \vartheta + \nu + \dot{\omega}^* \\ \dot{\nu} &= -k_i(e_q - \vartheta) \\ \dot{q}_c &= -a(q_c + be_q) \\ \vartheta &= q_c + be_q \end{cases}$$

$$\begin{array}{rl} \text{Feedback} \\ \text{controller} \end{array} \begin{cases} u &= L(q)\alpha\rho + \omega^* K(q)x + Rx^* - k_{px}e_x \\ e_x &= x - x^* \end{cases}$$

presented in Sections 3.5.1 and 3.5.3 respectively. The control gains are in the table below.

PI2D		Feedback
$k_p = 2000$	$k_i = 5\text{e}^{-4}$	$k_{px} = 24$
$k_d = 15000$	$a = 750$	$\eta = 6.4\text{e}^{-4}$
$b = 1600$	$\varepsilon = 1\text{e}^{-2}$	

TABLE 5.1: Control gains for the experiments corresponding to the PI^2D+*Feedback* controller.

5.3.1 Smooth-steps velocity reference

This reference signal is constructed by implementing Equation (5.1), it starts at $\omega^*(0) = 0$ and increases smoothly up to $\omega^*(t) = 110$[rad/s] at $t = 5.5s$, where it remains during around 10 seconds. Then, it gradually decreases until it shifts the spin sense and reaches -110[rad/s].

The test corresponds to the most favorable scenario, we imposed this velocity reference and the results in tracking are shown in Figure 5.2. We notice a good behavior with only a small delay in both upper-zoomed plots.

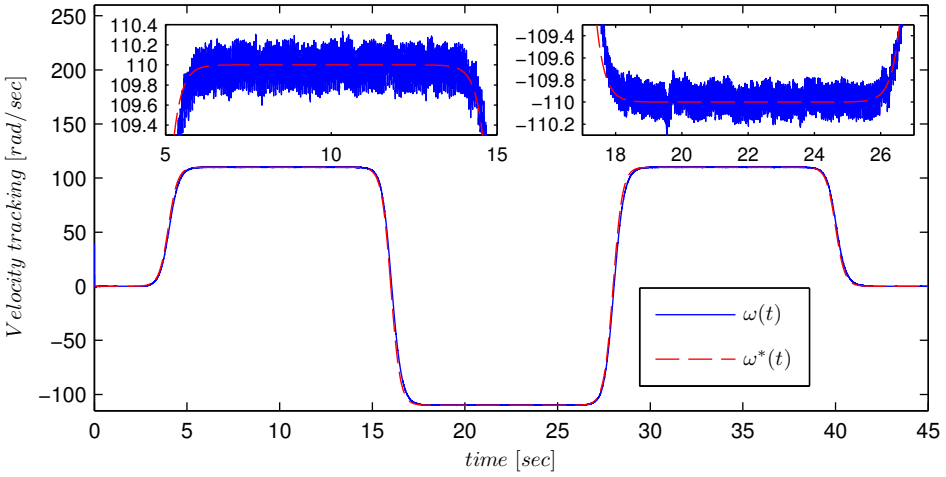

FIGURE 5.2: Velocity tracking of the smooth step reference for the PI^2D+ Feedback controller.

Furthermore, the results on tracking of the desired current reference is illustrated in Figure 5.3, we show the overall behavior of the controller during the whole experiment on left-side plots. On the right hand side plots of the figure, we show the tracking performance with more detail during a narrow time-window. The performance is good enough when we take into account that the objective of control is the mechanical velocity.

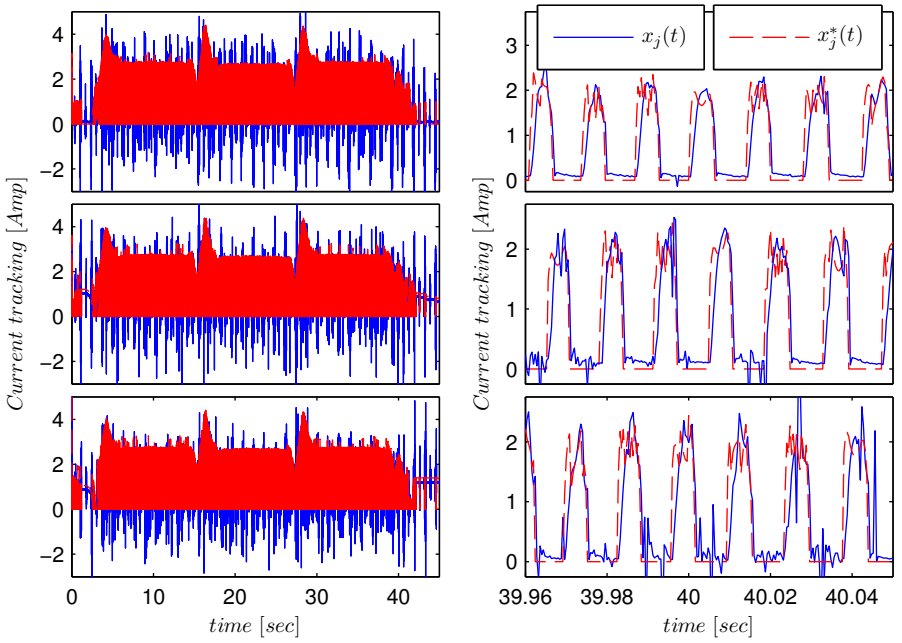

FIGURE 5.3: Current tracking corresponding to the smooth step reference for the PI^2D+ Feedback controller.

The last figure of this scenario corresponds to the signal control input, shown in Figure 5.4, this signal is entered to the half bridge asymmetric converter; which, based on the pulse width modulation methods, feeds the switched-reluctance motor.

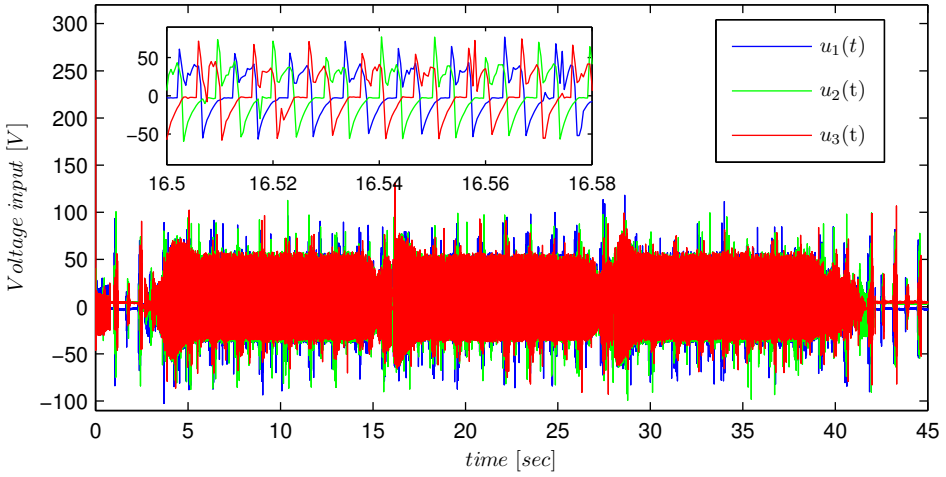

FIGURE 5.4: Voltage control input corresponding to the smooth step reference for the PI^2D + Feedback controller.

5.3.2 Saturated-ramp velocity reference

Next, we tested the performance of the PI^2D+Feedback controller, with the *saturated-ramp velocity reference*, constructed by applying Equation (5.2).

The result of velocity tracking is shown in Figure 5.5, where a good response in tracking is appreciated and only a small delay appears on the two zoomed plots.

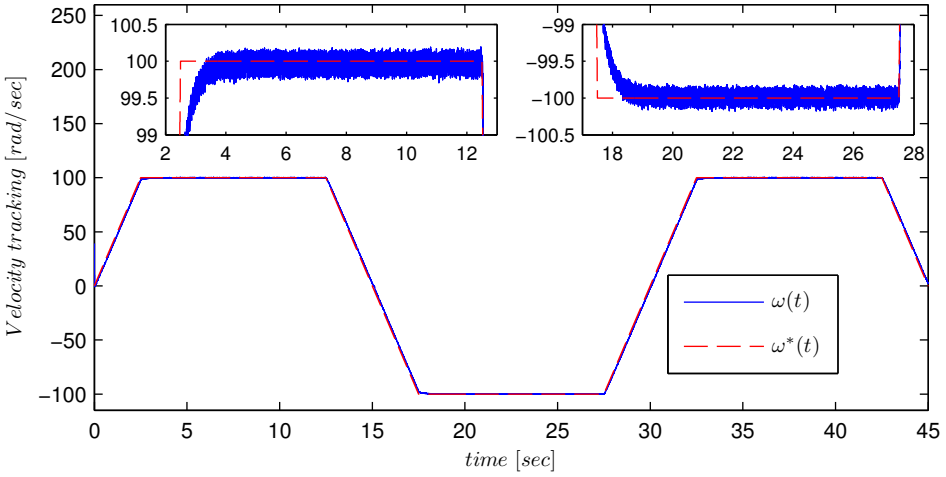

FIGURE 5.5: Velocity tracking of the saturated ramp reference for the PI^2D+ Feedback controller.

The tracking of the desired electric current for this scenario is shown in Figure 5.6. Notice on the right hand side plots a better response compared to that presented in the previous scenario. However, a small delay with respect to its reference can be noticed.

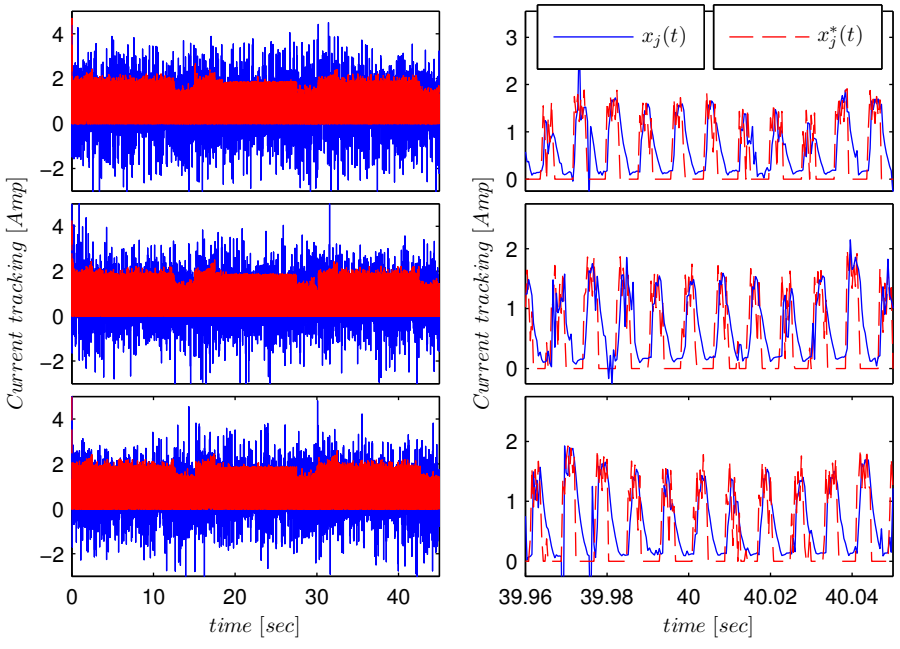

FIGURE 5.6: Current tracking of the saturated ramp reference for the PI^2D+ Feedback controller.

Finally, the control input is shown in Figure 5.7, note that the magnitude of this signal seldom exceeds ±100[V] and it is around ±50[V] during the most of the time, which is convenient for the half-bridge asymmetric converter.

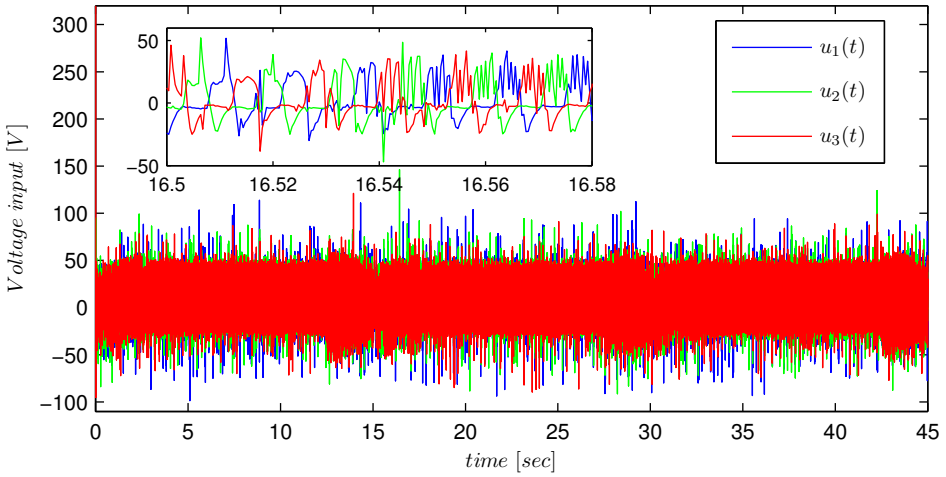

FIGURE 5.7: Voltage control input corresponding to the saturated ramp reference for the PI^2D+ Feedback controller.

5.3.3 Sinusoidal velocity reference

The last velocity-reference profile imposed to this controller corresponds to a sinusoidal signal -see Equation (5.3), this sinusoidal function has an amplitude of 100[V] and a period of 14s.

In Figure 5.8 we show the obtained results for velocity tracking. Similarly to the last scenario, a small delay is present, yet a good response of the motor is achieved and the control objective is attained.

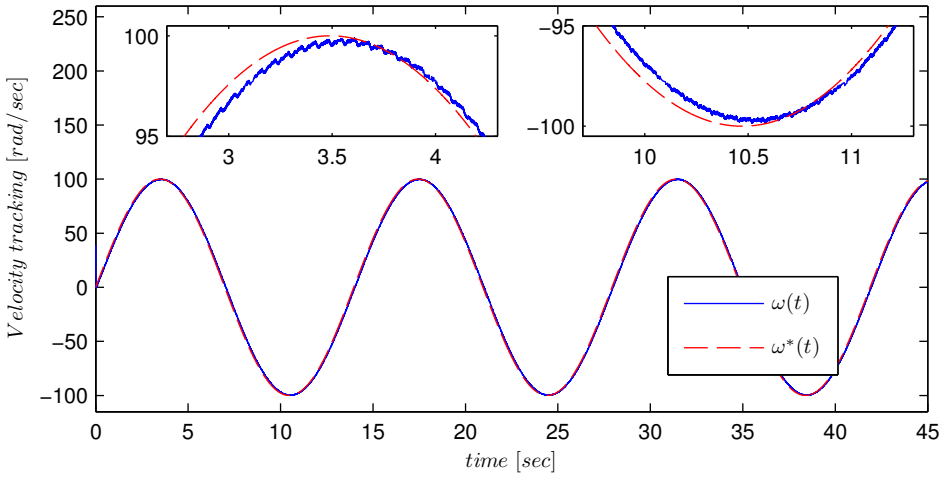

FIGURE 5.8: Velocity tracking of the sinusoidal reference for the PI^2D+ Feedback controller.

In Figure 5.9 we show the current reference tracking performance. Note that even when there are small errors in the tracking, it is better than the results presented in the previous scenarios.

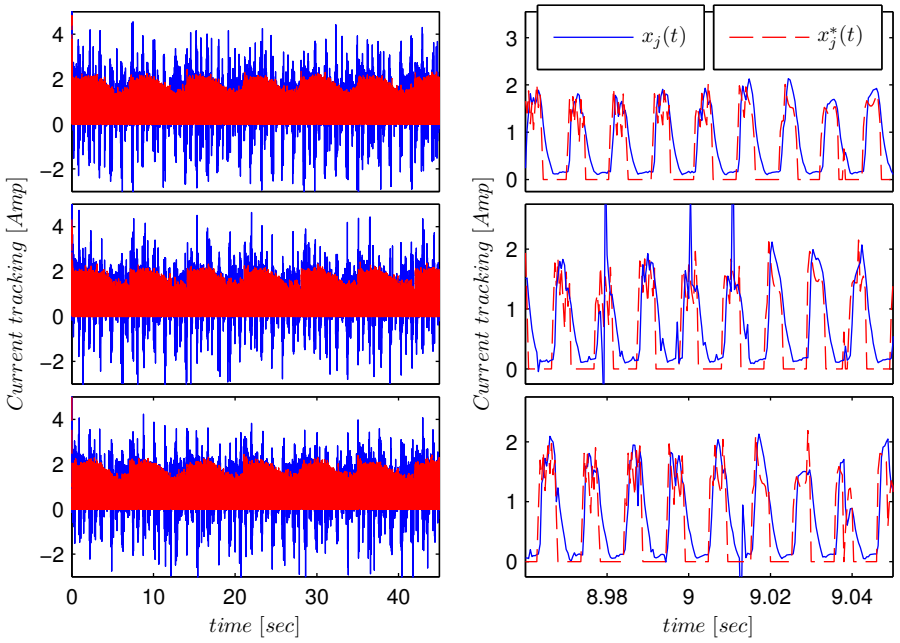

FIGURE 5.9: Current tracking corresponding to the sinusoidal reference for the PI^2D+ Feedback controller.

Finally, in Figure 5.10, we present the control input generated by the controller, we note that the demanded voltage magnitude is not high, around $\pm 50V$, which is fed without problem by the converter.

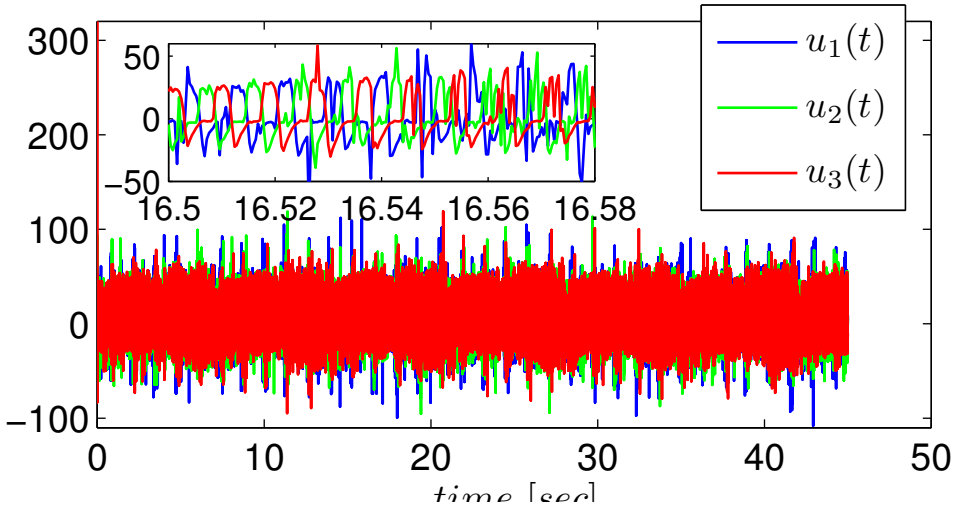

FIGURE 5.10: Voltage control input corresponding to the sinusoidal reference for the PI^2D + Feedback controller.

In this section we have presented the obtained results of the tests performed to the PI^2D+ feedback control considering three different scenarios, these are the *smooth step*, the *saturated ramp* and the *sinusoidal* reference. We obtained good results in tracking velocity in the all of

the three scenarios, with only small delays, however these are not significant for the control goal achievement. The current reference tracking is also good enough and in all cases reference and real current are in phase with a small difference in amplitude. Finally, we get low level voltages in the control signal, which is suitable for the half-bridge asymmetric converter. The designed controller achieves almost with no problems the control objectives.

5.4 Tests to the PI^2D+*Adaptive feedback* controller

Now we present the results corresponding to the performed experimental tests considering the PI^2D+*Adaptive feedback controller*

$$PI^2D \begin{cases} T_d &= -k_p e_q - k_d \vartheta + \nu + \dot{\omega}^* \\ \dot{\nu} &= -k_i(e_q - \vartheta) \\ \dot{q}_c &= -a(q_c + be_q) \\ \vartheta &= q_c + be_q \end{cases}$$

$$\begin{array}{r} \textit{Adaptive}\text{-Feedback} \\ \text{controller} \end{array} \begin{cases} \hat{u} &= \Psi(t, y, e_x)\hat{\Theta} - k_{px}e_x \\ \dot{\hat{\Theta}} &= -k_\theta \Psi^\top(t, y, e_x)e_x \end{cases}$$

presented in section 3.5.3. The control gains k_p, k_i, k_d, a and b utilized during the experiments are presented in Table 5.1, however, the gains k_θ for the adaptive law and the gains k_w for the anti-windup strategy are the following:

Adaptive law	**Anti windup**
$k_{\theta 1} = 3.2\text{e}^{-6}$	$k_{w1} = 0.7$
$k_{\theta 2} = 7.5\text{e}^{-6}$	$k_{w1} = 1.5$
$k_{\theta 3} = 1.6\text{e}^{-3}$	$k_{w1} = 7$

TABLE 5.2: Control gains for the adaptive law and the anti windup technique.

5.4.1 Anti-windup strategy

The adaptation law $\dot{\hat{\Theta}} = -k_\theta \Psi^\top(t, y, e_x)e_x$ essentially consists in the integral of two multiplied terms. The first, $\Psi(t, e_x, y)$, is bounded and persistently exciting[1] at $y = 0$ and $e_x = 0$ whilst the second term, e_x, corresponds to the state of the controlled system. Given the boundedness and the persistency-of-excitation property of $\Psi(\cdot)$, a necessary condition for $\tilde{\Theta}$ to converge to zero is that e_x vanishes, that is $e_x \to 0$ as $t \to \infty$. Theoretically speaking, the last comes from the uniform global exponential stability property of $e_x = 0$. Nonetheless, x^* is a complicated function of the state trajectories which oscillates between zero and positive values. That is, it is a highly changing function difficult to follow, this condition generates a persistent error in its

[1] This property is shown in section 3.6.1.

tracking, just when $x(t)$ is almost reaching its reference, $x^*(t)$ abruptly changes giving a "new" reference to follow, this provokes $e_x(t)$ to slightly grow just before it again tends to zero. The latter phenomenon is repeated all long of the experiment. Consequently, $\tilde{\Theta}$, which comes from the integral of a non-vanishing term e_x, grows indefinitely. To avoid this, an anti-windup strategy was implemented, this technique allows us to restart the integral term once it has reached a given threshold. The anti-windup technique consists in adding saturation term to (3.28b)

$$\dot{\hat{\Theta}} = -k_\theta \Psi^\top(\cdot) e_x + k_w \left[\hat{\Theta}_s - \hat{\Theta}\right]$$

where $\hat{\Theta}_s = \left[sat(\hat{\Theta}_1) \quad sat(\hat{\Theta}_2) \quad sat(\hat{\Theta}_3)\right]^\top$, $\Theta_1 = \ell_0$, $\Theta_2 = \ell_1$, and $\Theta_3 = R$. The gains k_θ and k_w are set in Table 5.2.

5.4.2 Smooth-steps velocity reference

In order to investigate the response of the adaptive controller to a smooth reference signal, we impose the profile given by Equation (5.1). The obtained result of velocity tracking is plotted in Figure 5.11. Note the good response of the controller with only small oscillations around the desired velocity, moreover there are not delays in the tracking. It is also notorious that there is not an important difference between these results and those for the non-adaptive controller presented in Section 5.3.1.

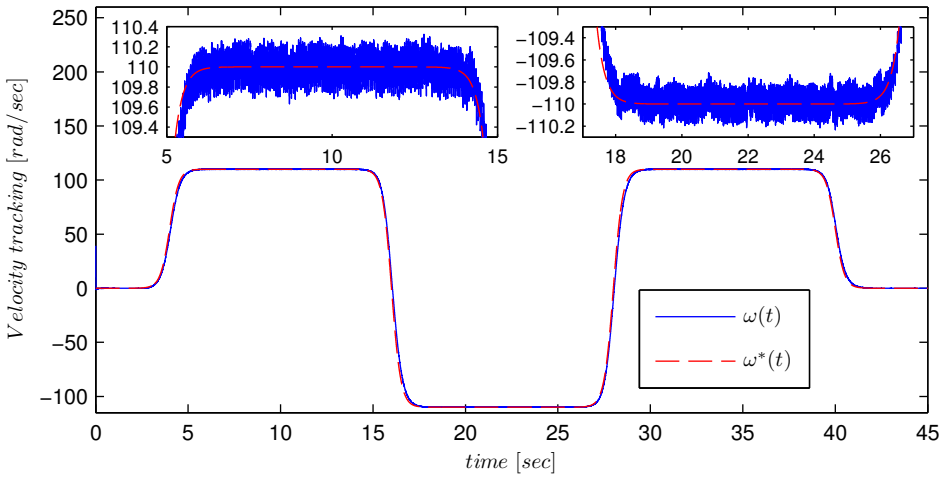

FIGURE 5.11: Velocity tracking of the smooth step reference for the PI^2D+ Adaptive feedback controller.

The result of the experiment concerning the current tracking is shown in Figure 5.12. Note, from the plots on the left, that the currents rarely exceed 3[A], they are higher only when motor is speeding up. From the plots on the right it can be noticed that the electric current is below 2.5[A] and tracking errors are quite acceptable.

The control input produced by the controller under test is depicted in Figure 5.13. This result is similar to that presented in the previous scenarios, magnitude of voltage around ±55[V] is

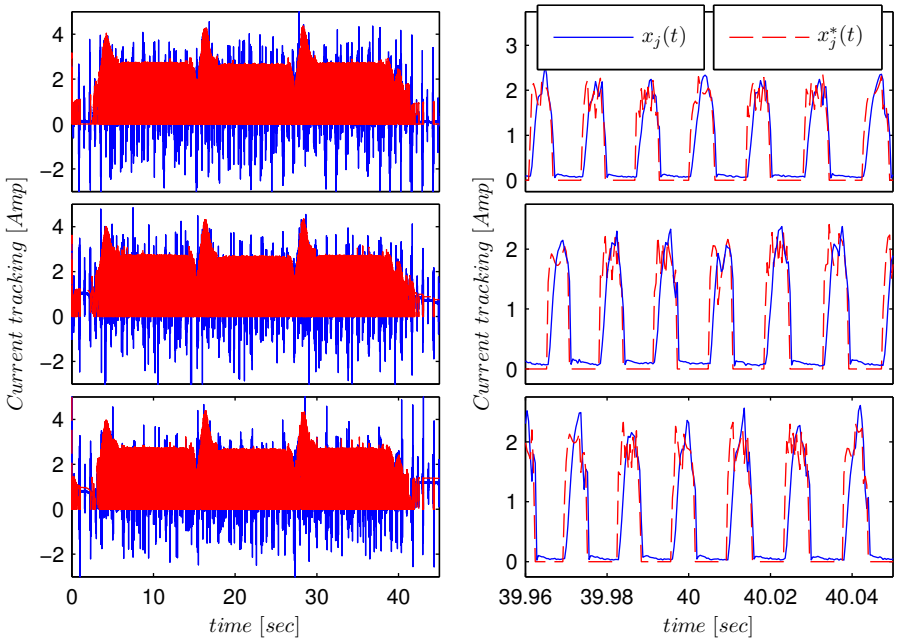

FIGURE 5.12: Current tracking corresponding to the smooth step reference for the PI^2D+Adaptive feedback controller.

proper for the half-bridge asymmetric converter, which will not be strained in excess under this regime.

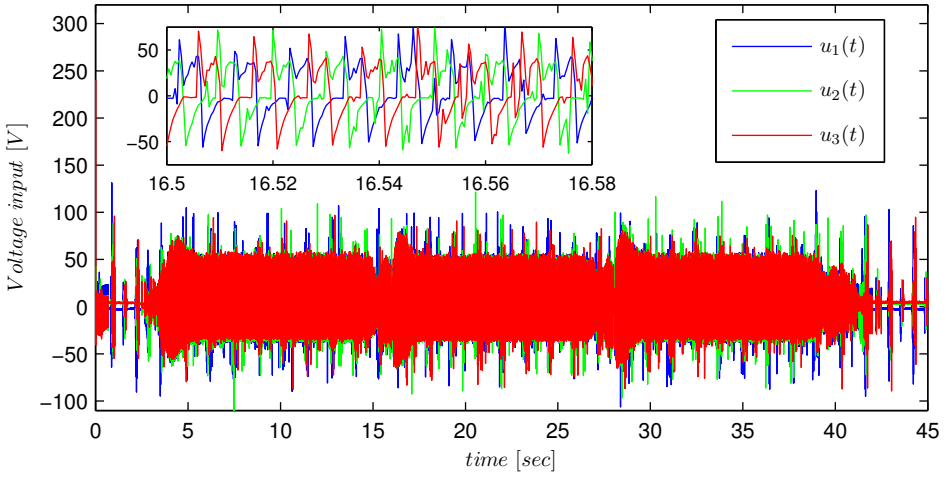

FIGURE 5.13: Voltage control input corresponding to the smooth step reference for the PI^2D + Adaptive feedback controller.

Finally for this scenario, we show, in Figure 5.14, the result of estimation of the physical parameters ℓ_0, ℓ_1 and R. It is important to note that the estimations of parameters do not converge to the real values, they are oscillating around them as result of the effect of the anti-windup strategy.

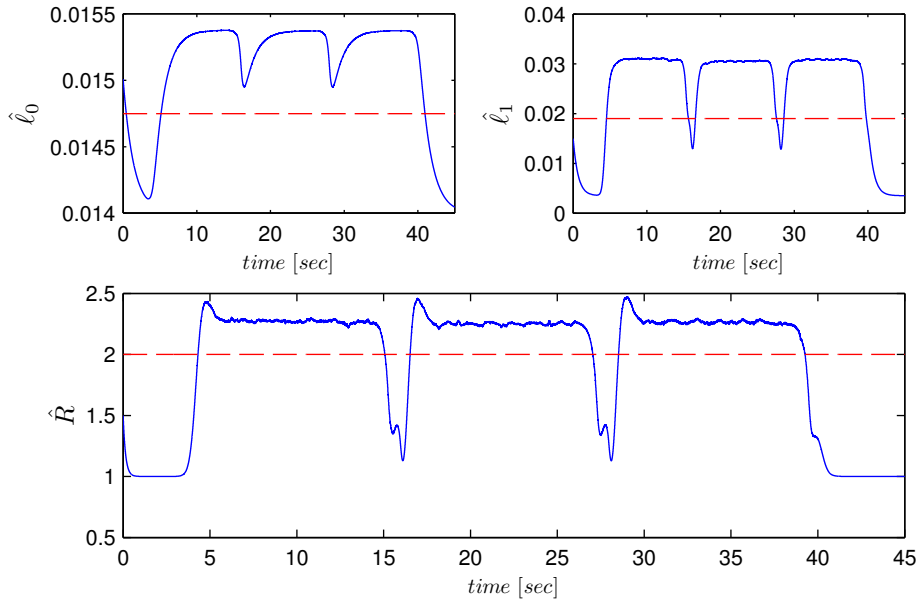

FIGURE 5.14: Estimation of parameters ℓ_0, ℓ_1 and R for the smooth-step reference.

5.4.3 Saturated-ramp velocity reference

In another experiment we injected a saturated ramp reference, constructed by implementing the function in (5.2). Note the good overall response of the velocity tracking in Figure 5.15, it only appears a small delays, see zoomed plot on the same figure, just after velocity stabilizes at 100[rad/s] and −100[rad/s], however this delay does not impact on the overall behavior.

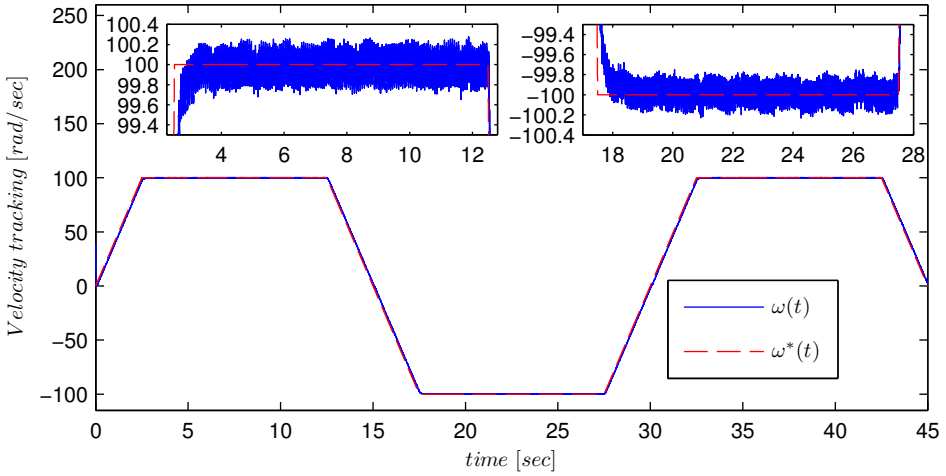

FIGURE 5.15: Velocity tracking of the saturated ramp reference for the PI^2D+Adaptive feedbackcontroller.

The tracking of the desired electric current for this scenario is shown in Figure 5.16, note in the right side plots that the actual current does not reach its reference in magnitude.

The control input is depicted in Figure 5.17, it is possible to note well behaved control signal and in the zoomed plot not too high voltage signals are shown, which can be easily handed by

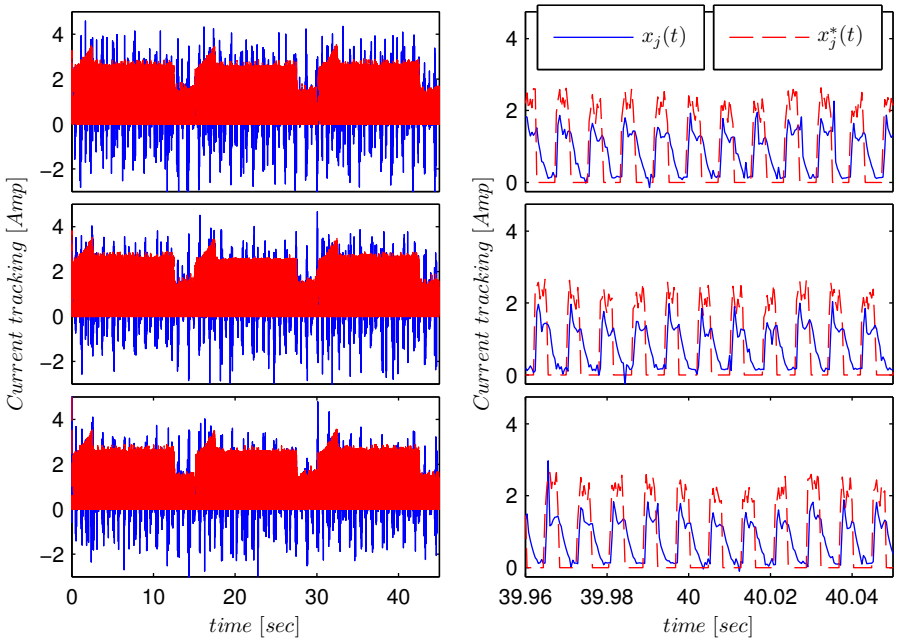

FIGURE 5.16: Current tracking corresponding saturated ramp reference for the PI^2D+ Adaptive feedback controller.

the half-bridge asymmetric converter.

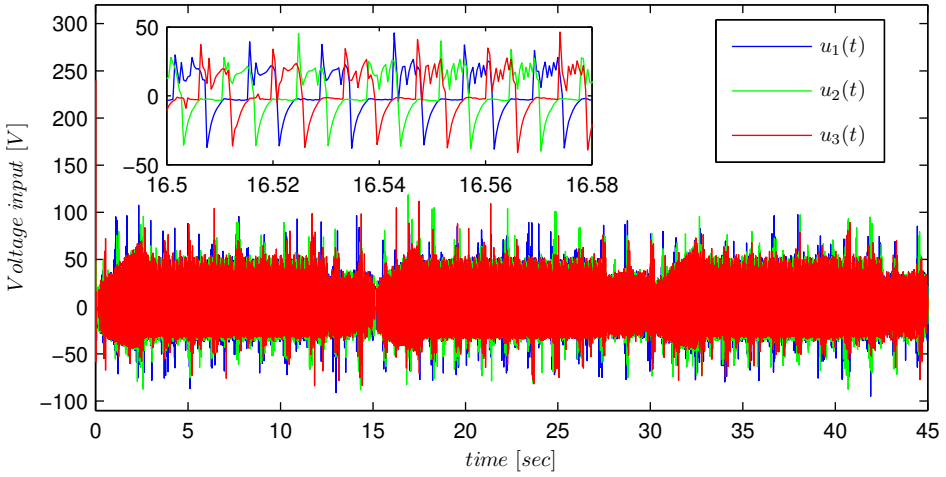

FIGURE 5.17: Voltage control input corresponding to the saturated ramp reference for the PI^2D + Adaptive feedback controller.

Finally, the results concerning to the estimation of the physical parameters are presented in Figure 5.18. As it may be observed in this figure, the estimate oscillates around the mean value which correspond to that of the real parameter.

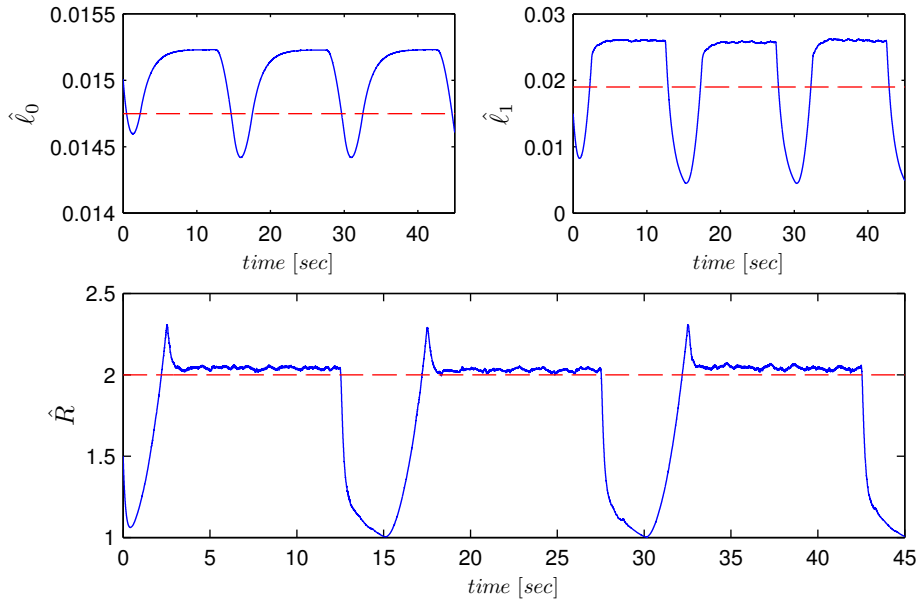

FIGURE 5.18: Estimate of electric parameters ℓ_0, ℓ_1 and R for the saturated ramp reference.

5.4.4 Sinusoidal velocity reference

In this section we present the results of the experiments where a sinusoidal velocity reference was imposed.

The corresponding result of velocity tracking is depicted in Figure 5.19. This scenario requires the motor to constantly shift the sense of spin. The velocity tracking performance is not as good as in the previous cases and small delays may be observed on zoomed plots. Nevertheless, a good overall behavior is obtained. The tracking of the desired electric current is shown in Figure 5.20.

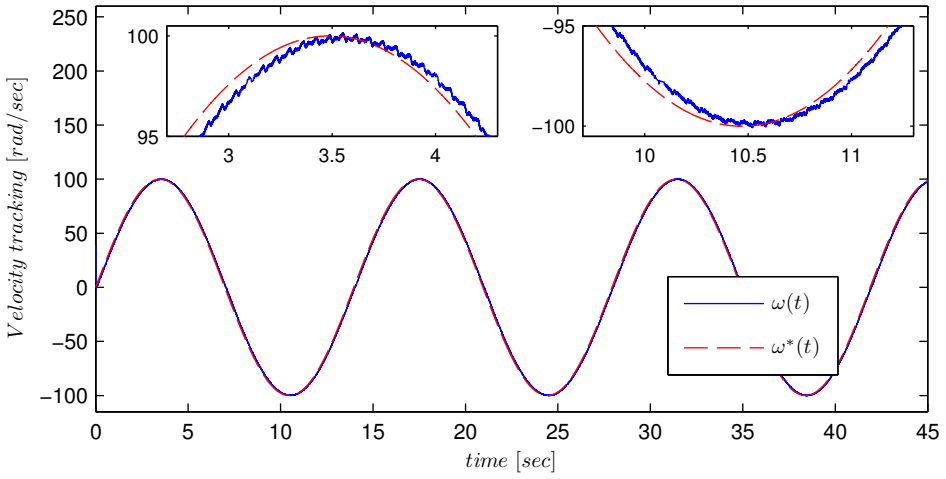

FIGURE 5.19: Velocity tracking of the sinusoidal reference for the PI^2D+ Adaptive feedback controller.

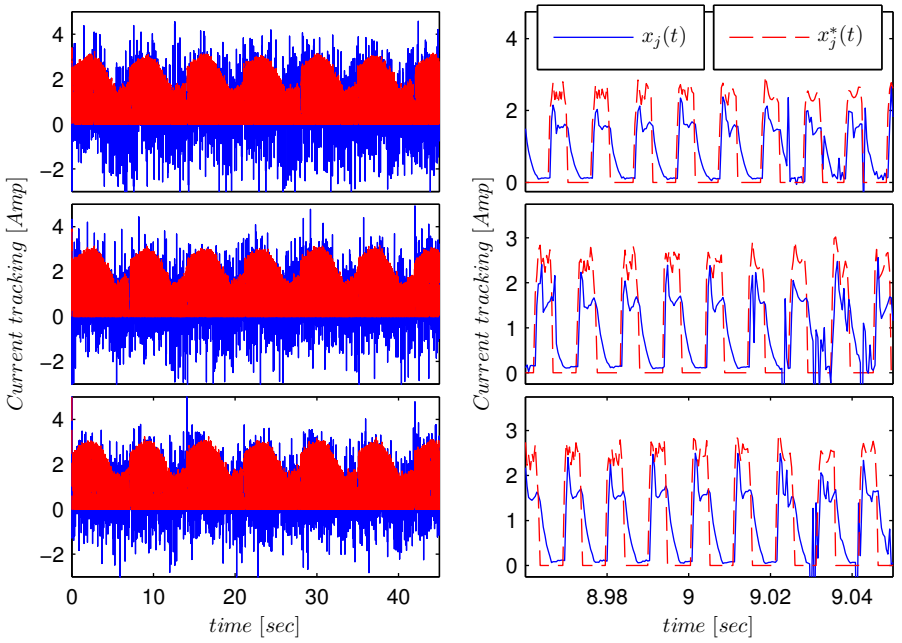

FIGURE 5.20: Current tracking corresponding to the sinusoidal reference for the PI^2D+Adaptive feedback controller.

In Figure 5.21 the control signal is shown and, similarly to the previous scenarios, its magnitude is not too high which allows the converter to handle them with no problems and feed the motor.

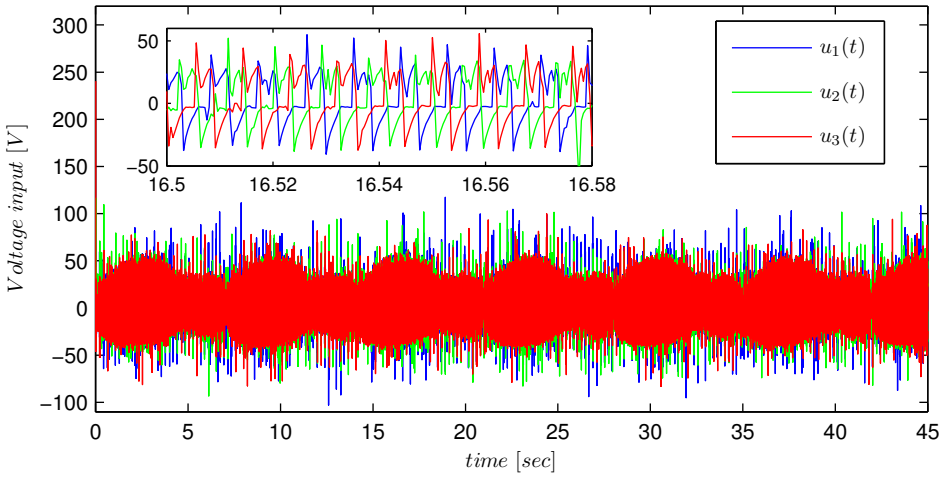

FIGURE 5.21: Voltage control input corresponding to the sinusoidal reference for the PI^2D + Adaptive feedback controller.

The estimations of the physical parameters are shown in Figure 5.22, note the oscillating behavior around the real values, which are consistent with the imposed velocity reference.

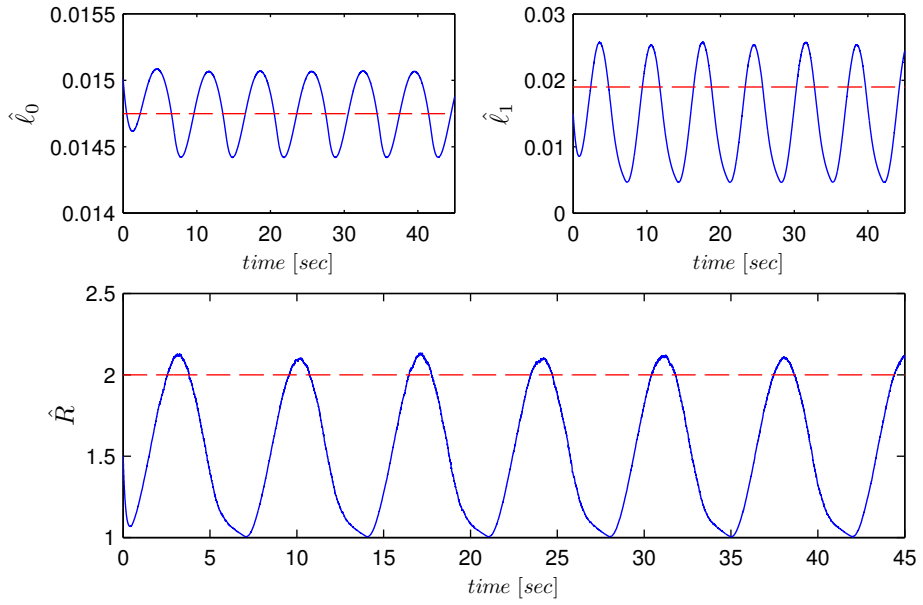

FIGURE 5.22: Estimate of electric parameters ℓ_0, ℓ_1 and R for sinusoidal reference.

5.5 Tests of the PID+*Feedback* controller for the ρ-model

We present now the results of the experiments corresponding to the PID+*feedback control*

$$\text{PID} \left\{ \begin{array}{rcl} T_d & = & -k_d e_\omega - k_p b^*(t)^\top e_\rho + \nu + \dot{\omega}^*. \\ \dot{\nu} & = & -k_i e_\omega - \varepsilon_1 k_i b^*(t)^\top e_\rho \end{array} \right.$$

$$\begin{array}{l} \text{Feedback} \\ \text{controller} \end{array} \left\{ \; u^*(t,x) := L(\rho^*)\dot{x}^* + K(\rho^*)\omega^* x + Rx^* - k_{px} e_x \right.$$

presented in Chapter 4. This controller is composed by equations; where, after a tuning process, the following control gains were utilized Similarly to the experiments reported in previous

PID		**Feedback**
$k_p = 40$	$k_i = 1\text{e}^{-8}$	$k_{px} = 24$
$k_d = 200$	$\rho_0^* = 4$	
$\varepsilon_1 = 1\text{e}^{-8}$		

TABLE 5.3: Control gains for the experimental test of the PID+*Feedback controller*.

sections, we have imposed three different velocity profiles $\omega^*(t)$; the corresponding results are presented in the following sections.

5.5.1 Smooth-steps velocity reference

The corresponding result of velocity tracking is depicted in Figure 5.23; as in the previous scenarios, a good performance may be observed. Note the small oscillations around $t = 23$[sec], this is due to a step-increment of unknown magnitude in the load torque imposed by the coupled direct motor. Despite this disturbance, the controller works properly and the motor velocity is again driven to its reference.

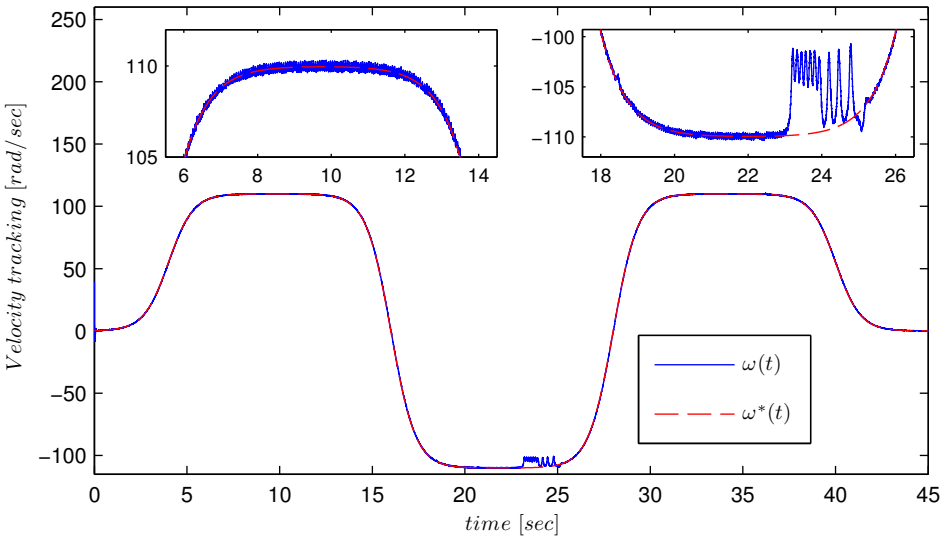

FIGURE 5.23: Velocity tracking of the smooth step reference for the $PID+$ Feedback controller.

The results for current tracking are shown in Figure 5.24. Note on left side plots the overshoots in current at $t = 23$[sec] as effect of the load torque increment. On the right hand side plots, a zoomed window shows the good results.

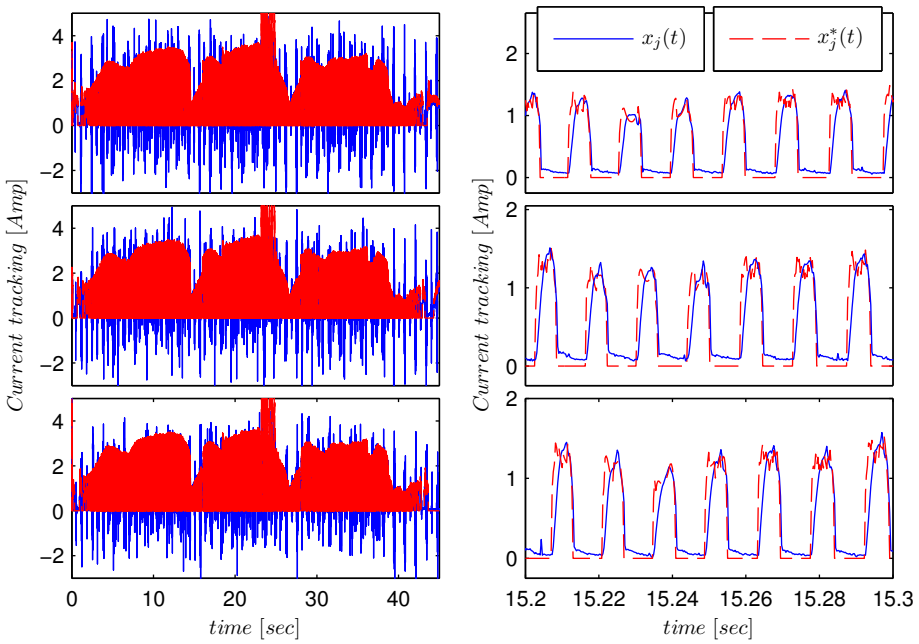

FIGURE 5.24: Current tracking corresponding to the smooth step reference for the $PID+$ Feedback controller.

Finally, voltage control input is depicted in Fig (5.25), in this figure it is noted the effect of the load torque increment, however magnitude seldom goes beyond ± 50[V], which is suitable for the half-bridge asymmetric converter.

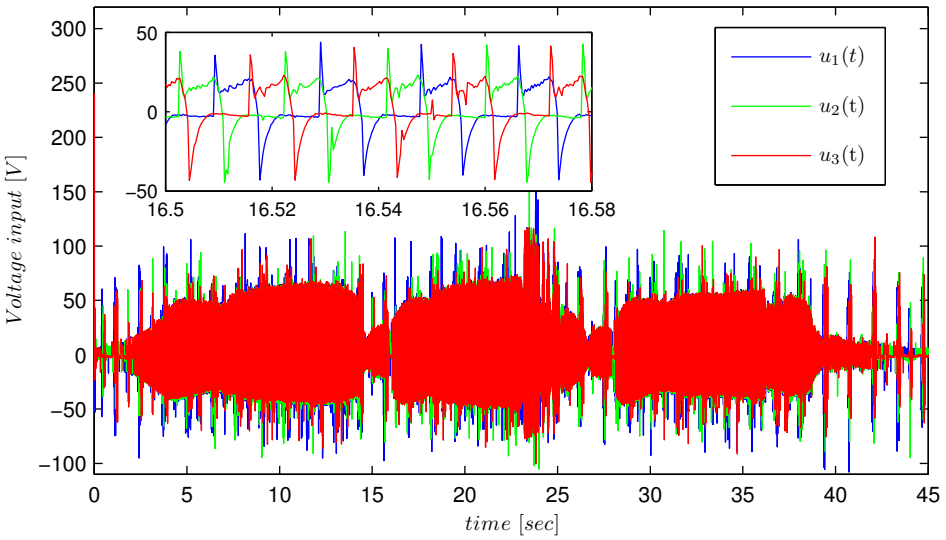

FIGURE 5.25: Voltage control input corresponding to the smooth step reference for the $PID+$ Feedback controller.

5.5.2 Saturated-ramp velocity reference

First, velocity tracking is depicted in Figure 5.26, note the good fit between the actual velocity and the imposed reference despite the small overshoot appreciated in the zoomed plots.

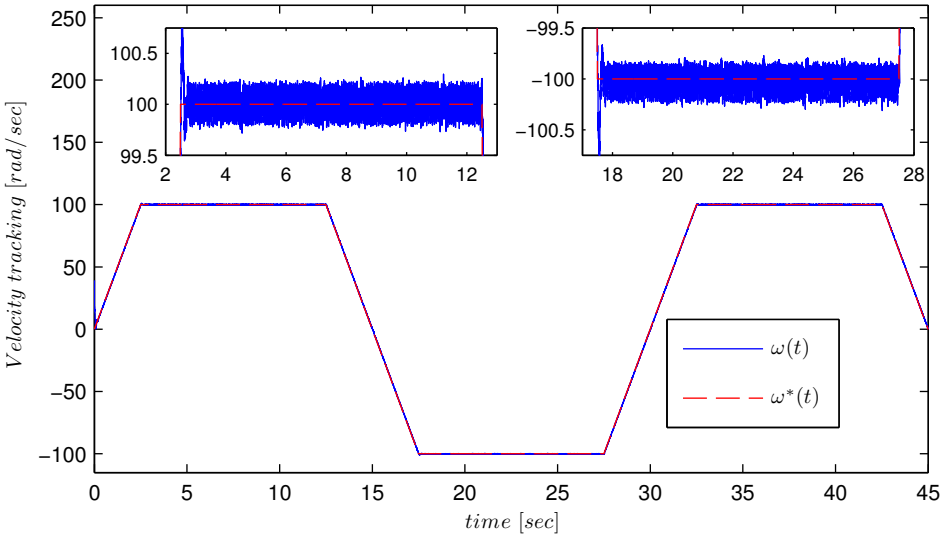

FIGURE 5.26: Velocity tracking of the saturated ramp reference for the $PID+$ Feedback controller.

Electrical current tracking is depicted in Figure 5.27 where currents not larger than 4[A] are shown but they are smaller that 2.5[A] the most of the time. Good tracking of current is shown on right hand side plots with a small error in magnitude, however this error does not impact on the velocity tracking.

Finally, for this scenario, the voltage input is shown in Figure 5.28, where values seldom overpass magnitudes of ± 60[V]. Moreover, note around $t = 15$[sec] and $t = 30$[sec], the way how the signals

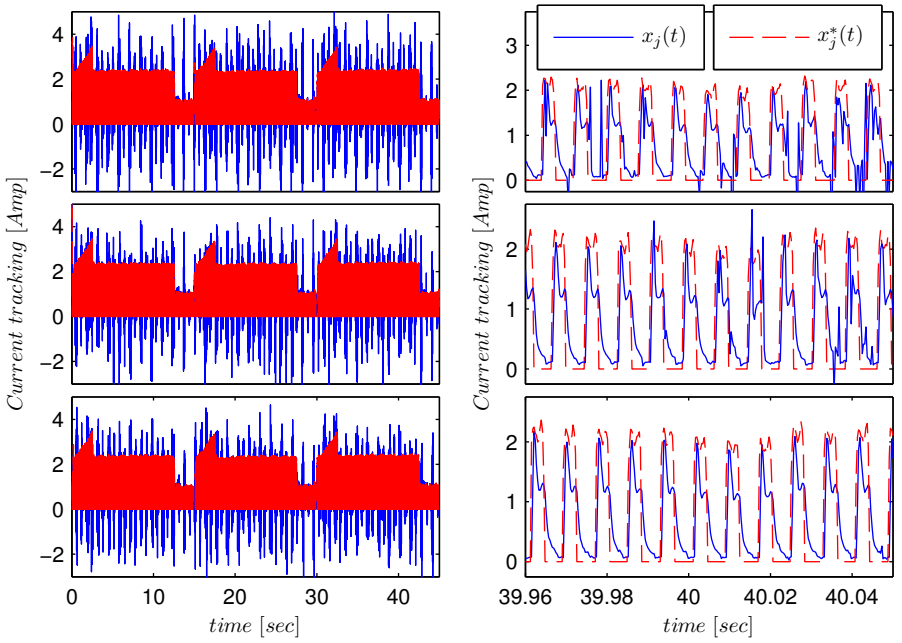

FIGURE 5.27: Current tracking corresponding to the saturated ramp reference for the *PID+* Feedback controller.

voltage control must shift sequence of phases in order to achieve the spin sense shift, -see on Figure 5.26 the velocity profile.

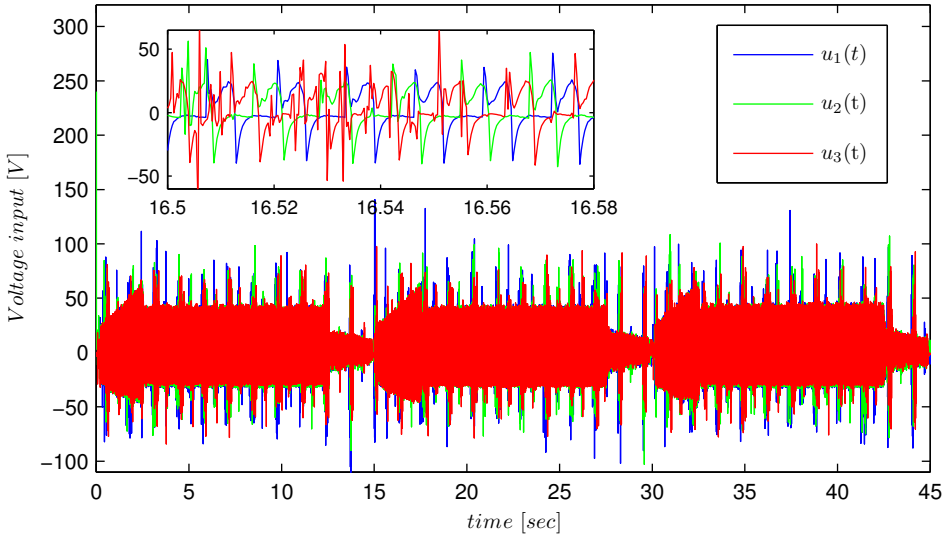

FIGURE 5.28: Control input corresponding to the saturated ramp reference for the *PID+* Feedback controller.

5.5.3 Sinusoidal velocity reference

The last scenario for this controller corresponds to the sinusoidal velocity reference constructed by the function $\omega^*(t) = 100\sin(0.45t)$.

The result of control for the velocity tracking is depicted in Figure 5.29, where it can be noticed, once again, good results. Furthermore, unlike experiments for the PI^2D controller, there are no delays; this result is better than the presented in Figures 5.8 and 5.19. Although we may notice small oscillations around the desired velocity, a very good fit between reference and real velocity is achieved.

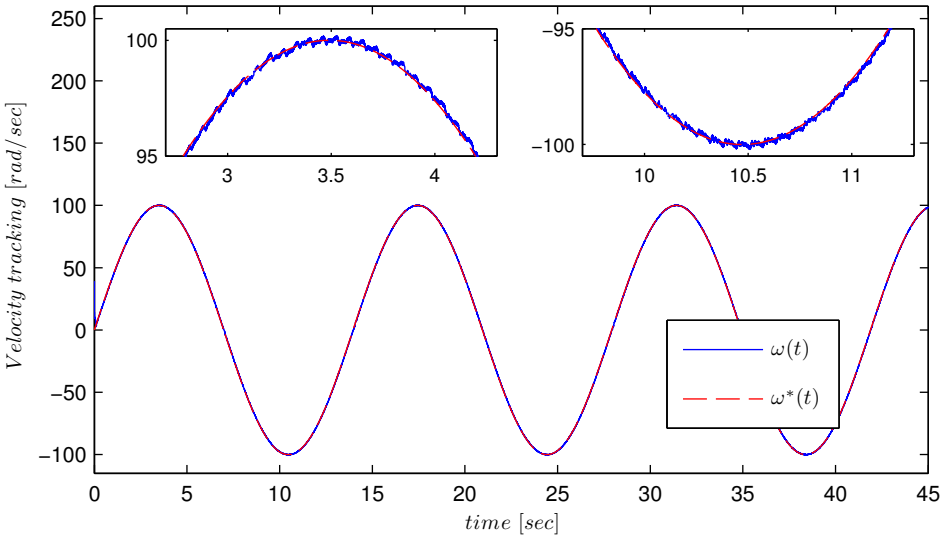

FIGURE 5.29: Velocity tracking of the sinusoidal reference for the $PID+$ Feedback controller.

The results corresponding to electrical current tracking are shown in both plots on Figure 5.30, similarly to the presented in the previous sections. The overall behavior of the currents is

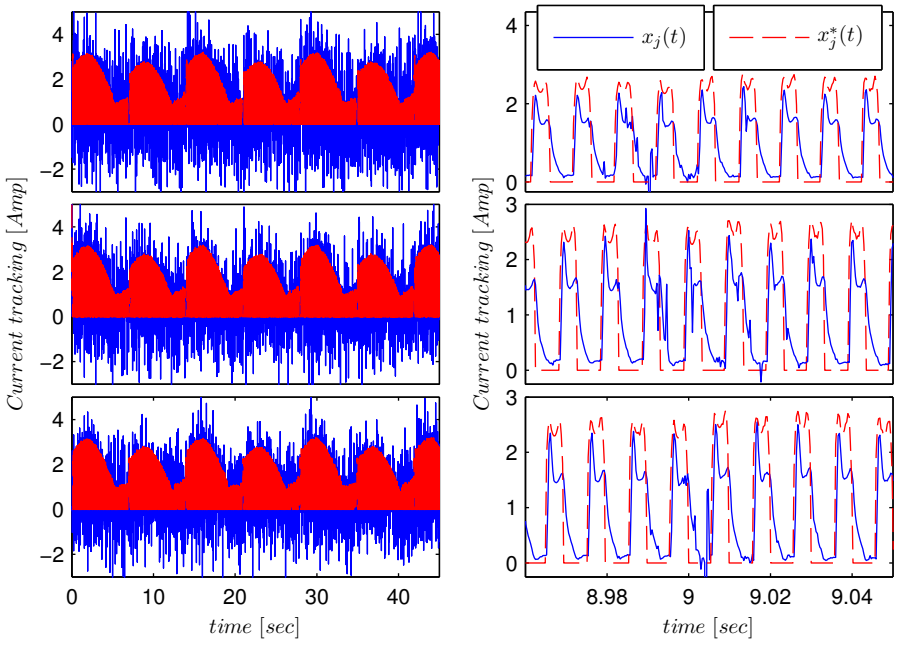

FIGURE 5.30: Current tracking corresponding to the sinusoidal reference for the $PID+$ Feedback controller.

presented in left hand side plots, it must be remarked that current merely reaches 3.5[A], with some overshoots apearing which are not significant.

On the right hand side plots detailed current tracking is depicted, notice the small errors and magnitude of the currents. It is also important to notice that the current does not reach zero, which means that stator remains magnetized despite the shooting off of the corresponding phase.

The last graph, shown in Figure 5.31, corresponds to the voltage control input. Once again, notice in the zoomed window that the voltage magnitudes are not larger than ±50[V] for almost all time and, consequently, the utilized converter is appropriate for these conditions and scenarios. We must point out that this graph pictures the ”output“

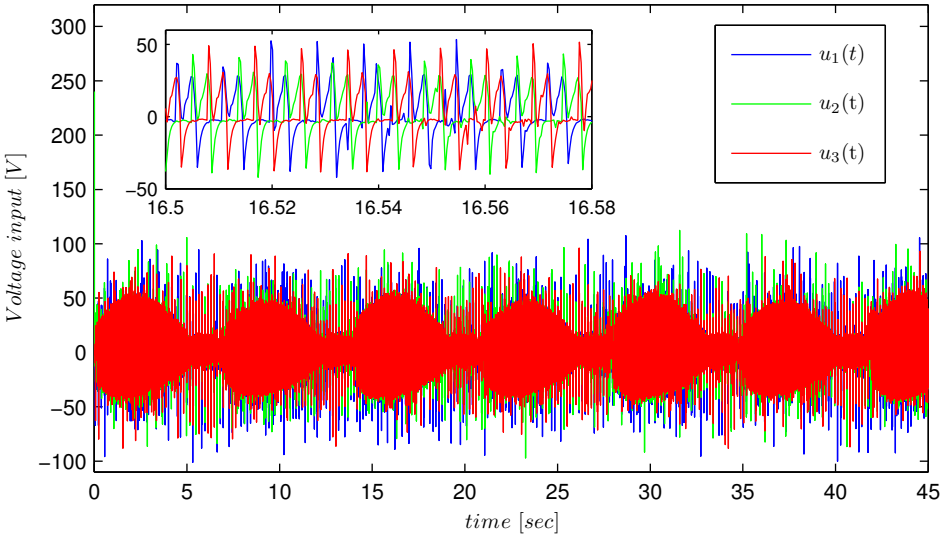

FIGURE 5.31: Voltage control input corresponding to the sinusoidal reference for the *PID+* Feedback controller.

Chapter 6

Conclusions

6.1 General conclusions

In this thesis we have **designed, and tested experimentally three different velocity controllers** for the switched-reluctance motor. In Chapters 3 and 4 we have presented the design, the theoretical results and the numerical simulations of three velocity controllers of the switched-reluctance motor. The first controller was designed for the so-called $q-model$ with the assumption of **known parameters** and **unknown both velocity and load torque**. In a second stage, in addition to velocity and load torque, **physical parameters are assumed unknown**. This work is presented in Chapter 3. For these two first controllers we have achieved uniform global exponential stability of the error variables in the parameter known case and uniform global asymptotical stability in the case of parameter uncertainty.

The third controller, presented in Chapter 4, was designed considering the so called $\rho-model$ under the assumption of **unknown load torque** but **parameters and the whole state are available**. For this controller we have achieved uniform global exponential stability of the origin of the controlled system. This result is important because it is a **first step towards the full sensorless control** were position and velocity measurements are replaced by the observed states coming from a virtual sensor. All these result are summarized in Tables 6.1 and 6.2.

Controller	**Assumptions**	**Stability results**
PI^2D+Feedback controller in Chapter 3	Parameters known Load torque unknown Velocity unknown	uniform global exponential stability
PI^2D+Adaptive feedback controller in Chapter 3	Parameters unknown Load torque unknown Velocity unknown Parameter estimation	uniform global asymptotical stability
PID+Feedback controller in Chapter 4	Parameters known Load torque unknown Velocity known	uniform global exponential stability

TABLE 6.1: Assumed conditions and theoretical results of the designed controllers.

Finally, in Chapter 5 we have presented the results of the experimental tests performed in order to investigate the behavior of the proposed controllers. During these experiments three different profiles were imposed for each one of the three designed controllers. The control objectives of the all tests was the mechanical velocity. As it can be noted in Chapter 5, we have obtained good results during the experimental tests, where the variable of interest is the mechanical velocity.

Profile / Controller	Smooth steps	Saturated ramp	Sinusoidal reference
PI^2D+Feedback controller	Good velocity tracking well behaved Good in current tracking	Velocity tracking with small delay Good in current tracking	Velocity tracking with small delay Good in current tracking
PI^2D+Adaptive feedback controller	Good velocity tracking well behaved Good in current tracking Parameter estimation with bounded error	Velocity tracking with small delay Current tracking with error in magnitude Parameter estimation with bounded error	Velocity tracking with small delay Not good in current tracking Parameter estimation with bounded error
PID+Feedback controller	Good in velocity tracking Good in current tracking	Vel. Tracking with small overshoot Current tracking with error in magnitude	Good in velocity tracking Good in current tracking with erroro in magnitude

TABLE 6.2: Tested controllers and imposed velocity-profiles.

6.2 Future work

Future work includes observer based control of the switched-reluctance motor by modifying the PID+*feedback* controller presented in Chapter 4, that is, adding a certainty equivalence control. Concerning the PI^2D presented in Chapter 3, it is interesting to run research towards improvements in the adaptive law, based on the research presented in [62] among others, this because the results obtained during experiments are subject to improvements.

Appendix A

Material in support of the PI^2D Controller

A.1 Hurwitz property of matrix $A(\eta)$ in (3.14)

Claim 1. *The matrix $A(\eta)$ in (3.14) is Hurwitz for any $0 < J \in [J_m,\, J_M]$ and $0 < \eta \in [\eta_m,\, \eta_M]$ if*

$$b \geq \left[\frac{\eta_M}{J_m} + 1\right] a + 1, \quad k_p' > k_d \tag{A.1}$$

where $\lambda \in (0, 1)$. Then, under the conditions (A.1) there exists a positive definite matrix $P(\eta, J)$ and reals q_m, $p_M \geq p_m > 0$ and $\varepsilon \in (0, 1)$ independent of η and J such that

$$2p_m \left|\xi\right|^2 \leq \xi^\top P \xi \leq p_M \left|\xi\right|^2,$$

$Q = -(A^\top P + PA) = -(Q_1 + Q_2)$ such that $Q_1 = Q_1^\top$ is positive definite and $Q_2 = Q_2^\top$ is positive semidefinite such that $q_m \left|\xi\right|^2 \leq \frac{1}{2}\xi^\top Q_1 \xi$ and $\xi^\top Q_2 \xi \geq \varepsilon(J/\eta)(b-1)e_\omega^2$.

Proof of Claim 1. Let $\varepsilon_1,\, \varepsilon_2 \in (0, 1)$ and P in (3.17) defined as

$$P = \begin{bmatrix} k_p' & (J/\eta)\varepsilon_1 & 0 & 0 \\ (J/\eta)\varepsilon_1 & (J/\eta) & -(J/\eta)\varepsilon_1 & -\varepsilon_2 \\ 0 & -(J/\eta)\varepsilon_1 & k_d/b & 0 \\ 0 & -\varepsilon_2 & 0 & \varepsilon_1/k_i \end{bmatrix}.$$

This matrix is diagonal dominant hence positive definite, if

$$\begin{aligned} k_p' &> (J_M/\eta_m)\varepsilon_1, & 1 &> 2(J_M/\eta_m)\varepsilon_1 + \varepsilon_2 \\ \frac{k_d}{b} &> (J_M/\eta_m)\varepsilon_1, & \frac{\varepsilon_1}{k_i} &> \varepsilon_2. \end{aligned}$$

These conditions hold for sufficiently small ε_1 and ε_2 such that $k_i \leq \varepsilon_1$, therefore there exist p_m and $p_M > 0$ such that

$$p_m \left|\xi\right|^2 \leq V_1(\xi) \leq p_M \left|\xi\right|^2 .$$

Next, let $Q := A^\top P + PA$ be partitioned as

$$Q = -\underbrace{\begin{bmatrix} Q_{1B} & 0 \\ 0 & (\eta/J)\varepsilon_2 \end{bmatrix}}_{Q_1} - \underbrace{\begin{bmatrix} Q_{2B} & Q_{2v} \\ Q_{2v}^\top & (\eta/J)\varepsilon_2 \end{bmatrix}}_{Q_2} \tag{A.2}$$

where

$$Q_{1B} = \begin{bmatrix} \varepsilon_1 k_p' & -\varepsilon_2 k_i & \varepsilon_1(k_d - k_p') \\ -\varepsilon_2 k_i & \varepsilon_1\Big[\frac{J}{\eta}(b-1) - \frac{2\varepsilon_2 k_i}{\varepsilon_1^2}\Big] & \Big(\varepsilon_2 k_i - \frac{J}{\eta}\varepsilon_1 a\Big) \\ \varepsilon_1(k_d - k_p') & \Big(\varepsilon_2 k_i - \frac{J}{\eta}\varepsilon_1 a\Big) & k_d\Big(\frac{a}{b} - \varepsilon_1\Big) \end{bmatrix},$$

$$Q_{2B} = \begin{bmatrix} \varepsilon_1 k_p' & 0 & 0 \\ 0 & \varepsilon_1 \frac{J}{\eta}(b-1) & 0 \\ 0 & 0 & k_d\Big(\frac{a}{b} - \varepsilon_1\Big) \end{bmatrix},$$

and

$$Q_{2v} = \frac{\eta}{J}\begin{bmatrix} -\varepsilon_2 k_p' & 0 & -k_d\varepsilon_2 \end{bmatrix}^\top$$

Since $(\eta/J)\varepsilon_2 > 0$ the matrix Q_1 in (A.2) is positive definite if and only if so is Q_{1B}; the latter holds if Q_{1B} is diagonal dominant. This in turn holds for small values of $\varepsilon_1 \geq \varepsilon_2 \geq k_i$ and control gains satisfying (A.1). Thus, there exists $q_m > 0$ such that $q_m \left|\xi\right|^2 \leq \frac{1}{2}\xi^\top Q \xi$. On the other hand, the Schur complement of Q_2 is positive for sufficiently small values of ε_1 and ε_2, independently of the center element in Q_{2B} hence, we have $\xi^\top Q_2 \xi \geq (J/\eta)\varepsilon(b-1)e_\omega^2$ with $\varepsilon := \varepsilon_1$. This is detailed along the following lines.

Matrix Q_1 in (A.2) is definite positive if the following stands. For given positive numbers k_p', k_d, k_i, a and b such that

$$b \geq \Big[\frac{\eta_M}{J_m} + 1\Big]a + 1, \quad k_p' > k_d \tag{A.3}$$

there exist $\varepsilon_1, \varepsilon_2 > 0$ s.t. $Q_1 > 0$. Let

$$\lambda = \frac{k_d}{k_p'} < 1, \tag{A.4}$$

$$\varepsilon_1 \leq \min\left\{1, \frac{k_d}{b}\Big(1 + \frac{2J_m}{\eta_M}\Big)^{-1}, \frac{a\lambda}{2b(\lambda+1)}\right\}, \tag{A.5}$$

$$\lambda_2 := \frac{a}{\varepsilon_1 b}$$

and ε_2 be such that

$$\frac{\varepsilon_2}{\varepsilon_1} \leq \frac{1}{k_i}\min\Big\{\alpha_1, \alpha_2, \alpha_3, \alpha_4\Big\} \tag{A.6}$$

where $\alpha_1 = k_d$, $\alpha_2 = \dfrac{J_m}{\eta_M}\Big[b - 1 - a\Big] - a$, $\alpha_3 = \dfrac{\varepsilon_1 a}{2}$ and $\alpha_4 = \dfrac{k_i}{k'_p}\Big[\dfrac{J_m}{\eta_M}\Big]\left[1 + \dfrac{\lambda}{\lambda_2 - 1}\right]^{-1}$.

Note that given a, b, k'_p, k_i and k_d satisfying (A.3), the conditions (A.5) and (A.6) hold for sufficiently small values of ε_1 and ε_2. Also note that $\lambda_2 > 1$ since, in view of (A.5) we have $a > b\varepsilon_1$. Now, Q_1 is diagonal dominant if

$$\varepsilon_1 \left|\lambda - 1\right| k'_p + \varepsilon_2 k_i \leq \varepsilon_1 k'_p \tag{A.7}$$

$$\varepsilon_2 k_i + \left|\varepsilon_2 k_i - (J/\eta)\varepsilon_1 a\right| \leq \varepsilon_1\Big[(J/\eta)(b-1) - \frac{2\varepsilon_2 k_i}{\varepsilon_1^2}\Big] \tag{A.8}$$

$$\varepsilon_1 k'_p \left|\lambda - 1\right| + \big[\varepsilon_2 k_i + (J/\eta)\varepsilon_1 a\big] \leq \lambda k'_p\Big(\frac{a}{b} - \varepsilon_1\Big) \tag{A.9}$$

Since $\lambda < 1$ (A.7) holds if

$$\varepsilon_1 k'_p \geq \varepsilon_2 k_i + \varepsilon_1(1-\lambda)k'_p \quad \Leftrightarrow \quad \varepsilon_1 \lambda k'_p \geq \varepsilon_2 k_i$$

which is equivalent to

$$\frac{\varepsilon_2}{\varepsilon_1} \leq \frac{\lambda k'_p}{k_i}$$

which holds in view of (A.6) and (A.4). Now, we show that (A.8) holds. Again, from (A.6) we have

$$\frac{\varepsilon_2}{\varepsilon_1} \leq \frac{a\varepsilon_1}{2k_i} \quad \Leftrightarrow \quad 2\varepsilon_2 k_i \leq \varepsilon_1^2 a$$

hence, (A.8) holds if

$$\frac{J}{\eta}\big[\varepsilon_1(b-1) - \varepsilon_1 a\big] \geq 2\varepsilon_2 k_i + \varepsilon_1 a$$

which is satisfied if

$$\frac{J}{\eta}\varepsilon_1(b-1) \geq 2\varepsilon_2 k_i + \varepsilon_1 a\big(1 + \frac{J}{\eta}\big)$$

or equivalently if

$$\frac{J}{\eta}\big[b - 1 - a\big] - a \geq \frac{2\varepsilon_2 k_i}{\varepsilon_1}$$

which in turn, holds in view of (A.6).

Finally, we show that inequality (A.9) holds. Indeed since $\lambda < 1$, (A.9) is implied by

$$\frac{\lambda k'_p a}{b} \geq \varepsilon_1 k'_p + \Big(\varepsilon_2 k_i + \frac{J}{\eta}\varepsilon_1 a\Big) + \lambda k'_p \varepsilon_1$$

which holds if

$$\frac{\lambda a}{2b} \geq \varepsilon_1(1+\lambda) \tag{A.10}$$

and

$$\frac{\lambda k_p' a}{2b} \geq \Big(\varepsilon_2 k_i + \frac{J}{\eta}\varepsilon_1 a\Big). \tag{A.11}$$

Inequality (A.10) holds in view of (A.5). Since from (A.6) $2\varepsilon_2 k_i \leq \varepsilon_1^2 a$, Inequality (A.11) holds if

$$\frac{\lambda k_p' a}{2b} \geq \varepsilon_1\Big(\frac{a\varepsilon_1}{2} + \frac{J}{\eta}a\Big) \Leftrightarrow \frac{\lambda k_p'}{2b} \geq \Big(\frac{\varepsilon_1^2}{2} + \frac{J}{\eta}\varepsilon_1\Big).$$

Since $\varepsilon_1 < 1$, the latter holds if

$$\frac{\lambda k_p'}{2b} \geq \frac{\varepsilon_1}{2}\Big(1 + \frac{2J}{\eta}\Big) \quad \Leftrightarrow \quad \frac{k_d}{b}\Big(1 + \frac{2J}{\eta}\Big)^{-1} \geq \varepsilon_1$$

which holds in view of (A.5).

On the other hand, definite positiveness of Q_2 results from the application of the Schur complement, which is non-negative if

$$\varepsilon_2 \geq \begin{bmatrix} -\varepsilon_2 k_p' \\ -k_d\varepsilon_2 \end{bmatrix}^\top \begin{bmatrix} \varepsilon_1 k_p' & 0 \\ 0 & k_d\big(\frac{a}{b} - \varepsilon_1\big) \end{bmatrix}^{-1} \begin{bmatrix} -\varepsilon_2 k_p' \\ -k_d\varepsilon_2 \end{bmatrix} \begin{bmatrix} \eta \\ J \end{bmatrix}$$

the latter is equivalent to

$$\varepsilon_2 \geq \begin{bmatrix} \eta \\ J \end{bmatrix} \begin{bmatrix} \frac{\varepsilon_2^2 k_p'}{\varepsilon_1} + \frac{\varepsilon_2^2 k_p' \lambda}{\big(\frac{a}{b} - \varepsilon_1\big)} \end{bmatrix} \tag{A.12}$$

using $\lambda_2 := \dfrac{a}{b\varepsilon_1}$ we see that (A.12) holds if

$$\varepsilon_2 \geq \begin{bmatrix} \eta \\ J \end{bmatrix} \Big[\frac{\varepsilon_2^2 k_p'}{\varepsilon_1} + \frac{\varepsilon_2^2 k_p' \lambda}{(\lambda_2 - 1)\varepsilon_1}\Big] = \frac{\varepsilon_2^2 k_p'}{\varepsilon_1} \begin{bmatrix} \eta \\ J \end{bmatrix} \Big[1 + \frac{\lambda}{\lambda_2 - 1}\Big]$$

which holds in view of (A.6). We remark that

$$\xi^\top Q_2 \xi \geq \frac{J}{2\eta}\varepsilon_1(b-1)$$

A.2 Proofs of the propositions in Chapter 3

A.2.1 Proof of Proposition 3.2

In view of the definition of x^* we have $T_e^* = \hat{J}T_d$ so the rotor closed-loop dynamics yields (3.16) with $A = A(\hat{J})$. In view of Proposition 3.1 the equilibrium defined by (3.13) is uniformly globally exponentially stable if $\tilde{T}_e = 0$. Let $q_m > 0$, $\varepsilon \in (0,1)$ and $Q = Q^\top > 0$ be such that $Q = Q_1 + Q_2$ where $Q_1 = Q_1^\top$ is positive definite and $Q_2 = Q_2^\top$ is positive semidefinite such

that $q_m |\xi|^2 \le \frac{1}{2}\xi^\top Q_1 \xi$ and $\xi^\top Q_2 \xi \ge (J/\eta)\varepsilon(b-1)e_\omega^2$. In view of the Hurwitz assumption and [63, Theorem 4.2] there exist a matrix P and positive real numbers γ_1, p_m and p_M such that $Q = -(A^\top P + PA)$, $|PB| \le \gamma_1$ and

$$p_m |\xi|^2 \le V_1(\xi) \le p_M |\xi|^2 .$$

Then, the derivative of V_1 satisfies (3.18) with Q as defined above and since T_e and T_e^* are quadratic functions uniformly bounded in q, $2\left|\tilde{T}_e\right| \le k_M \left|e_x^\top (x + x^*)\right|$ so, a.e.,

$$\dot{V}_1(\xi) \le -q_m |\xi|^2 + \frac{k_M \gamma_1}{2} |\xi| \left|e_x^\top (x + x^*)\right| - (J/\eta)\varepsilon(b-1)e_\omega^2$$

On the other hand, substituting u from (3.23) in (3.8a) we obtain the stator closed-loop Equation (3.25). Consider the function $V_2 : \mathbb{R}_+ \times \mathbb{R}^3 \to \mathbb{R}_+$ defined by

$$V_2(t, e_x) = \frac{1}{2} e_x^\top L(q(t)) e_x$$

which is positive definite and radially unbounded since $|L(q)|$ is uniformly bounded and positive definite actually, in view of (3.7),

$$\frac{\ell_m}{2} |e_x|^2 \le V_2(t, e_x) \le \ell_M |e_x|^2 .$$

The total derivative of V_2 along the trajectories of (3.25) satisfies

$$\begin{aligned} \dot{V}_2(t, e_x) \le & - e_x^\top \Big[(k_{px} - \gamma_2^2 \lambda_1 - \frac{k_M}{2}\omega^*) I \\ & - \frac{\lambda_3}{2} e_x^\top K(q(t)) e_x K(q(t)) \Big] e_x + \Big[\frac{1}{\lambda_1} + \frac{1}{2\lambda_3} \Big] e_\omega^2 \end{aligned}$$

for which we used $\frac{d}{dt} L(q(t)) = K(q(t))[e_\omega + \omega^*]$, $e_x^\top K(q) e_x e_\omega \le (1/\lambda_3) e_\omega^2 + \lambda_3 \left[e_x^\top K(q) e_x\right]^2$ and $e_x^\top g e_\omega \le \lambda_1 \gamma_2^2 |e_x|^2 + (1/\lambda_1) e_\omega^2$. Thus, the total derivative of the Lyapunov function $V_3 := V_1 + V_2$ along the closed-loop trajectories satisfies

$$\begin{aligned} \dot{V}_3 \le & - \Big[(J_m/\eta_M)\varepsilon(b-1) - \frac{1}{\lambda_1} - \frac{1}{2\lambda_3} \Big] e_\omega^2 \\ & - \Big[q_m - \frac{\lambda_2 k_M \gamma_1}{2} \Big] |\xi|^2 \\ & - \Big[k_{px} - \lambda_1 \gamma_2^2 - \frac{k_M}{2} \big(\omega^* + \lambda_3 k_M |e_x|^2 \\ & \qquad + \frac{\gamma_1}{\lambda_2} |x + x^*|^2 \big) \Big] |e_x|^2 \quad \text{a.e.} \end{aligned}$$

where we used $\left|e_x^\top (x + x^*)\right| |\xi| \le (1/\lambda_2) |x + x^*|^2 + \lambda_2 |\xi|^2$. Therefore, given q_m and b, for any J, η and ε, there exist positive numbers λ_1, λ_2, λ_3 and c such that, defining $k'_{px} > 0$ and

$$\begin{aligned} k''_{px} := & \frac{k_M}{2} \big(\omega^* + \lambda_3 k_M |e_x|^2 + \frac{\gamma_1}{\lambda_2} |x + x^*|^2 \big) \\ & + \lambda_1 \gamma_2 (|y|, |x|)^2, \end{aligned}$$

V_3 satisfies

$$\dot{V}_3(t,\xi,e_x) \leq -c\Big[\,|\xi|^2 + |e_x|^2\,\Big] \quad \text{a.e.}$$

Note that k''_{px} is a non-decreasing function of $|y|$, $|x|$ and $|x^*|$ since $|x^*|^2 = \mathcal{O}(T_d)$ where T_d is linear in y. The result follows.

A.2.2 Proof of Proposition 3.3

A direct computation using

$$u = \Psi(t,y,e_x)^\top \Theta - k_{px} e_x + \Psi(t,y,e_x)^\top \tilde{\Theta},$$

leads to the closed-loop equations

$$L(q)\dot{e}_x = -[R + k_{px}]e_x - g(t,x,y)e_\omega + \Psi(t,y,e_x)^\top \tilde{\Theta} \tag{A.13a}$$

$$\dot{\tilde{\Theta}} = -k_\theta \Psi(t,y,e_x) e_x. \tag{A.13b}$$

with $g(\cdot)$ as defined in (3.26). Next, consider the Lyapunov function $V : \mathbb{R}_+ \times \mathbb{R}^4 \times \mathbb{R}^3 \times \mathbb{R}^3 \to \mathbb{R}_+$ defined by

$$V(t,\xi,e_x,\tilde{\Theta}) := V_3(t,\xi,e_x) + \frac{1}{2k_\theta}\big\|\tilde{\Theta}\big\|^2$$

which is positive definite and radially unbounded. The Hurwitz property of A implies by Proposition 3.2 that the total derivative of V along the closed-loop trajectories generated by (A.13) satisfies

$$\dot{V}(t,\xi,e_x,\tilde{\Theta}) \leq -c\Big[\,|\xi|^2 + |e_x|^2\,\Big] \leq 0 \quad \text{a.e.} \tag{A.14}$$

Uniform global stability of the origin follows integrating $\dot{V} \leq 0$ along the closed-loop trajectories hence $\xi \in \mathcal{L}_\infty$, $e_x \in \mathcal{L}_\infty$ and, in view of (3.7), a simple inspection at the closed-loop equations show that $\dot{\xi} \in \mathcal{L}_\infty$ and $\dot{e}_x \in \mathcal{L}_\infty$. Furthermore, the first inequality in (A.14) implies that $\xi \in \mathcal{L}_2$, $e_x \in \mathcal{L}_2$. The result follows *e.g.*, from [64, Lemma A.5, p. 392].

A.2.3 Proof of Proposition 3.4

The proof of Proposition 3.4 follows by applying Matrosov's theorem –see Section A.3. The first condition of the latter requires the origin $\Big[\xi \;\; e_x \;\; \tilde{\Theta}\Big] = 0$ be uniformly globally stable, this is established in Proposition 3.3. In fact, from (A.14) we have $\dot{V} \leq Y_0(\xi, e_x)$ a.e. with $Y_0(\xi,e_x) = -c\Big[\,|\xi|^2 + |e_x|^2\,\Big] \leq 0$. It is left to find differentiable locally bounded auxiliary functions with the property that their time derivatives are negative semi-definite on very particular sets. The first auxiliary function must be negative semi-definite on $\{Y_0 = 0\}$ hence, we look for a function $W_1 : \mathbb{R}_+ \times \mathbb{R}^4 \times \mathbb{R}^3 \times \mathbb{R}^3 \to \mathbb{R}$ such that

$$[\xi,\, e_x] = [0,\, 0] \implies \dot{W}_1 \leq 0.$$

We propose

$$W_1(t,\xi,e_x,\tilde{\Theta}) = -e_x^\top L(q(t))^\top \Psi_0(t)^\top \tilde{\Theta}$$

whose total derivative along the closed-loop trajectories (3.25) , (3.16) and (3.28b) yields

$$\begin{aligned}\dot{W}_1\big(t,&\xi,e_x\tilde{\Theta}\big) = -e_x^\top \left(k_{px}+R\right)\Psi_0(t)^\top\widetilde{\Theta}\\ &- g(t,x,\xi)^\top\Psi_0(t)^\top\tilde{\Theta}e_\omega - \widetilde{\Theta}^\top\Psi(t,y,e_x)\Psi_0(t)^\top\widetilde{\Theta}\\ &- e_x^\top\dot{L}(q(t))^\top\Psi_0(t)^\top\widetilde{\Theta} - e_x^\top L(q(t))^\top\dot{\Psi}_0(t)\widetilde{\Theta}\\ &+ k_\theta e_x^\top L(q(t))^\top\Psi_0(t)^\top\Psi(t,y,e_x)e_x.\end{aligned}$$

Let $\Omega\subset\mathbb{R}^{10}$ be a compact set; we see that for all $(t,\,[\xi,e_x,\tilde{\Theta}])\in\mathbb{R}_+\times\Omega\cap\{Y_0=0\}$ we have

$$\begin{aligned}\dot{W}_1\big(t,\xi,e_x,\tilde{\Theta}\big) &= Y_1(t,\tilde{\Theta})\le 0,\\ Y_1(t,\tilde{\Theta}) &= -\tilde{\Theta}^\top\Psi_0(t)\Psi_0(t)^\top\tilde{\Theta}.\end{aligned}$$

Next, we look for a second auxiliary function W_2 such that its derivative is negative semi-definite on $\mathbb{R}_+\times\Omega\cap\{Y_0=0\}\cap\{Y_1=0\}$. Let $W_2:\mathbb{R}_+\times\mathbb{R}^3\to\mathbb{R}_+$ be defined by

$$W_2(t,\tilde{\Theta}) = -\int_t^\infty e^{t-\tau}\big\|\Phi(\tau,\tilde{\Theta})\big\|^2 d\tau$$

where $\Phi(t,\tilde{\Theta})=\Psi_0(t)^\top\tilde{\Theta}$. Note that

$$\int_t^\infty e^{t-\tau}\big\|\Phi(\tau,\tilde{\Theta})\big\|^2 d\tau \ge \int_t^{t+T} e^{t-\tau}\big\|\Phi(\tau,\tilde{\Theta})\big\|^2 d\tau$$

and after (3.29), that impose the persitence of excitation condition on $\Psi_0(t)$, we obtain

$$\int_t^{t+T} e^{t-(t+T)}\big\|\Phi(\tau,\tilde{\Theta})\big\|^2 d\tau \ge \mu e^{-T}\big\|\tilde{\Theta}\big\|^2$$

consequently

$$W_2(t,\tilde{\Theta}) \le -\mu e^{-T}\big\|\tilde{\Theta}\big\|^2. \tag{A.15}$$

On the other hand, the total time derivative of W_2 along the closed-loop trajectories satisfies, after inequality (A.15),

$$\begin{aligned}\dot{W}_2(t,\tilde{\Theta}) \le 2k_\theta &\int_t^\infty e^{t-\tau}\tilde{\Theta}^\top\Psi_0(\tau)\Psi_0(\tau)^\top d\tau\,\Psi(t,y,e_x)e_x\\ &+\big\|\Phi(t,\tilde{\Theta})\big\|^2 - \mu e^{-T}\big\|\tilde{\Theta}\big\|^2.\end{aligned}$$

Now, we have $\{Y_0=0\}\cap\{Y_1=0\} = \big\{[\xi,\ e_x,\ \Phi]=[0,\ 0,\ 0]\big\}$ hence, on this set and for all $t\in\mathbb{R}_+$,

$$\dot{W}_2(t,\tilde{\Theta}) \le -\mu e^{-T}\big\|\tilde{\Theta}\big\|^2.$$

The functions $\dot{V}$, $\dot{W}_1$ and $\dot{W}_2$ are bounded from above by continuous functions which vanish

simultaneously only at $[\xi,\ e_x,\ \Phi,\ \tilde{\Theta}] = [0,\ 0,\ 0,\ 0]$. The result follows invoking the generalized Matrosov's theorem, recalled below.

A.3 Generalized Matrosov's theorem

The following material is taken from [65]. Consider the time varying, not necessarily periodic, differential equation

$$\dot{x} = F(t, x) \tag{A.16}$$

where t denotes the time, $x = \begin{bmatrix} x_1^\top & x_2^\top \end{bmatrix}^\top$ the state with $x \in \mathbb{R}^n$. We assume that $F(t, 0) = 0$ for all $t > 0$, that F is continous in t and locally Lipschitz in x uniformly in t. Then, under the following assumptions[1] the origin of (A.16) is uniformly globally asymptotically stable.

Ass. 1 The origin of (A.16) is Uniformly Globally Stable; that is, there exist functions $V_0(x), W_0(x_1) \in K_\infty$ such that the time derivative of $V_0(x)$ along system (A.16) satisfies

$$\dot{V}_0(x) \leq -W_0(x_1)$$

Ass. 2 There exist integers $j, m > 0$ and for each $\Delta > 0$ there exist

- a number $\mu > 0$
- locally Lipschitz continuous functions $V_i : \mathbb{R}_{\geq 0} \times \mathbb{R}^n \to \mathbb{R}, i \in \{1, \cdots, j\}$;
- a function $\phi : \mathbb{R}_{\geq 0} \times \mathbb{R}^n \to \mathbb{R}^m$;
- continuous functions $W_i : \mathbb{R}^n \times \mathbb{R}^m \to \mathbb{R}, i \in \{1, \cdots, j\}$;

such that, for almost all $(t, x) \in \mathbb{R}_{\geq 0} \times \beta(\Delta)$ and all $i \in \{1, \cdots, j\}$

$$\max\left\{|V_i(t, x)|, |\phi(t, x)|\right\} \leq \mu$$

$$\dot{V}_i(t, x) \leq W_i(x, \phi(t, x)).$$

Ass. 3 For each integer $k \in \{1, \cdots, j\}$, we have that

(a) $\{W_i(z, \psi) = 0 \quad \forall i \in \{1, \cdots, k-1\}$, and all$(z, \psi) \in \beta(\Delta) \times \beta(\mu)\}$ implies that

(b) $\{W_k(z, \psi) \leq 0 \quad$ and all$(z, \psi) \in \beta(\Delta) \times \beta(\mu)\}$

Ass. 4 we have that the statement

(a) $\{W_i(z, \psi) = 0 \quad \forall i \in \{1, \cdots, j\}$, and all$(z, \psi) \in \beta(\Delta) \times \beta(\mu)\}$ implies that

(b) $\{z = 0\}$

[1] In [65] *it is not assumed* that F is locally Lipschitz in x uniformly in t

Note that any of the function $\dot{V}_k$ is required to be signed-definite on the set set where all the previous bounding functions W_i with $i \in \{1, \cdots, k-1\}$ are zero.

It can be useful to note that when the $x \mapsto F(t,x)$ is locally Lipschitz uniformly in t then the uniform global stability assumption can be relaxed to uniform (local) stability and boundedness of trajectories for each x_0.

A.4 MATLAB™code to integrate data vectors

The following code allows one to calculate the integral (3.29) for all $t \in [0, 25]$

```
clear
Nr=25; m=3 ; xm=180/(m*Nr); sigma=0.1275; TL=0.15; J=0.001; nua=TL/J;
pi=3.14159265358979323846264338327; d=80e-2; d2=0.500;
f = [6/xm^5 -15/xm^4 10/xm^3 0 0 0]; Tc=360/(2*3*Nr); Tc2=2*Tc;
Tc3=Tc*3; Tc4=Tc*4; Tc5=Tc*5; Tc6=Tc*6;
ti=5e-5; %time of integration
tmax=27; t=0:ti:tmax; t=t';

WDv=180*ones(max(size(t)),1); SWDv=zeros(max(size(t)),1);
sim IntegraWD %to obtain q^*
SM1v=0*QDv; SM2v=0*QDv; SM3v=0*QDv;
for i=1:max(size(t))
    qd=QDv(i);
SM1v(i,1)=sm1(qd); SM2v(i,1)=sm2(qd); SM3v(i,1)=sm3(qd);
end
sim Compute_Hkl_OK %run Simulink to obtain Hkl
T=1 % width of time integration
Np=T/ti;
for i=1:1:(25/ti)+1
    tT=t(i:i+Np);
    M11T=M11(i:i+Np); M12T=M12(i:i+Np); M22T=M22(i:i+Np);
    M13T=M13(i:i+Np); M23T=M23(i:i+Np); M33T=M33(i:i+Np);
    iMT=[trapz(tT,M11T) trapz(tT,M12T) trapz(tT,M13T);
         trapz(tT,M12T) trapz(tT,M22T) trapz(tT,M23T);
         trapz(tT,M13T) trapz(tT,M23T) trapz(tT,M33T)];
     E=eig(iMT);
    e1(i,1)=E(1);e2(i,1)=E(2);e3(i,1)=E(3);
end
```

Appendix B

Material in support of the *PID* Controller

B.1 Properties of matrix $\Upsilon(\cdot)$

We stress some useful properties of $\Upsilon(t)$. First of all, let $q^*(0) = 0$ therefore $q^*(t) = \omega^* t$, then define $\mathbb{R}^{2\text{x}2}$ matrix

$$\Upsilon(\tau) := \begin{bmatrix} \sin(N_r q^*(\tau))^2 & -\sin(N_r q^*(\tau))\cos(N_r q^*(\tau)) \\ -\sin(N_r q^*(\tau))\cos(N_r q^*(\tau)) & \cos(N_r q^*(\tau))^2 \end{bmatrix}$$

where each entry is periodic with period $\pi/N_r\omega^*$. We compute the integral over the indicated limits

$$\begin{aligned} \int_t^{t+\pi/N_r\omega^*} \sin(N_r q^*(\tau))^2 d\tau &= \frac{1}{N_r\omega^*} \int_{N_r\omega^* t}^{N_r\omega^*[t+\pi/N_r\omega^*]} \sin(q^*)^2 dq^* \\ &= \frac{1}{N_r\omega^*} \left[\frac{1}{2}q^* - \frac{1}{4}\sin(2q^*)\right]_{N_r\omega^* t}^{N_r\omega^*[t+\pi/N_r\omega^*]} \\ &= \frac{\pi}{2N_r\omega^*} - \frac{1}{4N_r\omega^*}\left[-\sin(2N_r\omega^*[t+\pi/N_r\omega^*])) + \sin(2N_r\omega^* t)\right] \\ &= \frac{\pi}{2N_r\omega^*} \end{aligned}$$

while a similar computation yields

$$\begin{aligned} \int_t^{t+\pi/N_r\omega^*} \cos(N_r q^*(\tau))^2 d\tau &= \frac{1}{N_r\omega^*} \left[\frac{1}{2}q^* + \frac{1}{4}\sin(2q^*)\right]_{N_r\omega^* t}^{N_r\omega^*[t+\pi/N_r\omega^*]} \\ &= \frac{\pi}{2N_r\omega^*} \end{aligned}$$

On the other hand,

$$\int_t^{t+\pi/N_r\omega^*} \sin(N_r q^*(\tau))\cos(N_r q^*(\tau))d\tau = \int_t^{t+\pi/N_r\omega^*} \sin(2N_r\omega^*\tau)d\tau = 0$$

so finally, we obtain

$$\int_t^{t+\pi/N_r\omega^*} \Upsilon(\tau)d\tau = \frac{\pi}{2N_r\omega^*} I. \tag{B.1}$$

By the same reasoning we see that the product

$$\Upsilon\mathbb{J} = \begin{bmatrix} -\sin(N_r q^*)\cos(N_r q^*) & -\sin(N_r q^*)^2 \\ \cos(N_r q^*)^2 & \sin(N_r q^*)\cos(N_r q^*) \end{bmatrix} N_r$$

satisfies the following. The matrix

$$\mathit{\Pi} := \int_t^{t+\pi/N_r\omega^*} \Upsilon(\tau)\mathbb{J}d\tau = \begin{bmatrix} 0 & -\pi/2\omega^* \\ \pi/2\omega^* & 0 \end{bmatrix} \tag{B.2}$$

hence, it is skew-symmetric and

$$|\mathit{\Pi}| := \sqrt{\lambda_M\left(\Upsilon^\top\Upsilon\right)} = \pi/2\omega^*.$$

The above expressions become useful in the following section.

B.2 Proof of Lemma 4.1

In this section we present the details concerning the proof of Lemma 4.1. The derivative of V_{c2}, as expressed in (4.16a) , along the trajectories of (4.13) yields

$$\begin{aligned} \dot{V}_{c2} &= \varepsilon_1\left[-k_d e_\omega - k_p\rho^{*\top}\mathbb{J}^\top e_\rho + v\right]\rho^{*\top}\mathbb{J}^\top e_\rho \\ &\quad +\varepsilon_1 e_\omega\dot{\rho}^{*\top}\mathbb{J}^\top e_\rho + \varepsilon_1 e_\omega\rho^{*\top}\mathbb{J}^\top\left[\mathbb{J}\rho^* e_\omega + \omega\mathbb{J}e_\rho\right] \\ &= -\varepsilon_1 k_d e_\omega\rho^{*\top}\mathbb{J}^\top e_\rho - \varepsilon_1 k_p\left[\rho^{*\top}\mathbb{J}^\top e_\rho\right]^2 + \varepsilon_1 v\rho^{*\top}\mathbb{J}^\top e_\rho \\ &\quad +\varepsilon_1 e_\omega\rho^{*\top}\mathbb{J}^\top\mathbb{J}^\top e_\rho\omega^* + N_r^2\varepsilon_1\left|\rho_\circ^*\right|^2 e_w^2 + \varepsilon_1 e_w\rho^{*\top}\mathbb{J}^\top\mathbb{J}e_\rho\omega \\ &= -\varepsilon_1 k_p\left[\rho^{*\top}\mathbb{J}^\top e_\rho\right]^2 + N_r^2\varepsilon_1\left[\rho^{*\top}e_\rho + \left|\rho_\circ^*\right|^2\right]e_\omega^2 \\ &\quad -\varepsilon_1 k_d\left[\rho^{*\top}\mathbb{J}^\top e_\rho\right]e_\omega + \varepsilon_1\left[\rho^{*\top}\mathbb{J}^\top e_\rho\right]v\,. \end{aligned} \tag{B.3}$$

Next, we expose some properties of V_{c3}. Firstly, note that

$$V_{c3} = -e_\rho^\top\left[\int_t^{t+T_c} e^{(t-\tau)}\Upsilon(\tau)d\tau\right]e_\rho N_r^2\left|\rho_\circ^*\right|^2$$

and since $\Upsilon(\tau) \geq 0$ and $e^{(t-\tau)} \geq e^{(t-[t+T_c])}$ we have

$$V_{c3} \leq -e_\rho^\top \left[\int_t^{t+T_c} \Upsilon(\tau)d\tau\right] e_\rho N_r^2 \left|\rho_\circ^*\right|^2 e^{-T_c}.$$

Then, setting $T_c = \pi/N_r\omega^*$ and using (B.1) we obtain

$$V_{c3} \leq -\left(\frac{N_r\pi}{2\omega^*}\left|\rho_\circ^*\right|^2 e^{-\pi/N_r\omega^*}\right)|e_\rho|^2 \tag{B.4}$$

in which $\rho_\circ^*$ is a design parameter. Furthermore, the total derivative of V_{c3} along the trajectories of (4.13) satisfies

$$\begin{aligned}\dot{V}_{c3} \leq & -\int_t^{t+T_c} e^{(t-\tau)} 2e_\rho^\top N_r^2 \left|\rho_\circ^*\right|^2 \Upsilon(\tau)d\tau \\ & + \left|\rho^*(t)^\top \mathbb{J}^\top e_\rho\right|^2 + V_{c3}.\end{aligned} \tag{B.5}$$

Substituting (4.13b) in the first term we obtain

$$\begin{aligned}-\int_t^{t+T_c} e^{(t-\tau)} 2e_\rho^\top N_r^2 \left|\rho_\circ^*\right|^2 \Upsilon(\tau)d\tau = & \\ -N_r^2 \left|\rho_\circ^*\right|^2 \int_t^{t+T_c} e^{(t-\tau)} e_\rho^\top \Upsilon(\tau)\mathbb{J}\rho^*(\tau)d\tau e_\omega & \\ -N_r^2 \left|\rho_\circ^*\right|^2 \omega e_\rho^\top \left(\int_t^{t+T_c} e^{(t-\tau)}\Upsilon(\tau)\mathbb{J}d\tau\right) e_\rho.\end{aligned} \tag{B.6}$$

Set $T_c = \pi/N_r\omega^*$. Then, we use (B.2) to see that the first term on the right-hand side of (B.6) is bounded by $\pi N_r^2 \left|\rho_\circ^*\right|^3 |e_\rho| \left|e_\omega\right| / 2\omega^*$ while the second term is bounded by

$$N_r^2 \left|\rho_\circ^*\right|^2 |\omega| \left|e_\rho^\top \int_t^{t+\pi/N_r\omega^*} \Upsilon(\tau)\mathbb{J}d\tau e_\rho\right| = 0;$$

see (B.2). We conclude that

$$\begin{aligned}\dot{V}_{c3} \leq & \left|\rho^*(t)^\top \mathbb{J}^\top e_\rho\right|^2 - \left(\frac{N_r\pi}{2\omega^*}\left|\rho_\circ^*\right|^2 e^{-\pi/N_r\omega^*}\right)|e_\rho|^2 \\ & + \frac{N_r\pi}{2\omega^*}\left|\rho_\circ^*\right|^3 |e_\rho| \left|e_\omega\right|.\end{aligned} \tag{B.7}$$

The last term in B.7 satisfies

$$\frac{N_r^2\pi}{2\omega^*}\left|\rho_\circ^*\right|^3 |e_\rho| \left|e_\omega\right| \leq \frac{N_r^2\pi}{4\omega^*}\left|\rho_\circ^*\right| \left(|e_\rho|^2 + \left|\rho_\circ^*\right|^4 |e_\omega|^2\right).$$

Then, recalling that $k_{di} = \lambda_i k_d$ and $k_{pi} = \lambda_i k_p$, let

$$k_{d1} \geq N_r^2 \left|\rho_\circ^*\right|^2 \left(3\varepsilon_1 + \frac{\pi}{4\omega^*}\left|\rho_\circ^*\right|^3\right) \tag{B.8}$$

$$k_{p1} = 1/\varepsilon_1 \tag{B.9}$$

and

$$\delta_1 := \frac{1}{2} \begin{bmatrix} e_\omega \\ \rho^{*\top} \mathbb{J}^\top e_\rho \end{bmatrix} \begin{bmatrix} k_{d2} & \varepsilon_1 k_d \\ \varepsilon_1 k_d & \varepsilon_1 k_{p2} \end{bmatrix} \begin{bmatrix} e_\omega \\ \rho^{*\top} \mathbb{J}^\top e_\rho \end{bmatrix}$$

which is non-negative if

$$\frac{k_p \lambda_2^2}{k_d} \geq \varepsilon_1 \,. \tag{B.10}$$

Under these conditions, putting together the expressions (4.14), (B.3) and (B.7) we obtain (4.18) in Lemma 4.1.

Bibliography

[1] Kandipati Rajani. *Modelling and control of switched reluctance motor*. BSc Thesis, Vignan's Engineering College, Vadlamudi, Guntur, 2011.

[2] Moulay Tahar Lamchich Ed. *Torque Control*. InTech, ISBN: 978-953-307-428-3, 2011.

[3] R. Krishnan. *Switched Reluctance Motor Drives*. CRC Press, 2001.

[4] D. Traoré, J. De Leon, and A. Glumineau. Adaptive interconnected observer-based backstepping control design for sensorless induction motor. *Automatica*, 48(4):682 – 687, 2012. ISSN 0005-1098. doi: http://dx.doi.org/10.1016/j.automatica.2012.01.018.

[5] Marwa Ezzat, Jesus de Leon, and Alain Glumineau. Sensorless speed control of pmsm via adaptive interconnected observer. *International Journal of Control*, 84(11):1926–1943, 2011. doi: 10.1080/00207179.2011.629684. URL http://www.tandfonline.com/doi/abs/10.1080/00207179.2011.629684.

[6] Mohamed Assaad Hamida, Alain Glumineau, and Jesus de Leon. Robust integral backstepping control for sensorless {IPM} synchronous motor controller. *Journal of the Franklin Institute*, 349(5):1734 – 1757, 2012. ISSN 0016-0032. doi: http://dx.doi.org/10.1016/j.jfranklin.2012.02.005. URL http://www.sciencedirect.com/science/article/pii/S0016003212000373. <ce:title>Special Section on Nonlinear Multiresolution algorithms and Applications</ce:title>.

[7] M. Ghanes, J. De Leon, and A. Glumineau. Cascade and high-gain observers comparison for sensorless closed-loop induction motor control. *Control Theory Applications, IET*, 2(2):133–150, 2008. ISSN 1751-8644. doi: 10.1049/iet-cta:20070058.

[8] M. Ghanes. Tracking performances of backstepping and high gain observers for sensorless induction motor control against low frequencies benchmark. In *Control Applications, 2007. CCA 2007. IEEE International Conference on*, pages 652–657, 2007. doi: 10.1109/CCA.2007.4389306.

[9] A.D. Cheok and Y. Fukuda. A new torque and flux control method for switched reluctance motor drives. *Power Electronics, IEEE Transactions on*, 17(4):543 –557, jul 2002. ISSN 0885-8993. doi: 10.1109/TPEL.2002.800968.

[10] Hongwei Gao, F.R. Salmasi, and M. Ehsani. Inductance model-based sensorless control of the switched reluctance motor drive at low speed. *Power Electronics, IEEE Transactions on*, 19(6):1568 – 1573, nov. 2004. ISSN 0885-8993. doi: 10.1109/TPEL.2004.836632.

[11] I. Husain and M.S. Islam. Observers for position and speed estimations in switched reluctance motors. In *Decision and Control, 2001. Proceedings of the 40th IEEE Conference on*, volume 3, pages 2217 –2222 vol.3, 2001. doi: 10.1109/.2001.980586.

[12] L.L.N. dos Reis, F. Sobreira, A.R.R. Coelho, O.M. Almeida, J.C.T. Campos, and S. Daher. Identification and adaptive speed control for switched reluctance motor using DSP. In *Power Electronics Conference, 2009. COBEP '09. Brazilian*, pages 836 –841, 27 2009-oct. 1 2009. doi: 10.1109/COBEP.2009.5347659.

[13] H. Hannoun, M. Hilairet, and C. Marchand. Design of an srm speed control strategy for a wide range of operating speeds. *Industrial Electronics, IEEE Transactions on*, 57(9): 2911–2921, 2010. ISSN 0278-0046. doi: 10.1109/TIE.2009.2038396.

[14] M. Hilairet, H. Hannoun, and C. Marchand. Design of an optimized srm control architecture based on a hardware/software partitioning. In *Industrial Electronics, 2009. IECON '09. 35th Annual Conference of IEEE*, pages 4053–4057, 2009. doi: 10.1109/IECON.2009.5415107.

[15] P. Jinupun and P.C.-K. Luk. Direct torque control for sensorless switched reluctance motor drives. In *Power Electronics and Variable Speed Drives, 1998. Seventh International Conference on (Conf. Publ. No. 456)*, pages 329–334, 1998. doi: 10.1049/cp:19980546.

[16] C. Elmas and H. Zelaya-De La Parra. Position sensorless operation of a switched reluctance drive based on observer. In *Power Electronics and Applications, 1993., Fifth European Conference on*, pages 82–87 vol.6, 1993.

[17] C. Elmas and H. Zelaya-De La Parra. Application of a full-order extended luenberger observer for a position sensorless operation of a switched reluctance motor drive. *Control Theory and Applications, IEE Proceedings* -, 143(5):401–408, 1996. ISSN 1350-2379. doi: 10.1049/ip-cta:19960421.

[18] W.F. Ray and I.H. Al-Bahadly. A sensorless method for determining rotor position for switched reluctance motors. In *Power Electronics and Variable-Speed Drives, 1994. Fifth International Conference on*, pages 13–17, 1994. doi: 10.1049/cp:19940932.

[19] J.A. Makwana, A. Mishra, P. Agarwal, and S.P. Srivastava. Sensorless control of switched reluctance motor drive: An analytical method. In *Advances in Engineering, Science and Management (ICAESM), 2012 International Conference on*, pages 571–576, 2012.

[20] Jun Cai, Qing-Chang Zhong, and Zhiquan Deng. Estimation of srm rotor position based on coordinate transformation. In *Industrial Electronics Society, IECON 2013 - 39th Annual Conference of the IEEE*, pages 2786–2791, 2013. doi: 10.1109/IECON.2013.6699572.

[21] A. Cheok and N. Ertugrul. A model free fuzzy logic based rotor position sensorless switched reluctance motor drives. In *Industry Applications Conference, 1996. Thirty-First IAS Annual Meeting, IAS '96., Conference Record of the 1996 IEEE*, volume 1, pages 76–83 vol.1, 1996. doi: 10.1109/IAS.1996.557000.

[22] A. Cheok and N. Ertugrul. High robustness and reliability of a fuzzy logic based angle estimation algorithm for practical switched reluctance motor drives. In *Power Electronics Specialists Conference, 1998. PESC 98 Record. 29th Annual IEEE*, volume 2, pages 1302–1308 vol.2, 1998. doi: 10.1109/PESC.1998.703174.

[23] H.S. Ooi and T.C. Green. Simulation of neural networks to sensorless control of switched reluctance motor. In *Power Electronics and Variable Speed Drives, 1998. Seventh International Conference on (Conf. Publ. No. 456)*, pages 281–286, 1998. doi: 10.1049/cp:19980538.

[24] R. Zhong, Y.B. Wang, and Y.Z. Xu. Position sensorless control of switched reluctance motors based on improved neural network. *Electric Power Applications, IET*, 6(2):111–121, 2012. ISSN 1751-8660. doi: 10.1049/iet-epa.2011.0092.

[25] J. Wolff, R. Rahner, and H. Spath. Sensorless speed control of a switched reluctance motor for industrial applications. In *Optimization of Electrical and Electronic Equipments, 1998. OPTIM '98. Proceedings of the 6th International Conference on*, volume 2, pages 457–462, 1998. doi: 10.1109/OPTIM.1998.707975.

[26] P. Brandstetter and P. Krna. Sensorless control of switched reluctance motor using sliding mode observer. In *Applied Electronics (AE), 2013 International Conference on*, pages 1–4, ISSN:1803–7232, 2013.

[27] Wenzhe Lu and A. Keyhani. Sensorless control of switched reluctance motors using sliding mode observers. In *Electric Machines and Drives Conference, 2001. IEMDC 2001. IEEE International*, pages 69–72, 2001. doi: 10.1109/IEMDC.2001.939275.

[28] Han-Woong Park, Jin-Hyun Park, Soon-Jae Kwon, Jin-Gil Park, and Cheul-U Kim. A novel high performance position sensorless control of switched reluctance motor drives. In *Industrial Electronics, 2001. Proceedings. ISIE 2001. IEEE International Symposium on*, volume 1, pages 643–648 vol.1, 2001. doi: 10.1109/ISIE.2001.931870.

[29] B. Fahimi, G. Suresh, and M. Ehsani. Review of sensorless control methods in switched reluctance motor drives. In *Industry Applications Conference, 2000. Conference Record of the 2000 IEEE*, volume 3, pages 1850–1857 vol.3, 2000. doi: 10.1109/IAS.2000.882131.

[30] A. Kawamura. Survey of position sensorless switched reluctance motor control. In *Industrial Electronics, Control and Instrumentation, 1994. IECON '94., 20th International Conference on*, volume 3, pages 1595–1598 vol.3, 1994. doi: 10.1109/IECON.1994.398052.

[31] G.H. Holling. The sensorless control of variable switched reluctance motors. In *American Control Conference, 1998. Proceedings of the 1998*, volume 2, pages 1330–1338 vol.2, 1998. doi: 10.1109/ACC.1998.703630.

[32] H. Peyrl, G. Papafotiou, and M. Morari. Model predictive torque control of a switched reluctance motor. In *Industrial Technology, 2009. ICIT 2009. IEEE International Conference on*, pages 1 –6, feb. 2009. doi: 10.1109/ICIT.2009.4939734.

[33] G. Espinosa-Perez, P. Maya-Ortiz, M. Velasco-Villa, and H. Sira-Ramirez. Passivity-based control of switched reluctance motors with nonlinear magnetic circuits. *Control Systems Technology, IEEE Transactions on*, 12(3):439 – 448, may 2004. ISSN 1063-6536. doi: 10.1109/TCST.2004.824345.

[34] D.G. Taylor. Pulse-width modulated control of electromechanical systems. *Automatic Control, IEEE Transactions on*, 37(4):524–528, 1992. ISSN 0018-9286. doi: 10.1109/9.126591.

[35] R. Milman and S.A. Bortoff. Observer-based adaptive control of a variable reluctance motor: Experimental results. *Control Systems Technology, IEEE Transactions on*, 7(5):613 –621, sep 1999. ISSN 1063-6536. doi: 10.1109/87.784425.

[36] Jun Hu D. Dawson and T. Burg. *nonlinear control of electric machinery*. Marcel Dekker Inc, 1998.

[37] Hao Chen and J.J. Gu. Implementation of the three-phase switched reluctance machine system for motors and generators. *Mechatronics, IEEE/ASME Transactions on*, 15(3):421 –432, june 2010. ISSN 1083-4435. doi: 10.1109/TMECH.2009.2027901.

[38] Hala Hannoun, Mickael Hilairet, and Claude Marchand. High performance current control of a switched reluctance machine based on a gain-scheduling pi controller. *Control Engineering Practice*, 19(11):1377 – 1386, 2011. ISSN 0967-0661. doi: 10.1016/j.conengprac.2011.07.011. URL http://www.sciencedirect.com/science/article/pii/S0967066111001626.

[39] C. Mademlis and I. Kioskeridis. Gain-scheduling regulator for high-performance position control of switched reluctance motor drives. *Industrial Electronics, IEEE Transactions on*, 57(9):2922 –2931, sept. 2010. ISSN 0278-0046. doi: 10.1109/TIE.2009.2038400.

[40] S.A. Hossain, I. Husain, H. Klode, B. Lequesne, A.M. Omekanda, and S. Gopalakrishnan. Four-quadrant and zero-speed sensorless control of a switched reluctance motor. *Industry Applications, IEEE Transactions on*, 39(5):1343 – 1349, sept.-oct. 2003. ISSN 0093-9994. doi: 10.1109/TIA.2003.816541.

[41] R. Marino, P. Tomei, and C.M. Verrelli. Nonlinear tracking control for sensorless induction motors. In *Decision and Control, 2004. CDC. 43rd IEEE Conference on*, volume 4, pages 4423 – 4428 Vol.4, dec. 2004. doi: 10.1109/CDC.2004.1429447.

[42] Sebastian Ibarra-Rojasa; Jaime Moreno and Gerardo Espinosa-Péreza. Global observability analysis of sensorless induction motors. *Automatica*, 2004.

[43] P. Tomei and C.M. Verrelli. Observer-based speed tracking control for sensorless permanent magnet synchronous motors with unknown load torque. *Automatic Control, IEEE Transactions on*, 56(6):1484 –1488, june 2011. ISSN 0018-9286. doi: 10.1109/TAC.2011.2121330.

[44] Ortega Shah, Espinosa and Hilairet. An asymptotically stable sensorless speed controller for non-salient permanent magnet synchronous motors. *Int. J. Rob. Nonl. Contr.*, 23:x–y, 2012.

[45] L.O. de Araujo Porto Henriques, L.G. Barbosa Rolim, W. Issamu Suemitsu, J.A. Dente, and P.J. Costa Branco. Development and experimental tests of a simple neurofuzzy learning sensorless approach for switched reluctance motors. *Power Electronics, IEEE Transactions on*, 26(11):3330–3344, 2011. ISSN 0885-8993. doi: 10.1109/TPEL.2011.2129597.

[46] B. Parreira, S. Rafael, A.J. Pires, and P.J. Costa Branco. Obtaining the magnetic characteristics of an 8/6 switched reluctance machine: from fem analysis to the experimental tests. *Industrial Electronics, IEEE Transactions on*, 52(6):1635–1643, Dec 2005. ISSN 0278-0046. doi: 10.1109/TIE.2005.858709.

[47] Luis Oscar, Luis Oscar de Araujo Porto Henriques, P. J. Costa Branco, Luís Guilherme, Barbosa Rolim, and Walter Issamu Suemitsu. Proposition of an offline learning current modulation for torque-ripple reduction in switched reluctance motors: Design and experimental evaluation. *IEEE Trans. Ind. Electron*, 49:665–676, 2002.

[48] T. Koblara. Implementation of speed controller for switched reluctance motor drive using fuzzy logic. In *Optimization of Electrical and Electronic Equipment, 2008. OPTIM 2008. 11th International Conference on*, pages 101–105, 2008. doi: 10.1109/OPTIM.2008.4602464.

[49] H. Chen X. Zhang and Y. Xu. Modeling, simulation, and experiment of switched reluctance ocean current generator system. In *Advances in Mechanical Engineering Journal*, 2013. doi: 10.1155/2013/261241,.

[50] A. Loria, G. Espinosa-Perez, and E. Chumacero. A novel pid-based control approach for switched-reluctance motors. In *Decision and Control (CDC), 2012 IEEE 51st Annual Conference on*, pages 7626–7631, 2012.

[51] D. Shah, R. Ortega, and A. Astolfi. Speed and load torque observer for rotating machines. In *Decision and Control, 2009 held jointly with the 2009 28th Chinese Control Conference. CDC/CCC 2009. Proceedings of the 48th IEEE Conference on*, pages 6143–6148, 2009. doi: 10.1109/CDC.2009.5400745.

[52] M. Ilic'-Spong, R. Marino, S.M. Peresada, and D. Taylor. Feedback linearizing control of switched reluctance motors. *Automatic Control, IEEE Transactions on*, 32(5):371–379, May 1987. ISSN 0018-9286. doi: 10.1109/TAC.1987.1104616.

[53] G. Espinosa-Perez, P. Maya-Ortiz, M. Velasco-Villa, and H. Sira-Ramirez. Passivity-based control of switched reluctance motors with nonlinear magnetic circuits. In *Decision and Control, 2002, Proceedings of the 41st IEEE Conference on*, volume 1, pages 468 – 473 vol.1, dec. 2002. doi: 10.1109/CDC.2002.1184540.

[54] M. Ilic-Spong, R. Marino, S. Peresada, and D. Taylor. Feedback linearizing control of switched reluctance motors. *IEEE Trans. Automat. Contr.*, AC-32:371–379, 1987.

[55] A. Loria, G. Espinosa-Perez, and E. Chumacero. Exponential stabilization of switched-reluctance motors via speed-sensorless feedback. *Control Systems Technology, IEEE Transactions on*, PP(99):1–1, 2013. ISSN 1063-6536. doi: 10.1109/TCST.2013.2271446.

[56] R. Ortega, A. Loría and R. Kelly. A semiglobally stable output feedback PI2D regulator for robot manipulators. *IEEE Trans. on Automat. Contr.*, 40(8):1432–1436, 1995.

[57] R. Ortega, A. Loría P. J. Nicklasson, and H. Sira-Ramírez. *Passivity-based Control of Euler-Lagrange Systems: Mechanical, Electrical and Electromechanical Applications*. Series Comunications and Control Engineering. Springer Verlag, London, 1998. ISBN 1-85233-016-3.

[58] K. S. Narendra and A. M. Annaswamy. *Stable adaptive systems*. Prentice-Hall, Inc., New Jersey, 1989.

[59] R. Ortega, L. Praly, A. Astolfi, Junggi Lee, and Kwanghee Nam. Estimation of rotor position and speed of permanent magnet synchronous motors with guaranteed stability. *Control Systems Technology, IEEE Transactions on*, 19(3):601 –614, may 2011. ISSN 1063-6536. doi: 10.1109/TCST.2010.2047396.

[60] M. Vidyasagar. *Nonlinear systems analysis*. Prentice Hall, New Jersey, 1993.

[61] M. Aguado. *Construction and design of a benchwork for switched reluctance motors*. PhD thesis, Autonomus National University of Mexico, Mexico City, Mexico, November 2012.

[62] T. Yucelen and W.M. Haddad. Low-frequency learning and fast adaptation in model reference adaptive control. *Automatic Control, IEEE Transactions on*, 58(4):1080–1085, 2013. ISSN 0018-9286. doi: 10.1109/TAC.2012.2218667.

[63] H. Khalil. *Nonlinear systems*. Prentice Hall, 3rd ed., New York, 2002.

[64] R. Kelly, V. Santibáñez, and A. Loría. *Control of robot manipulators in joint space*. Series Advanced textbooks in control engineering. Springer Verlag, 2005. ISBN: 1-85233-994-2.

[65] A. Loría E. Panteley, D. Popovic, and A. Teel. A nested Matrosov theorem and persistency of excitation for uniform convergence in stable non-autonomous systems. *IEEE Trans. on Automat. Contr.*, 50(2):183–198, 2005.